

**ISTANBUL TECHNICAL UNIVERSITY ★ GRADUATE SCHOOL OF SCIENCE**  
**ENGINEERING AND TECHNOLOGY**

**MOTION AND ENERGY TRANSFER THROUGH COUPLED  
MICRO/NANO-SCALE CANTILEVER BEAMS VIA MECHANICAL  
RESONANCE ABSORPTION**

**M.Sc. THESIS**

**Ünal DEĞİRMENÇİ**

**Department of Mechanical Engineering**

**Solid Mechanics Programme**

**JANUARY 2014**



**ISTANBUL TECHNICAL UNIVERSITY ★ GRADUATE SCHOOL OF SCIENCE**  
**ENGINEERING AND TECHNOLOGY**

**MOTION AND ENERGY TRANSFER THROUGH COUPLED  
MICRO/NANO-SCALE CANTILEVER BEAMS VIA MECHANICAL  
RESONANCE ABSORPTION**

**M.Sc. THESIS**

**Ünal DEĞİRMENÇİ**  
**(503111519)**

**Department of Mechanical Engineering**

**Solid Mechanics Programme**

**Thesis Advisor: Asst. Prof. Erdal BULĞAN**

**JANUARY 2014**



**İSTANBUL TEKNİK ÜNİVERSİTESİ ★ FEN BİLİMLERİ ENSTİTÜSÜ**

**MİKRO/NANO-BOYUTLU ANKASTRE KİRİŞLERDE  
MEKANİK REZONANS ABSORPSİYONU YARDIMIYLA  
HAREKET VE ENERJİ TRANSFERİ**

**YÜKSEK LİSANS TEZİ**

**Ünal DEĞİRMENCI  
(503111519)**

**Makine Mühendisliği Anabilim Dalı**

**Katı Cisimlerin Mekaniği Programı**

**Tez Danışmanı: Yrd. Doç. Dr. Erdal BULĞAN**

**OCAK 2014**



**Ünal DEĞİRMENCİ**, a **M.Sc.** student of **ITU Graduate School of Science, Engineering and Technology** student ID **503111519**, successfully defended the thesis entitled “**MOTION AND ENERGY TRANSFER THROUGH COUPLED MICRO/NANO-SCALE CANTILEVER BEAMS VIA MECHANICAL RESONANCE ABSORPTION,**” which he prepared after fulfilling the requirements specified in the associated legislations, before the jury whose signatures are below.

**Thesis Advisor :**      **Asst. Prof. Dr. Erdal BULĞAN**      .....

İstanbul Technical University

**Jury Members :**      **Prof. Dr. Ekrem TÜFEKÇİ**      .....

İstanbul Technical University

**Asst. Prof. Dr. M. Selçuk ARSLAN**      .....

Yıldız Technical University

**Date of Submission : 16 December 2013**

**Date of Defense : 21 January 2014**





*To my family and friends,*



## FOREWORD

Firstly, I would like to thank my advisor Asst. Prof. Erdal BULĞAN for his guidance, help and patience during the course of this project.

My thanks extend to all my colleagues, namely Ender GÜZEL, Jaber SALAMAT, Mustafa KAYKISIZ, and Shahab Bakhtiari GORAJOOBI, in the NANOPSYS Laboratory at School of Mechanical Engineering, Istanbul Technical University. It was a pleasure to be part of the team.

I would also like to express my gratitude to dear friends, namely Bilal BİLGİLİ, Bilal ERVURAL, Emrah DÖNMEZ, and İ. Hakkı TONYALI for their support, help and advice.

I would like to thank my father, mother, brother and sister, namely Cemil DEĞİRMENCİ, Aysel DEĞİRMENCİ, Ahmet DEĞİRMENCİ Bircan DEĞİRMENCİ, Gamze DEĞİRMENCİ, and Eda ELBİR for prayers and all their support at every stage of my personal and academic life, I love them all depth of my heart.

I appreciate kind contribution of the thesis defense committee members, Prof. Dr. Ekrem TÜFEKÇİ and Asst. Prof. M. Selçuk ARSLAN for their consideration and advises.

I also want to thank warmly my advisor Asst. Prof. Erdal BULĞAN, who introduced me with this thesis topic. I am grateful to “Future Faculty Member Support Program (Öğretim Üyesi Yetiştirme programı, ÖYP)” and “ITU Scientific Research Projects Program (İTÜ Bilimsel Araştırma Projeleri Programı, İTÜ BAP)” for the financial support to this thesis study as well.

Above all, I owe it all to Almighty ALLAH for granting me the wisdom, health and strength to undertake this research task and enabling me to its completion.

January 2014

Ünal DEĞİRMENCİ  
(Industrial and Mechanical Engineer)



## TABLE OF CONTENTS

	<u>Page</u>
<b>FOREWORD</b> .....	<b>ix</b>
<b>TABLE OF CONTENTS</b> .....	<b>xi</b>
<b>ABBREVIATIONS</b> .....	<b>xiii</b>
<b>LIST OF TABLES</b> .....	<b>xv</b>
<b>LIST OF FIGURES</b> .....	<b>xvii</b>
<b>SUMMARY</b> .....	<b>xix</b>
<b>ÖZET</b> .....	<b>xxi</b>
<b>1. INTRODUCTION</b> .....	<b>1</b>
1.1 Purpose of Thesis.....	1
1.2 Literature Review .....	1
<b>2. BEAM THEORIES</b> .....	<b>11</b>
2.1 Introduction.....	11
2.2 Static Analysis .....	11
2.2.1 Euler-Bernoulli Theory .....	11
2.2.2 Rayleigh Theory.....	15
2.2.3 Euler-Bernoulli Modified Theory or Shear Model .....	16
2.2.4 Timoshenko Theory .....	17
2.3 Dynamic Analysis.....	20
2.3.1 Vibration of a Single Degree-of-Freedom (DOF) System.....	20
2.3.1.1 Free Vibration .....	20
2.3.1.2 Free Vibration Under Harmonic Force .....	22
2.3.2 Vibration of Multidegree-of-Freedom System .....	24
2.3.3 Transverse (Bending) Vibration of Beams .....	27
2.4 Summary .....	34
<b>3. FLUID STRUCTURE INTERACTION IN MICRO/NANO-SCALE CANTILEVER BEAMS FOR MRA VIA FINITE ELEMENT ANALYSIS ....</b>	<b>35</b>
3.1 Introduction.....	35
3.2 Finite Element Method .....	35
3.3 Common Element Types used in FEM.....	36
3.3.1 Three-Dimensional (3D) Beam Element .....	36
3.3.2 Constant Stress Triangular Element.....	37
3.3.3 Linear Stress Triangular Element .....	38
3.3.4 Double Linear Rectangular Element.....	38
3.3.5 Four-node Tetrahedral Element .....	39
3.3.6 Eight-node Brick Element.....	41
3.3.7 Ten-Node Tetrahedral Element.....	42
3.3.8 Twenty-Node Brick Element .....	43
3.4 Acoustic Fluid-Structure Coupling in FEM .....	44
3.4.1 Perfectly Matched Layers, PML (Absorbing Layer) .....	51
3.5 Summary .....	53

<b>4. CONCEPT AND MODEL OF THE ENERGY TRANSFER VIA MRA BETWEEN THE BEAMS .....</b>	<b>55</b>
4.1 Introduction.....	55
4.2 Concept of Energy Transfer.....	55
4.3 Modeling of Energy Transfer Between Beams in FEM Analysis .....	56
4.3.1 Material identification and geometric model .....	56
4.3.2 Definition of analysis settings and results.....	58
4.4 Summary .....	61
<b>5. RESULTS.....</b>	<b>63</b>
5.1 Introduction.....	63
5.2 Energy Transfer between Beams with Neglected Viscous Damping Ratios....	63
5.2.1 Energy transfer between beams with square cross-section at out-of-plane alignment .....	63
5.2.2 Energy transfer between beams with square cross-section at in-plane alignment .....	72
5.2.3 Energy transfer for smaller beams with square cross-section at in-plane alignment .....	74
5.2.4 Energy transfer for beams with rectangular cross-section at in-plane alignment .....	77
5.2.5 Energy transfer in micromachinable and characterizable cantilever beams with rectangular cross-section aligned at in-plane orientations.....	80
5.3 Effect of Viscous Damping on Energy Transfer between Micromachinable Beams.....	85
5.4 Summary .....	90
<b>6. CONCLUSION.....</b>	<b>93</b>
<b>REFERENCES .....</b>	<b>99</b>
<b>APPENDICES .....</b>	<b>103</b>
<b>CURRICULUM VITAE .....</b>	<b>153</b>

## ABBREVIATIONS

<b>A</b>	: Cross-sectional Area
<b>APDL</b>	: ANSYS Parametric Design Language
<b><math>b_{sys}</math></b>	: Viscous Damping Coefficient
<b>c</b>	: Acoustic Wave Speed
<b><math>c_b</math></b>	: The Longitudinal Wave Velocity
<b><math>C_c</math></b>	: Critical Damping Constant
<b>d</b>	: Distance Between Beams
<b>DOF</b>	: Degree-of-Freedom
<b>DP</b>	: Deviation Percentage
<b>E</b>	: The Modulus of Elasticity
<b><math>E_s</math></b>	: Young's Modulus of Source Beam
<b><math>E_t</math></b>	: Young's Modulus of Target Beam
<b>ET</b>	: Energy Transfer
<b>ETR</b>	: Energy Transfer Rate
<b>F</b>	: Structural Load Vector
<b><math>F^{pr}</math></b>	: Fluid Pressure Load Vector
<b>FEA</b>	: Finite Element Analysis
<b>FEM</b>	: Finite Element Method
<b>FSI</b>	: Fluid Structure Interaction
<b>G</b>	: The shear Modulus
<b>I</b>	: The Moment of Inertia
<b><math>I_s</math></b>	: The Moment of Inertia of Source Beam
<b><math>I_t</math></b>	: The Moment of Inertia of Target Beam
<b><math>k_b</math></b>	: The Longitudinal Wave Number
<b><math>k_0</math></b>	: The Wave Number
<b><math>k_w</math></b>	: Costant Wave Number
<b>K</b>	: Fluid Bulk Modulus
<b><math>K_n</math></b>	: Knudsen Number
<b><math>K^d</math></b>	: Dielectric Conductivity Matrix
<b><math>K^z</math></b>	: Piezoelectric Coupling Matrix
<b>L</b>	: Beam Length
<b><math>L_s</math></b>	: Source Beam Length
<b><math>L_t</math></b>	: Target Beam Length
<b>m</b>	: Mass
<b>M</b>	: Structural Mass Matrix
<b>MEMS</b>	: Micro-Electro-Mechanical Systems
<b>MRA</b>	: Mechanical Resonance Absorption
<b>NEMS</b>	: Nano-Electro-Mechanical Systems
<b>PML</b>	: Perfectly Matched Layer
<b>q</b>	: Distributed Load
<b>SAW</b>	: Surface Acoustic Waves
<b>t</b>	: Thickness of Beam
<b><math>U_{max}</math></b>	: Maximum Strain Energy

$U_{s, \max}$	: Maximum Strain Energy of Source Beam
$U_{t, \max}$	: Maximum Strain Energy of Target Beam
$w$	: Width
$W_{\max}$	: Maximum Deflection of Beam
$W_{s, \max}$	: Maximum Deflection of Source Beam
$W_{t, \max}$	: Maximum Deflection of Target Beam
$\omega_n$	: Natural Frequency
$\zeta$	: Damping Ratio
$\phi$	: The Phase Angle
$\rho$	: Density
$\lambda_{\text{air}}$	: Mean Free Path of Air
$\eta_{\text{air}}$	: Viscosity of Air
$\eta_{\text{eff},s}$	: Effective Viscosity of Air



## LIST OF TABLES

	<u>Page</u>
<b>Table 2.1</b> : Boundary conditions of beams.....	30
<b>Table 2.2</b> : Values of $\beta_n L$ for boundary conditions. ....	34
<b>Table 4.1</b> : Material properties of silicon and air. ....	57
<b>Table 4.2</b> : APDL codes for air layers.....	58
<b>Table 4.3</b> : APDL codes for <i>Analysis Setting</i> and FSI. ....	60
<b>Table 5.1</b> : Numerical natural beam frequencies.....	65
<b>Table 5.2</b> : Analytical natural beam frequencies.....	66
<b>Table 5.3</b> : Frequency-dependent deformation values. ....	68
<b>Table 5.4</b> : Natural frequencies of smaller beam by simulation.....	74
<b>Table 5.5</b> : Natural frequencies of smaller beam analytically.....	75
<b>Table 5.6</b> : Natural frequencies of the beam with rectangular cross-section studied numerically.....	77
<b>Table 5.7</b> : Natural frequencies of the beam with rectangular cross-section studied analytically. ....	78
<b>Table 5.8</b> : Numerical natural frequency values of the beam.....	82
<b>Table 5.9</b> : Analytical natural frequency values of the beam.....	82
<b>Table 5.10</b> : Viscous damping ratios for various separation distances. ....	88
<b>Table A.1</b> : Deflection and <i>ETR</i> values at 1 $\mu$ m separation distance. ....	104
<b>Table A.2</b> : Deflection and <i>ETR</i> values at 2 $\mu$ m separation distance. ....	105
<b>Table A.3</b> : Deflection and <i>ETR</i> values at 3 $\mu$ m separation distance. ....	106
<b>Table A.4</b> : Deflection and <i>ETR</i> values at 4 $\mu$ m separation distance. ....	107
<b>Table A.5</b> : Deflection and <i>ETR</i> values at 5 $\mu$ m separation distance. ....	108
<b>Table A.6</b> : Deflection and <i>ETR</i> values at 6 $\mu$ m separation distance. ....	109
<b>Table A.7</b> : Deflection and <i>ETR</i> values at 8 $\mu$ m separation distance. ....	110
<b>Table A.8</b> : Deflection and <i>ETR</i> values at 10 $\mu$ m separation distance. ....	111
<b>Table B.1</b> : Deflection and <i>ETR</i> values at 0.1 $\mu$ m separation distance.....	112
<b>Table B.2</b> : Deflection and <i>ETR</i> values at 0.5 $\mu$ m separation distance.....	113
<b>Table B.3</b> : Deflection and <i>ETR</i> values at 1 $\mu$ m separation distance.....	114
<b>Table B.4</b> : Deflection and <i>ETR</i> values at 2 $\mu$ m separation distance.....	115
<b>Table B.5</b> : Deflection and <i>ETR</i> values at 4 $\mu$ m separation distance.....	116
<b>Table B.6</b> : Deflection and <i>ETR</i> values at 5 $\mu$ m separation distance.....	117
<b>Table B.7</b> : Deflection and <i>ETR</i> values at 10 $\mu$ m separation distance.....	118
<b>Table C.1</b> : Deflection and <i>ETR</i> values at 0.2 $\mu$ m separation distance. ....	119
<b>Table C.2</b> : Deflection and <i>ETR</i> values at 0.5 $\mu$ m separation distance. ....	120
<b>Table C.3</b> : Deflection and <i>ETR</i> values at 1 $\mu$ m separation distance. ....	121
<b>Table C.4</b> : Deflection and <i>ETR</i> values at 2 $\mu$ m separation distance. ....	122
<b>Table C.5</b> : Deflection and <i>ETR</i> values at 0.2 $\mu$ m separation distance. ....	123
<b>Table C.6</b> : Deflection and <i>ETR</i> values at 0.5 $\mu$ m separation distance. ....	124
<b>Table C.7</b> : Deflection and <i>ETR</i> values at 1 $\mu$ m separation distance. ....	125
<b>Table C.8</b> : Deflection and <i>ETR</i> values at 2 $\mu$ m separation distance. ....	126
<b>Table D.1</b> : Deflection and <i>ETR</i> values at 0.1 $\mu$ m separation distance. ....	127

<b>Table D.2</b> : Deflection and ETR values at 0.2 $\mu\text{m}$ separation distance.....	128
<b>Table D.3</b> : Deflection and ETR values at 0.3 $\mu\text{m}$ separation distance.....	129
<b>Table D.4</b> : Deflection and ETR values at 0.4 $\mu\text{m}$ separation distance.....	130
<b>Table D.5</b> : Deflection and ETR values at 0.5 $\mu\text{m}$ separation distance.....	131
<b>Table D.6</b> : Deflection and ETR values at 1 $\mu\text{m}$ separation distance.....	132
<b>Table D.7</b> : Deflection and ETR values at 2 $\mu\text{m}$ separation distance.....	133
<b>Table E.1</b> : Deflection and ETR values at 0.1 $\mu\text{m}$ separation distance.....	134
<b>Table E.2</b> : Deflection and ETR values at 0.5 $\mu\text{m}$ separation distance.....	135
<b>Table E.3</b> : Deflection and ETR values at 0.8 $\mu\text{m}$ separation distance.....	136
<b>Table E.4</b> : Deflection and ETR values at 1 $\mu\text{m}$ separation distance.....	137
<b>Table E.5</b> : Deflection and ETR values at 2 $\mu\text{m}$ separation distance.....	138
<b>Table E.6</b> : Deflection and ETR values at 4 $\mu\text{m}$ separation distance.....	139
<b>Table E.7</b> : Deflection and ETR values at 8 $\mu\text{m}$ separation distance.....	140
<b>Table E.8</b> : Deflection and ETR values at 10 $\mu\text{m}$ separation distance.....	141
<b>Table E.9</b> : Deflection and ETR values at 12 $\mu\text{m}$ separation distance.....	142
<b>Table E.10</b> : Deflection and ETR values at 15 $\mu\text{m}$ separation distance.....	143
<b>Table E.11</b> : Deflection and ETR values at 18 $\mu\text{m}$ separation distance.....	144
<b>Table E.12</b> : Deflection and ETR values at 20 $\mu\text{m}$ separation distance.....	145
<b>Table F.1</b> : Deflection and ETR values at 0.1 $\mu\text{m}$ separation distance.....	146
<b>Table F.2</b> : Deflection and ETR values at 0.2 $\mu\text{m}$ separation distance.....	147
<b>Table F.3</b> : Deflection and ETR values at 0.3 $\mu\text{m}$ separation distance.....	148
<b>Table F.4</b> : Deflection and ETR values at 0.4 $\mu\text{m}$ separation distance.....	149
<b>Table F.5</b> : Deflection and ETR values at 0.5 $\mu\text{m}$ separation distance.....	150
<b>Table F.6</b> : Deflection and ETR values at 1 $\mu\text{m}$ separation distance.....	151
<b>Table F.7</b> : Deflection and ETR values at 2 $\mu\text{m}$ separation distance.....	152

## LIST OF FIGURES

	<u>Page</u>
<b>Figure 1.1</b> : SEM image of the suspended nanowire device, 1.3 mm long and 43 nm in diameter. b) Measurement circuit used for magnetomotive drive and detection [35].	5
<b>Figure 1.2</b> : Optical micrograph of typical mechanically coupled resonators [36].	6
<b>Figure 1.3</b> : Electrostatically coupled nanocantilevers [37].	7
<b>Figure 1.4</b> : Schematic illustration of the human ear [38].	7
<b>Figure 1.5</b> : Basilar membrane diagram showing the locations maximum displacement in the different sinusoidal frequency responses basilar [38].	8
<b>Figure 2.1</b> : a) Beam in bending. b) Free-body diagram for an element [40].	12
<b>Figure 2.2</b> : Deformation of a typical transverse normal line in various beam theories[43].	17
<b>Figure 2.3</b> : a) An n-degree-of-freedom system.b) free-body diagrams of the masses [44].	25
<b>Figure 2.4</b> : $\beta L$ values for double-clamped boundary conditions.	31
<b>Figure 2.5</b> : Mode shapes for different boundary conditions.	32
<b>Figure 2.6</b> : Expressions of the vibrating beams with different boundary conditions.	33
<b>Figure 3.1</b> : Three-dimensional Beam Element.	37
<b>Figure 3.2</b> : Constant Stress Triangular Element.	37
<b>Figure 3.3</b> : Linear Stress Triangular Element.	38
<b>Figure 3.4</b> : Double Linear Quadrilateral Element.	39
<b>Figure 3.5</b> : Four-node Tetrahedral Element.	39
<b>Figure 3.6</b> : Eight-node Brick Element.	41
<b>Figure 3.7</b> : Ten-node Tetrahedral Element.	43
<b>Figure 3.8</b> : Twenty-node Brick Element.	43
<b>Figure 3.9</b> : FLUID29 geometry.	46
<b>Figure 3.10</b> : FLUID129 geometry.	48
<b>Figure 3.11</b> : FLUID30 geometry.	48
<b>Figure 3.12</b> : FLUID221 geometry.	49
<b>Figure 3.13</b> : FLUID220 geometry.	50
<b>Figure 3.14</b> : FLUID130 geometry.	51
<b>Figure 3.15</b> : Concept of absorbing layer in 2D models: a) infinite medium, b) semi-infinite medium, c) plate.	52
<b>Figure 3.16</b> : Microstrip structure with PML regions [49].	52
<b>Figure 3.17</b> : PML region attached to interior region [49].	53
<b>Figure 4.1</b> : Conceptual illustration.	56
<b>Figure 4.2</b> : Geometric model of the beams and air layers.	57
<b>Figure 4.3</b> : Meshed geometric model with beams and air layers.	59
<b>Figure 4.4</b> : The nodal force illustration on the geometric model.	60

<b>Figure 5.1</b> : Simulation model utilized in the FEM Analysis. ....	64
<b>Figure 5.2</b> : Beam deflection values about the fundamental mode frequency. ....	67
<b>Figure 5.3</b> : Coupled vibration responses of beams with square cross-section at out-of-plane alignment: a) At off-resonant frequencies. b) At on-resonant frequency. ....	69
<b>Figure 5.4</b> : <i>ETRs</i> depending on distance between beams with square cross-section at out of plane alignment. ....	71
<b>Figure 5.5</b> : Beam geometries with square cross-section at in-plane alignment. ....	72
<b>Figure 5.6</b> : Coupled vibration responses of beams placed at in-plane alignment: a) At off-resonant frequencies. b) At on-resonant frequency. ....	72
<b>Figure 5.7</b> : <i>ETRs</i> versus distance results between beams with square cross-section at in-plane alignment. ....	73
<b>Figure 5.8</b> : Smaller beam geometries with square cross-section at in-plane alignment. ....	74
<b>Figure 5.9</b> : <i>ETRs</i> in the out-of-plane direction as a function of distance between smaller beams with square cross-section at in-plane alignment. ....	75
<b>Figure 5.10</b> : <i>ETR</i> in the transverse direction with distance between smaller beams with square cross-section at in-plane alignment. ....	76
<b>Figure 5.11</b> : Beam geometries with rectangular cross-section. ....	77
<b>Figure 5.12</b> : Coupled vibration responses of beams with rectangular cross-section placed at in-plane alignment: a) At off-resonant frequencies. b) At on-resonant frequency. ....	79
<b>Figure 5.13</b> : <i>ETR</i> versus distance between beams with rectangular cross-section at in-plane alignment. ....	79
<b>Figure 5.14</b> : Finalized beam geometries at in-plane orientation. ....	81
<b>Figure 5.15</b> : Coupled vibration responses of micromachinable beams: a) Off-resonant frequencies. b) On-resonance frequency. ....	83
<b>Figure 5.16</b> : <i>ETRs</i> as a function of distance for micromachinable beams. ....	83
<b>Figure 5.17</b> : <i>ETRs</i> as a function of greater distances for micromachinable beams at narrower frequency ranges. ....	84
<b>Figure 5.18</b> : Spectral <i>ETR</i> response for micromachinable and characterizable beams at various viscous damping caused by various separation distances. ....	89

# **MOTION AND ENERGY TRANSFER THROUGH COUPLED MICRO/NANO-SCALE CANTILEVER BEAMS VIA MECHANICAL RESONANCE ABSORPTION**

## **SUMMARY**

The famous physicist Richard Feynman suggested the idea that very small-scale apparatus and systems produced by evaporating and collecting materials are possible first in 1959 [1]. In this sense, Micro-Electro-Mechanical Systems (MEMS) have subsequently emerged and developed confirming the vision provided by Feynman as a science investigating small-scale electro-mechanical setup and systems. Research on micro/nano-scale structures is indeed spreading day-by-day. Since the volume force in micro/nano-scale systems is at significantly low levels compared to that in larger systems, micro/nano-systems can move mechanically faster and with high acceleration, are compact, and provide energy savings [2]. Hence, MEMS have applications in many fields such as ink printers, airbags, bolometers, pressure gauges, distance meters, micro/nano-filters and resonators.

One of the major issues studied by a large number of research groups is conceptual and practical mechanical vibration and resonance. A large number of researchers have targeted miniaturized structures at micro/nano-scales, which has given rise to production of many new mechanical and electronic devices [3-16]. In this thesis, a novel technique for non-contact motion and energy transfer between micro/nano-scale doubly-clamped cantilever beams at high efficiency via Mechanical Resonance Absorption (*MRA*) is presented. In order to characterize quality of the transfer, resonating beam dimensions and distances, in-plane and out-of-plane transmission directions, and effect of damping by the environment are comprehensively investigated.

In this study, energy interaction via *MRA* between two identical micro/nano cantilever beams positioned at certain distances relative to each other are examined. In addition, creating fields of application in micro/nano-scale structures, such as remote drive and selective resonance are targeted by achieving the regular relationship between energy transfer values and distance changes. Then, energy transfer is analyzed for various distances and geometries. Use of micro/nano-scale beams not only increases the efficiency of energy transfer, but also it eases fabrication, testing and characterization, particularly at oscillations with high-frequency vibrations.

In the first chapter of the thesis, brief information on the aim, scope and solution steps of the study is given and previous studies associated with the thesis topic such as Micro-Electro-Mechanical Systems (MEMS), micro/nano-scale vibration, Surface Acoustic Wave (SAW), motion and energy transfer and Mechanical Resonance Absorption (MRA) are referred under the scope of literature study.

The second chapter, first, information about the general forms of Euler Bernoulli, Rayleigh and Timoshenko Beam Theories have been introduced. Then, vibration

equations have been described for single and multi-degrees of freedom systems, and derivation of analytical formulations required for the calculation of natural frequencies and bending vibrations in beams have been shown.  $\beta nL$  values used in the calculation of natural frequencies are listed for different boundary conditions.

In the third chapter, Finite Element Method (FEM) has been mentioned briefly, and after a brief introduction about the element type used in the FEA are given, Acoustic Fluid-Structure Coupling in FEM is explained and the expression of acoustic waves is presented. Then, mechanical energy transfer between the beams via MRA is simulated. Acoustic element types are defined for the air to show acoustic properties in a commercial FEM analysis software, namely ANSYS (ANSYS Inc., USA) and necessary environment characteristics for the element types are summarized. Finally, the absorbing layer (Perfectly Matched Layers, PML) behaving as an infinite medium of modeled air environment in order to prevent back-reflection by absorbing the acoustic waves created by the target beam are described.

In the fourth chapter, initially, such concepts as representation of the cross-section of the beam geometries used in the investigation of motion and energy transfer between the beams, relative positioning, the direction of the applied force, and representation of the source and target beam are studied. Then, the interaction model, material properties, acoustic element types in air, and the program codes required to define the fluid-structure interaction between air and the beams in FEA software are described.

In the fifth chapter, energy transfer rates are studied numerically in various beam distances for two different cases where first, viscous damping ratio is neglected and, then considered. At first, ETR values are studied in a band about resonance frequency for two cross-section geometries as in square and rectangular shapes, at two settlement status as in-plane and out-of-plane, and with several geometrical dimensions. In the second half, ETR values depending on the distance between the beams with rectangular cross-section at in-plane alignment are examined under the influence of viscous damping, and the results are presented based on the data obtained in the first half of the chapter.

In the sixth chapter, obtained data are evaluated. Then, the effects of distance and the beam geometry on the performance are investigated, and the most suitable cross-sectional geometry and distance between the beams for optimum energy transfer are determined.

# MİKRO/NANO-BOYUTLU ANKASTRE KİRİŞLERDE MEKANİK REZONANS ABSORPSİYONU YARDIMIYLA HAREKET VE ENERJİ TRANSFERİ

## ÖZET

Çok küçük ölçekli düzenek ve sistemlerin malzemeleri buharlaştırarak biriktirme yolu ile üretilebileceği fikrini ilk olarak 1959 yılında ünlü fizikçi Richard Feynman ileri sürmüştür [1]. Bu anlamda, Mikro-Elektro-Mekanik Sistemler (MEMS) küçük ölçekli elektro-mekanik düzeneklerin ve sistemlerin incelendiği bir bilim dalı olarak sonradan Feynman'ın öngördüğü vizyonu doğrular biçimde ortaya çıkmış ve gelişmiştir. Mikro ve nano sistemlerin bu kadar çok ilgi toplamalarının nedenleri arasında makro boyuttaki mekanik sistemlerin mikro ve nano boyutta küçültülerek üretilmesinde hacimsel kuvvetlerin (ağırlık/atalet) önemini yitirmelerinden ötürü mekanik bakımdan çok hızlı sistemlerin gerçekleştirilebilmesi, yüksek ivmeli hareketlerin mümkün olması, daha az yer kaplamaları, enerji tasarrufu sağlamaları, seri üretimlerinin mümkün olması gibi pek çok faydayı gösterebiliriz [2]. Belirtilen bu nedenlerden dolayı, nano ve mikro mekanik sistemlerin günümüzde mürekkepli yazıcılar, hava yastıkları, ışınımölçerler, basınçölçerler, mesafeölçerler, nano ve mikro filtreler, ve rezonatörler gibi pek çok alanda uygulamaları bulunmaktadır.

Çok sayıda araştırma grubunun üzerinde çalıştığı önemli konulardan birisi de kavramsal ve uygulamalı mekanik titreşim ve rezonanstır, ve bu çabalar pek çok yeni mekanik ve elektronik cihaz üretimine yolaçmıştır. Bu alandaki çalışmalar, mikro ve nano ölçekteki Mikro-Elektro-Mekanik Sistemler/Nano-Elektro-Mekanik Sistemler (MEMS/NEMS)'in mümkün olması ile makro boyuttaki titreşimlerden, bu minyatür boyutlu yapıların titreşimlerinin incelenmesine doğru kaymaya başlamıştır [3-16]. Makro-boyutlu yapıların mikro/nano-boyutlara küçültülerek üretilmesi, Literatür Özeti'nde de bahsedildiği üzere daha küçük ebatlarda ve birbirine daha yakın mesafelerde yapılar kullanılacağından, hareket ve enerji transferi esnasında gerçekleşecek kayıpların çok daha küçük olmasına ve dolayısıyla da *MRA*'nın minyatür ebatlarda kullanımının çok daha etkin ve işlevsel bir biçimde gerçekleştirilebilmesine olanak sağlayacaktır. Bu çalışma ile mikro/nano-boyutlu ankastre kirişlerde *MRA* kullanılarak çok düşük frekanslardan çok yüksek frekanslara kadar geniş bir bant aralığında rezonans edilebilen mikro/nano-kirişler üzerinden temassız ve yüksek hızlı hareket ve mekanik enerji transferinin gerçekleştirilmesi çalışılmıştır.

Bu tezde, mikro/nano-boyutlu iki ucu sabitlenmiş (ankastre, cantilever) kirişler üzerinde Mekanik Rezonans Absorpsiyon (Mechanical Resonance Absorption, *MRA*)'u kullanarak titreşim hareketi ve enerjisinin yüksek verimlerde temassız (non-contact) olarak transferi üzerinde durulmuştur. Aslında, *MRA*-temelli hareket ve enerji transferi makro-boyutlu yapılarda da hâlihazırda gerçekleştirilmekte olup, büyük ebat ve mesafeler kullanılmasından dolayı düşük etkinlikte performans gözlenmektedir, bu nedenle mühendislik uygulamalarında kullanımı çoğunlukla tercih edilmemektedir.

Diğer yandan, *MRA*, mikro/nano-boyutlu yapılarda kullanılması halinde, hacimsel kuvvetlerin gözardı edilebilecek seviyelere düşmesinden dolayı yüksek hız ve yüksek tahrik ivmelerine dayanım, daha az yer kaplama, daha az enerji tüketimi, seri üretim halinde çok ucuz ve çok daha yüksek performanslarda hareket ve enerji transferi sağlayan cihazların gerçekleştirilmesine yolaçacaktır.

Bu çalışmada, spesifik olarak nano-boyutlu ankastre bir kirişin rezonans frekansında zorlanmış salınımı (titreştirilmesi) ile ortaya çıkan hareket ve mekanik enerjinin yakınındaki eşdeğer bir başka ankastre kiriş tarafından Mekanik Rezonans Absorpsiyonu (Mechanical Resonance Absorption, *MRA*) ve bu sayede transferini sağlamak, mekanik absorpsiyon ile hareket ve enerjinin düzlem-içi (in-plane) ve düzlem-dışı (out-of-plane) doğrultularda iletim performansını gözleme ve ölçme suretiyle karakterize etmek, bu transferin maksimum seviyede gerçekleştirilebilmesi için gerekli optimum mesafe ve boyutları belirlemek, ve sözkonusu hareket ve enerji transferinin kontrolünü gerçekleştirebilmek için muhtemel müdahale biçimlerini belirlemek hedeflenmiştir.

Tez kapsamında ankastre kirişlerin birbirlerine göre mesafeleri, ve boyutları dolayısıyla rezonans frekansları da değiştirilerek mesafe ve kiriş geometrilerinin performans üzerindeki etkileri çalışılmış ve optimum enerji transferi için en uygun kesit geometrileri ve kirişler arası mesafeler belirlenmiştir. Büyük oranda düzlem-içi hareket aktarımı çalışılması ile birlikte, düzlem-dışı aktarıma dair en temel anlamda enerji transferi de incelenmiştir. İlk olarak FEA tabanlı analiz programlarında simülasyon yoluyla kirişlerin doğal frekansları ve çalışma parametreleri belirlenmiştir. Farklı kiriş geometrisi ve konumlama mesafeleri için FEA analizleri tekrarlanarak bu parametrelerin hareket ve enerji transferi üzerindeki etkileri nümerik olarak tespit edilmiştir. Bu çalışma ile üzerinde herhangi bir tahrik elemanı yeralmadan tahrik edilmek istenen sistemler, fiziksel temas olmadan (non-contact), hava molekülleri üzerinden hareket ve enerji transferi sağlanarak tahrik edilebilecektir. Böylelikle sistemler üzerinde temaslı tahrikle ilgili problemler ortadan kaldırılmış, üretimlerinde ve karakterizasyon testlerinde büyük kolaylıklar sağlayacağı düşünülmektedir.

Tezin birinci bölümünde, çalışmanın amacı, kapsamı ve çözüm aşamaları hakkında kısaca bilgiler verilerek, Literatür Çalışması başlığı altında tez konusu ile ilişkili olan Mikro-Elektro-Mekanik Sistemler (MEMS), mikro ve nano boyutta titreşim, yüzey akustik dalgalar (Surface Acoustic Wave, SAW), hareket ve enerji transferi ve Mekanik Rezonans Absorpsiyonu (Mechanical Resonance Absorption, *MRA*) konularına dair yapılan çalışmalara değinilmiştir.

İkinci bölümde, ilk olarak Euler Bernoulli, Rayleigh ve Timoshenko Kiriş Teorileri'nin genel formları hakkında bilgi verilmiştir. Ardından tek ve çok serbestlik dereceli sistemler için titreşim eşitlikleri anlatılarak kirişlerde eğilme titreşiminin ve doğal frekans değerlerinin analitik hesaplanması için gerekli formülasyonların elde edilişi gösterilmiş ve farklı sınır şartları için, doğal frekans değerlerinin hesaplanmasında kullanılan  $\beta_n L$  değerleri sıralanmıştır.

Üçüncü bölümde, sonlu elemanlar yönteminden kısaca bahsedilerek sonlu elemanlar analizinde kullanılan eleman tipleri hakkında kısaca bilgi verilmesinden sonra akışkan-katı etkileşimi açıklanarak akustik dalga ifadesi sunulmuştur. Ardından *MRA* yardımı ile ankastre kirişler arasındaki hareket ve enerji transferinin sonlu elemanlarda simüle edilmesi için yaygın bir sonlu elemanlar yazılımı olan ANSYS Inc., ABD programında havanın akustik özellik göstermesi için tanımlanan akustik eleman tipleri ve bu eleman tiplerine gerekli ortam özellikleri tanımlanması için kullanılan anahtar



program kodları kısaca açıklanmıştır. Bu bölümde son olarak, oluşturulan hava ortamının, sonsuz bir ortam gibi davranması ve hedef kirişin oluşturduğu akustik dalgaları sönümleyerek geri-yansımasının engellenmesi için kullanılan absorpsiyon katmanı (Perfectly Matched Layers, PML)'nin sönümleme işlemi ve akustik elemanlarda özellik olarak tanımlanması anlatılmıştır.

Dördüncü bölümde, ilk olarak kirişler arasındaki hareket ve enerji transferinin incelenmesinde kullanılacak kirişlerin kesit geometrilerinin gösterimi, birbirlerine göre konumlandırılmaları, uygulanan kuvvet ve kuvvetin uygulanma doğrultusu ile tahrik edilen ve enerjinin aktarıldığı kirişlerin gösterimi gibi çalışmanın ilgili kavramı açıklanmıştır. Ardından FEA yazılımında bu etkileşimin modellenmesi malzeme değerlerinin girilmesi, hava elemanına akustik eleman tipinin tanımlanması, kirişler ve hava arasındaki akışkan-katı etkileşiminin sağlanması için kullanılması gereken program kodları açıklanmıştır.

Beşinci bölümde, enerji transfer oranları, viskoz sönüm oranlarının ihmal edildiği ve dahil edildiği durumlar olmak üzere farklı kiriş mesafeleri için sayısal olarak çalışılmış ve elde edilen sonuçlar iki kısımda sunulmuştur. İlk kısımda, enerji transfer oranları kare ve dikdörtgen şekilli olmak üzere iki farklı kesit geometrisi üzerinde, düzlem-içi ve düzlem-dışı olmak üzere iki farklı yerleşim durumunda ve farklı geometrik boyutlar için farklı mesafe değerlerinde rezonans frekansı bölgesi etrafındaki bir bantta çalışılmıştır. İkinci kısımda ise ilk kısımda elde edilen bilgiler doğrultusunda sadece düzlem-içi yerleştirilmiş dikdörtgen kesitli kirişler arasındaki mesafeye bağlı enerji transfer oranları viskoz sönüm etkisi altında incelenmiş ve elde edilen sonuçlar sunulmuştur.

Tezin altıncı bölümünde ise yapılan çalışmalar sonucunda elde edilen veriler değerlendirilerek mesafe ve kiriş geometrilerinin performans üzerindeki etkileri ve optimum enerji transferi için en uygun kesit geometrileri ve kirişler arası mesafeler belirlenmiştir.



## **1. INTRODUCTION**

### **1.1 Purpose of Thesis**

In this thesis, a novel technique for non-contact motion and energy transfer between micro/nano-scale both end-fixed cantilever beams at high efficiency via Mechanical Resonance Absorption (*MRA*) is presented. *MRA*-based motion and energy transfer has already been carried out on macro-scale structures, however, low transfer performance due to large size and distance uses is observed. Despite low performance levels at macro-scale, cost-effective devices transferring motion and energy at high-efficiency when *MRA* on micro/nano-scale structures is used are achievable. Those at micro/nano-scale dimensions have such advantageous properties as high-speed and high actuation acceleration strength, less space, less energy consumption, and mass production due to negligible levels of volumetric forces. Towards the aforementioned goal, forced oscillations at resonance between two doubly-clamped micro/nano-scale identical beams located in the vicinity using Mechanical Resonance Absorption (*MRA*) is utilized for enabling remote mechanical energy transfer in air. In order to characterize quality of the transfer, resonating beam dimensions and distances, in-plane and out-of-plane transmission directions, and effect of damping by the environment are comprehensively investigated.

### **1.2 Literature Review**

The famous physicist Richard Feynman suggested the idea that very small-scale apparatus and systems produced by evaporating and collecting materials are possible first in 1959 [1]. In this sense, Micro-Electro-Mechanical Systems (*MEMS*) have subsequently emerged and developed confirming the vision provided by Feynman as a science investigating small-scale electro-mechanical setup and systems. Research on micro/nano-scale structures is indeed spreading day-by-day. Since the volume force in micro/nano-scale systems is at significantly low levels compared to that in larger systems, micro/nano-systems can move mechanically faster and with high

acceleration, are compact, and provide energy savings [2]. Hence, MEMS has applications in many fields such as ink printers, airbags, bolometers, pressure gauges, distance meters, micro/nano-filters and resonators.

One of the major issues studied by a large number of research groups is conceptual and practical mechanical vibration and resonance. A large number of researchers have targeted miniaturized structures at micro/nano-scales, which has given rise to production of many new mechanical and electronic devices [3-16]. Among such studies are those focusing on micro/nano-scale resonators, filters and sensors working based on the principle of spectral response change [4-9].

Since they can resonate at very high frequency resulting mass sensitivities, micro/nano-scale cantilever beams are frequently used in the design of miniature resonators. In addition, the fact that classical theory for macro-scale is insufficient to identify the mechanical performance of beams is understood [10]. Therefore, researchers have sought such other issues as the effect of the geometric boundary conditions and material [5], and non-linear effect on frequency in their studies [11]. A number of research groups also investigated the effects on the frequencies of nano-scale systems of change in the geometry of the structure and heat changes [12,13]. Another research group have explained vibration and stability analysis of fluid passing through the tubular micro/nano-beams by the theory of non-elasticity [14].

Furthermore, they have observed the behavior of vibration and the fundamental frequency of single-layer grapheme structures with the theory of non-elasticity, and they have demonstrated that it is possible the use of grapheme-based structures as a resonator [15]. In addition to these studies, some studies are continued such as, characterization of an electrostatically coupled oscillator MEM filter [7], measurement and vibration analysis in plane and out-of-plane of MEMS resonators [6], dynamics of mechanically and electrostatically coupled microcantilevers [16].

Another important issue is Surface Acoustic Waves (SAW) when we consider in the vibrations and waves topics. For over thirty years, the effects of surface acoustic wave devices is used for electrical signal processing as the basic principle [17]. The surface acoustic wave devices are not only used in the signal processing but also many areas such as telecommunications industry due to their properties as high performance, small size and high reproducibility, and also are used as pressure sensor, temperature sensor,

sensor applications such as biosensors and mass sensors due to the high accuracy with time and crystal-stability [17, 18, 19].

Working principle of Surface Acoustic Wave devices is very simple as scope. An acoustic wave confined on the surfaces of the bottom layer materials, is generated and spread. If any object is located on the same surface, this object will cause change on the wave properties. SAW devices work by ground on this change on wave properties [20]. Surface acoustic waves are affected sensitively from change in physical and chemical properties of the active layer on the crystal surface [21]. Surface molecules also affects the propagation of surface acoustic waves. Their circuit elements are formed to measure these effects depending on change in the resonance frequency, amplitudes, or change in phase angles of the surface acoustic wave [20].

When we investigate studies done on surface acoustic wave issue, Wixforth and Kothaus have examined between two dimensional electron system and surface acoustic wave on the heterogeneous mixture at high magnetic field and low temperature. They have demonstrated that strong quantum oscillations formed when the sound velocity and sound described quantitatively the interaction between two-dimensional electron system and the surface acoustic waves was examined [22]. Walsh et al. have developed immunity sensor using a surface acoustic wave device with two orbits [23].

Jakubik *et al.* have presented a double-layer structure in a surface acoustic wave sensor system for the detection of hydrogen. They have also reported that sensibility is influenced from changes in temperature and decrease with the increase of the temperature [24]. A group of researcher has tried identifying wave phase velocities and electromechanical coupling constant by developing a model to describe the wave propagation of surface acoustic, and they have demonstrated that wave velocities can reach up to 9500 m/s [19]. Springer *et al.* have expressed surface acoustic wave sensors can be used as completely passive and wireless questionable in many enemies (harmful) environment [18].

Another widely studied field is macro-dimensional structures of energy conversion and energy transfer between the structures. In this regard, energy transfer may be carried out to several methods. One of these methods is the mechanical energy coupling based on the mechanical resonance absorption. Hollweg has presented a

mechanical model for resonance absorption, and shown sound waves collected in the same direction when the system is running [25].

Powell *et al.* have investigated the dielectric and mechanical absorption mechanisms for time and frequency domain transformation models [26]. Kerschen *et al.* have studied energy transfer between the two-coupled oscillators for two nonlinear connection status, such as the temporary orbital bridge and reproduction of resonance, and expressed that the energy is always transferred irreversibly from linear oscillator to the nonlinear-coupled oscillator [27].

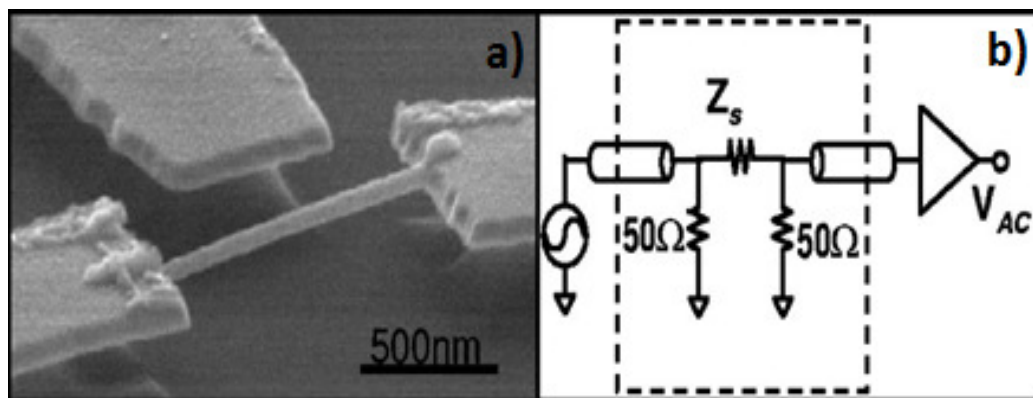
In another study, Carcaterra and Akay have observed that an important part of the energy in start oscillator may be transferred to other groups without having to turn back to the starting oscillator, and energy will remain there [28]. Likewise, they have studied smaller sized resonator placed on the main body in a specific frequency band in macro-dimensional structures in order to ensure energy equipartition but it is still macro-scale [29, 30 and 31]. In this study, motion and energy transfer are limited with the magnitude of natural frequency and the distribution patterns of resonators mounted on the main body. Motion and energy are transferred by tally with natural frequencies of used a certain number of resonators and discrete from the main body. The results of these studies are used in order to absorb vibration in different transportation vehicles [30, 31].

Understanding and controlling nonlinear coupling between vibrational modes is critical for the development of advanced nanomechanical devices; it has important implications for applications ranging from quantitative sensing to fundamental research. However, achieving accurate experimental characterization of nonlinearities in nanomechanical systems (NEMS) is problematic. Matheny *et al.* have described an experimental protocol and a highly linear transduction scheme, specifically designed for NEMS, that enables accurate, in situ characterization of device nonlinearities. By comparing predictions from Euler–Bernoulli theory for the intra- and intermodal nonlinearities of a doubly clamped beam, we assess the validity of our approach and find excellent agreement [32].

Villanueva *et al.* have presented the first highly controlled measurements of the nonlinear response of nanomechanical cantilevers using an ultralinear detection system. This is performed for an extensive range of devices to probe the validity of Euler-Bernoulli theory in the nonlinear regime. They found that its predictions deviate strongly from their measurements for the nonlinearity of the fundamental flexural mode, which show a systematic dependence on aspect ratio (length/width) together with random scatter. This contrasts with the second mode, which is always found to be in good agreement with theory. These findings underscore the delicate balance between inertial and geometric nonlinear effects in the fundamental mode, and strongly motivate further work to develop theories beyond the Euler-Bernoulli approximation [33].

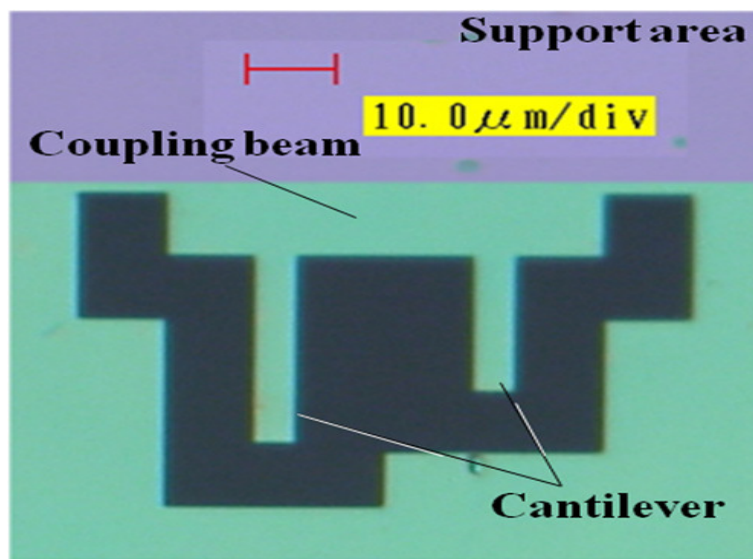
Karabalin *et al.* have reported the first controlled measurements of stress-induced change in cantilever stiffness with commensurate theoretical quantification. Simultaneous measurements are also performed on equivalent clamped-clamped beams. All experimental results are quantitatively and accurately predicted using elasticity theory. They have also presented conclusive experimental evidence for invalidity of the longstanding and unphysical axial force model, which has been widely applied to interpret measurements using cantilever beams [34].

Husain *et al.* have presented the fabrication and measurement of a platinum nanowire resonator, 43 nm in diameter and 1.3 $\mu$ m in length as seen in Fig. 1.1. This device, among the smallest NEMS reported, has a fundamental vibration frequency of 105.3 MHz, with a quality factor of 8500 at 4 K. Its resonant motion is converted by a technique that is well suited to ultra-small mechanical structures [35].



**Figure 1.1** : SEM image of the suspended nanowire device, 1.3 mm long and 43 nm in diameter. b) Measurement circuit used for magnetomotive drive and detection [35].

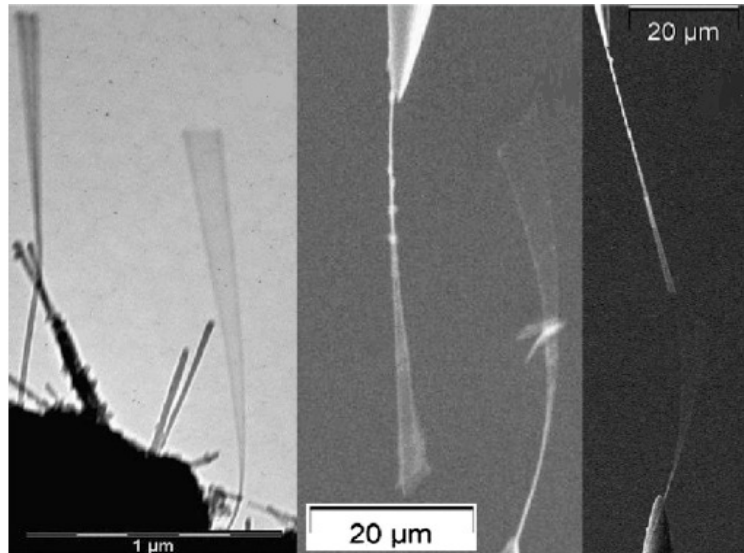
Feng *et al.* have studied the characteristic of the synchronization of mechanically coupled microcantilevers for increasing the sensitivity of the resonant sensors based on synchronization. Synchronizations of coupled cantilever structures by piezoceramic actuation were observed and the phase noise of the cantilever could be decreased. The frequency response signal was doubled from the low-frequency cantilever to the high-frequency cantilever by synchronization while the frequency fluctuation was almost the same, and the frequency fluctuation in coupled cantilevers can be decreased under synchronization. It is possible to enlarge the frequency response signal from the low-frequency cantilever to the high-frequency cantilever based on this kind of superharmonic synchronization while the frequency fluctuation was not amplified for resonant sensing applications. The resonant frequency shift measurement under magnetic force was achieved. The frequency shift of the low-frequency cantilever under external force can be enlarged by the coupled high-frequency cantilever based on synchronization [36].



**Figure 1.2 :** Optical micrograph of typical mechanically coupled resonators [36].

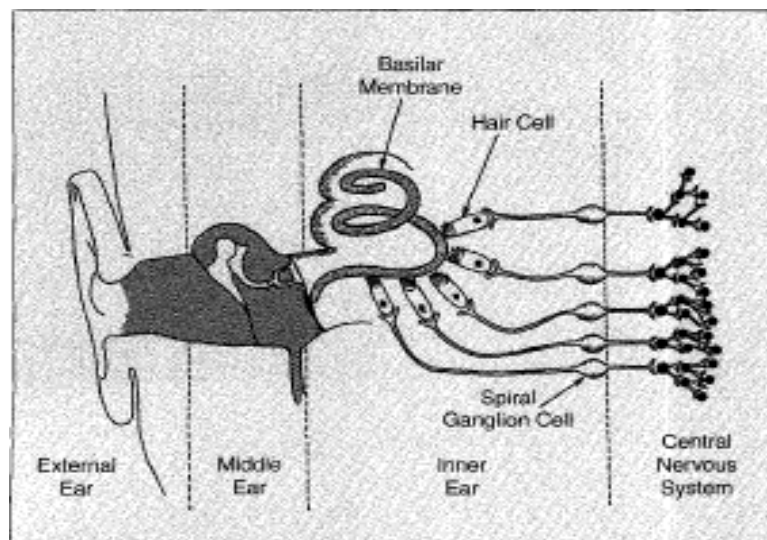
Perisanu *et al.* have presented an experimental study of the electrostatic coupling between the mechanical resonances of two nanowires or two nanotubes as shown in Fig. 1.3. This coupling occurs when the Eigen frequencies of the two resonators are matched by electrostatic tuning and it changes from a weak coupling to a strong coupling regime as the distance between the cantilevers is decreased. Linear coupling theory is shown to be in excellent agreement with the experimental data [37].





**Figure 1.3 :** Electrostatically coupled nanocantilevers [37].

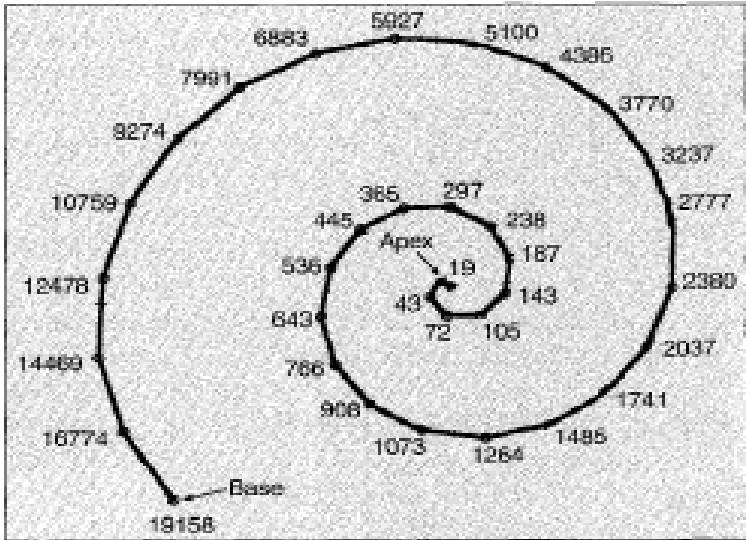
We are also observed the movement and energy transfer with Mechanical Resonance Absorption (MRA) in mechanisms in the hearing of humans and animals. If we examine in some detail the human ear and the hearing system. Vibration waves in particular frequencies, which make up sounds emerging from any source are moved up to our ears by air molecules. Waves of sprawling vibration goes the external ear and the way of the ear and vibrate eardrum as seen in figure1.4. Vibrating the eardrum transfer these vibration waves to perilymph fluid in cochlear situated in the inner ear by means of the hammer, Anvil and stirrup, which acts as amplifier and located in the middle ear. Waves of vibration occurring in the fluid moves through the cochlear and vibrates the basilar membrane located in the cochlear [38].



**Figure 1.4 :** Schematic illustration of the human ear [38].

Frequency coding takes place in organ of the cochlear. As shown the basal membrane diagram in Figure 1.5, coming vibrations of different frequencies cause the maximum amplitude vibrations at different points along the basal membrane with MRA. Vibration waves, generated by low frequency sounds in the cochlea fluid, will lead to displacement with the largest amplitude at the top of basal membrane (apex, Figure 1.5). High-frequency sounds constitute vibration waves madding displacement with the largest amplitude in the bottom of the basement membrane (base, see Figure 1.5). If signals consists of multiple frequencies, these moving waves will form the maximum displacement at different points along the membrane with MRA.

Cochlear behaves as a frequency encoding mechanism of hearing system by decomposing the complex frequency of sound waves. Each location or place of over the basilar membrane gives the best answer for a specific frequency between 20-20000 Hz. A certain position on the basal membrane vibrates with maximum amplitude depending on the frequency of the drive. Hair cells bent by displacement occurring in the membrane incentives to neighboring nerve fibers arranged according to very sensitive frequencies. Thus, messages are converted into electric signals and transmitted to the brain. Understanding of sound is provided by processing these signals in the brain [38].



**Figure 1.5 :** Basilar membrane diagram showing the locations maximum displacement in the different sinusoidal frequency responses basilar [38].

All of the abovementioned methods focus on the macro-scale mechanical structures, but there is not any studies about motion and energy transfer between nano-scale structures (e.g. nano-scale cantilever beams). Actually, in case of using *MRA* in the

micro / nano-sized structures, motion and energy losses taking place during the transfer will be much smaller depending on small dimensions compared to the macro-scale structure and to use structures in close proximity to each other. Therefore, the use of *MRA* in miniature sizes can occur much more effective and functional way. Based on this motivation, the first time in this project, study of energy transfer between nano-scale cantilever beams with the help of the resonance frequency is recommended. This proposed project will be carried out numerical. Thereby, energy transfer between nano-scale cantilever beams will be observed with the mechanical energy coupling without contact.

In this study, it are attempted to give a new technique to literature by studying on basic descriptive parameters of the movement and the energy and controlling of the efficiency or making adjustable.



## 2. BEAM THEORIES

### 2.1 Introduction

In this chapter, first, static and dynamic behavior of beams are explained by the general forms of Euler Bernoulli, Rayleigh and Timoshenko Beam Theories, and their distinction and reasons for preference are described. Then, free and forced vibration equations and formulations used for calculation of the transverse vibrations of beams are mentioned to examine their dynamic behavior. Calculation of analytical natural frequencies is presented. The obtainment of  $\beta nL$  values utilized in the calculation of natural frequency are shown for doubly-clamped beams in detail, and these values achieved under different boundary conditions are also submitted in the table.

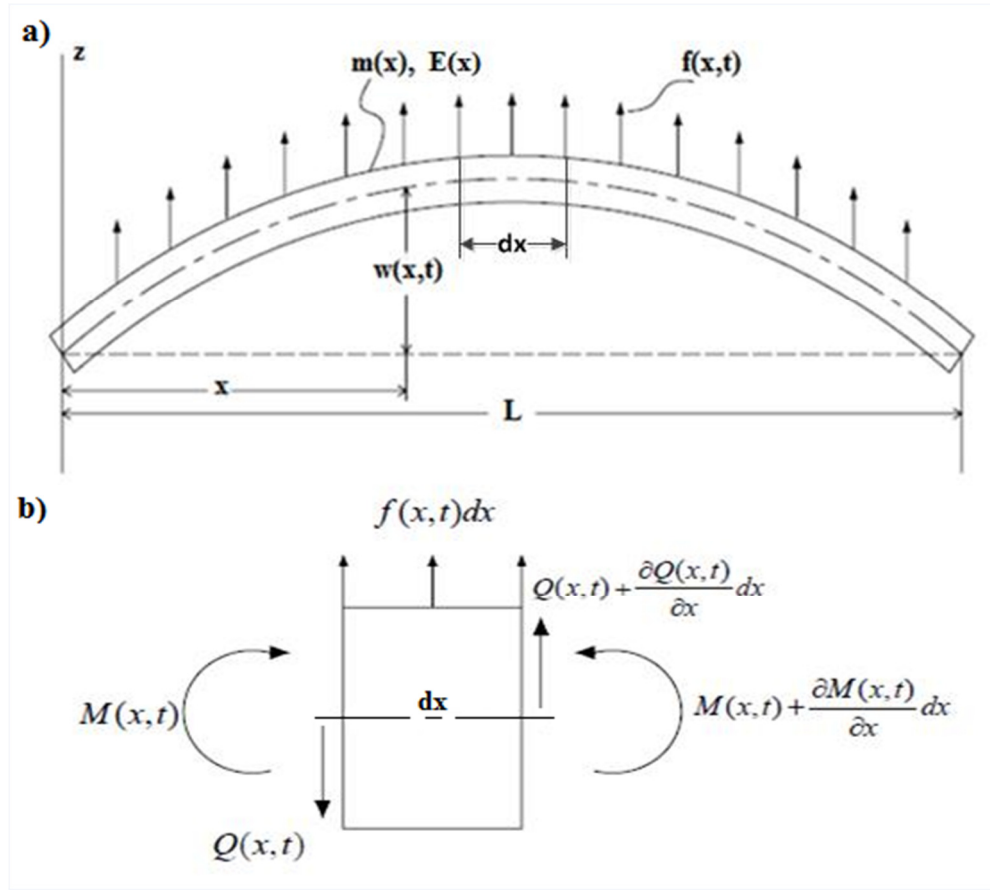
### 2.2 Static Analysis

#### 2.2.1 Euler-Bernoulli Theory

The Euler-Bernoulli beam model includes the strain energy due to bending and kinetic energy due to lateral displacement. In this theory, the inertial force due to transverse translation is taken into account, and those due to shear deflection and rotation are neglected. Since shear is neglected, rotation of the differential element becomes small compared to both its translation and the angular distortion. The cross-sections remain in the plane and orthogonal to the mid-plane of the beam after deformation.

Newton's Second Law is used to derive the equation of motion. The equation of motion can also be obtained using Hamilton's variational principle [39] based on the beam and its differential element as shown in Figs. 2.1a and 2.1b, respectively.

In Fig. 2.1,  $M(x,t)$ ,  $Q(x,t)$ ,  $f(x,t)$ ,  $m(x)$ ,  $E$  denote the bending moment, the shear force, the transverse force density, the mass per unit length, and the modulus of elasticity, respectively.



**Figure 2.1 :** a) Beam in bending. b) Free-body diagram for an element [40].

The equilibrium equation for the forces in the vertical direction of the beam in bending, hence, can be expressed as:

$$\left( Q(x,t) + \frac{\partial Q(x,t)}{\partial x} dx \right) - Q(x,t) + f(x,t)dx = m(x) \frac{\partial^2 w(x,t)}{\partial t^2} dx \quad (2.1)$$

$$0 < x < L$$

Moreover, assuming the mass moment of inertia and the angular acceleration of the element are negligible, the equilibrium equation for the moments of the beam element in bending is given by:

$$\left( M(x,t) + \frac{\partial M(x,t)}{\partial x} dx \right) - M(x,t) + \left( Q(x,t) + \frac{\partial Q(x,t)}{\partial x} dx \right) dx + f(x,t)dx \frac{dx}{2} = 0, \quad 0 < x < L \quad (2.2)$$

By ignoring the second-order dx terms in Eq. (2.2), inserting it in Eq. (2.1), dividing Eq. (2.1) by dx, and canceling all appropriate terms we end up with the following equation:

$$-\frac{\partial^2 M(x,t)}{\partial x^2} + f(x,t) = m(x) \frac{\partial^2 w(x,t)}{\partial t^2}, \quad 0 < x < L \quad (2.3)$$

Equation (2.3) relates the bending moment  $M(x,t)$  and transverse force density  $f(x,t)$  to the bending deflection of  $w(x,t)$ .  $M(x,t)$  can also be written as a function of  $w(x,t)$  in the form of:

$$M(x,t) = -EI(x) \frac{\partial^2 w(x,t)}{\partial x^2} \quad (2.4)$$

where  $I(x)$  is the moment of inertia along the length of the beam. By placing Eq. (2.4) in Eq. (2.3), we can obtain a relationship between the displacement and transverse force density alone, expressed as:

$$-\frac{\partial^2}{\partial x^2} \left( EI(x) \frac{\partial^2 w(x,t)}{\partial x^2} \right) + f(x,t) = m(x) \frac{\partial^2 w(x,t)}{\partial t^2}, \quad 0 < x < L \quad (2.5)$$

Equation (2.5) is a fourth-order partial differential equation governing the bending vibrations of beams. The equation of motion with boundary conditions form a boundary value problem solvable by the method of separation of variables. To complete the boundary value problem, two boundary conditions for each end of the beam have to be specified. These boundary conditions can be classified as essential and natural ones. For a beam governed by a fourth-order differential equation, essential boundary conditions consist of equations containing the displacement function and its first derivative, whereas the natural boundary conditions consist of the second and third derivative.

For fixed ends, the deflection and its slope are zero causing the essential boundary conditions to be:

$$w(x,t) = 0, \quad \text{at } x = 0 \text{ and } x = L \quad (2.6)$$

$$\frac{\partial w}{\partial x} = 0, \quad \text{at } x = 0 \text{ and } x = L \quad (2.7)$$

The constrained equations satisfying these classical boundary conditions are homogenous. There are several other types of beam-ends for which various boundary conditions can be written. For those with sliding ends, restrained by translational or rotational springs, and beams resting on elastic foundations, other boundary equations arise.

In the absence of external excitations, the beam is vibrating freely and the term corresponding to the transverse force density  $f(x, t)$  in the governing partial differential equation is set to zero, so that Eq. (2.5) reduces to:

$$m(x) \frac{\partial^2 w(x, t)}{\partial t^2} + \frac{\partial^2}{\partial x^2} \left( EI(x) \frac{\partial^2 w(x, t)}{\partial x^2} \right) = 0 \quad (2.8)$$

$$0 < x < L$$

By taking the terms  $m(x)$  and  $EI(x)$  as constants for uniform beams, Eq. (2.8) is reduced to:

$$\frac{\partial^4 w(x, t)}{\partial x^4} + \frac{m}{EI} \frac{\partial^2 w(x, t)}{\partial t^2} = 0 \quad 0 < x < L \quad (2.9)$$

Equation (2.9) can be rewritten as:

$$\frac{\partial^4 w(x, t)}{\partial x^4} + \frac{1}{D_0^4} \frac{\partial^2 w(x, t)}{\partial t^2} = 0 \quad (2.10)$$

$$D_0^4 = \frac{EI}{m} \quad (2.11)$$

The next step is to apply separation of variables to the term  $w(x, t)$  in the spatial variable  $x$  and time  $t$ . Because the beam is assumed to do a synchronous motion during vibration, its shape or profile remains, same except the profile amplitude change with time under vibration.

If we assume that the displacement changes as  $y = e^{i(k_w x - \omega_n t)}$ , where  $k_w$  is constant wave number ( $k_w = 2\pi/\text{wavelength}$ ), and  $\omega_n$  is the natural frequency of vibration, then the dispersive relationship between  $k_w$  and  $\omega_n$  may be given as follows [40]:



$$k_w^4 = \frac{\omega_n^2}{D_0^4} = k_0^4 \quad (2.12)$$

where  $k_0$  is the wave number for Euler-Bernoulli rod.

The degree of accuracy of the theory may be evaluated by its dispersive curve  $k_w$  versus  $\omega_n$ , and its comparison with the exact dispersive curve. The corresponding curve to a dispersive equation is also referred to as propagation constant-frequency curve. The elementary Euler-Bernoulli Beam Theory is valid if the ratio between the length of the beam and its depth is relatively large [39]. This theory, however, tends to slightly overestimate the natural frequencies [41].

### 2.2.2 Rayleigh Theory

This theory includes the effect of rotary inertia of the beam cross-section, and provides an improvement to Euler-Bernoulli Beam Theory [40]. It is assumed that the cross-sections of the beam remain planar and orthogonal to the neutral axis (midplane) of the beam.

The governing differential equation of transverse vibration according to Rayleigh Theory is given as follows:

$$\frac{\partial^4 w(x,t)}{\partial x^4} + \frac{1}{D_0^4} \frac{\partial^2 w(x,t)}{\partial t^2} - \frac{1}{c_b^2} \frac{\partial^4 w(x,t)}{\partial x^2 \partial t^2} = 0 \quad (2.13)$$

$$c_b^2 = \frac{E}{\rho} \quad (2.14)$$

Where  $c_b$  is the longitudinal wave velocity in the Euler-Bernoulli rod and  $\rho$  is density. The third term of the left side of Eq. (2.14) represents the effect of rotary inertia. The dispersive equation is given as follows [40]:

$$2k_{w/2}^2 = k_b^2 \pm \sqrt{k_b^4 + 4k_0^4} \quad (2.15)$$

$$k_b^2 = \frac{\omega_n}{c_b^2} \quad (2.16)$$

where  $k_b$  is the longitudinal wave number and  $k_0$  is the wave number for Euler-Bernoulli beam as aforementioned.

### 2.2.3 Euler-Bernoulli Modified Theory or Shear Model

In Euler-Bernoulli Modified Theory, also called as Shear Model, the effect of shear distortion is taken into account but the effect of rotational inertia is neglected. In this case, as seen in Fig. 2.2, the cross-sections of the beam remain planar but not orthogonal to the neutral axis because of the shear deformation.

The governing differential equation for transverse vibration of the beam is given by:

$$\frac{\partial^4 w(x,t)}{\partial x^4} + \frac{1}{D_0^4} \frac{\partial^2 w(x,t)}{\partial t^2} - \frac{1}{c_t^2} \frac{\partial^4 w(x,t)}{\partial x^2 \partial t^2} = 0 \quad (2.17)$$

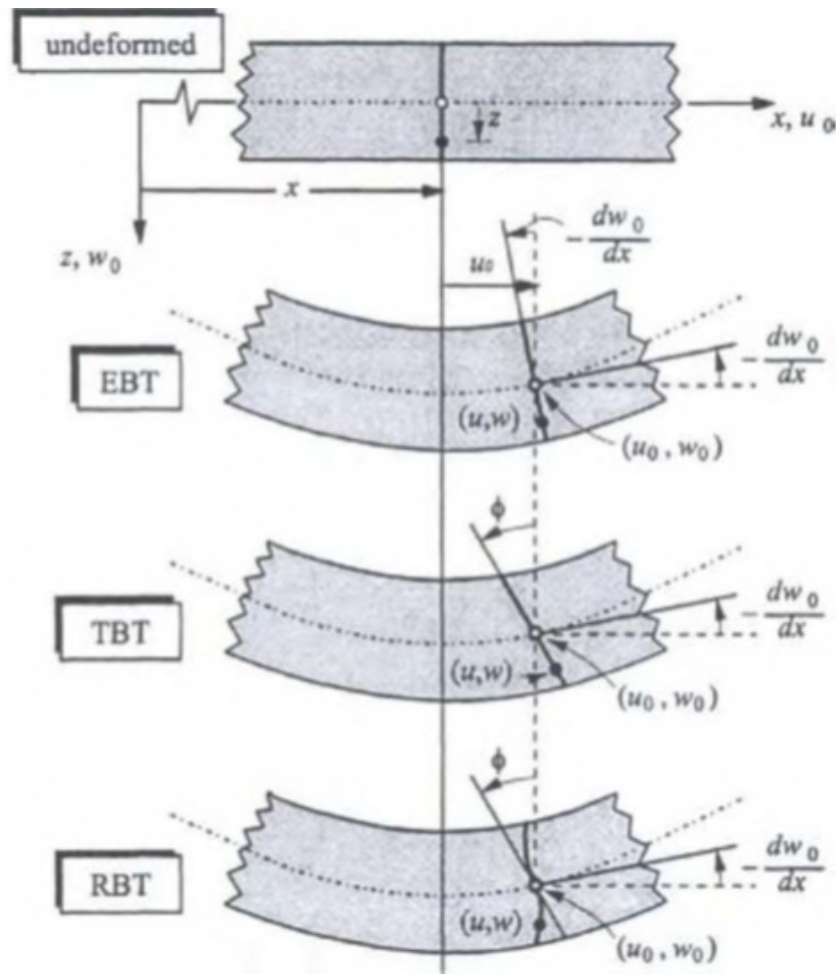
$$c_t^2 = \frac{G}{\rho} \quad (2.18)$$

where  $G$  is the shear modulus, which replaces the elasticity modulus  $E$  in the differential equation of Rayleigh Theory,  $c_t$  is the velocity of the shear waves in the thin rod.

The dispersive relationship is given by:

$$2k_{w/2}^2 = k_t^2 \pm \sqrt{k_t^4 + 4k_0^4} \quad (2.19)$$

$$k_t^2 = \frac{\omega_n}{c_t^2} \quad (2.20)$$



**Figure 2.2 :** Deformation of a typical transverse normal line in various beam theories[43].

### 2.2.4 Timoshenko Theory

In elementary Euler-Bernoulli Beam Model, the cross-sectional dimensions of the beam are assumed to be small compared to its length so that the rotary inertia and shear deflection are neglected.

However, the effect of cross-sectional dimensions on the vibration frequency becomes important when studying higher frequencies vibrations, if the beam is subdivided into shorter portions. Therefore, in Timoshenko Theory, the effect of shearing force, rotary inertia and their combined effects are added to the Euler-Bernoulli Beam Model [42]. Because the beam element does not only undergo translational motion during vibration, but also the effect of rotation is taken into account by modification of the corresponding terms. The moment exerted by inertial forces about the axis through the center of gravity of the beam element in Fig. 2.1b, is given by:

$$I\rho \frac{\partial^3 w}{\partial x \partial t^2} dx \quad (2.21)$$

such that the first derivative of bending moment is given by:

$$\frac{\partial M(x,t)}{\partial x} = - \left( Q - I\rho \frac{\partial^3 w}{\partial x \partial t^2} dx \right) \quad (2.22)$$

If we differentiate Eq. (2.4) twice with respect to  $x$ , then:

$$\frac{\partial^2 M(x,t)}{\partial x^2} = EI(x) \frac{\partial^4 w(x,t)}{\partial t^4} \quad (2.23)$$

By inserting Eq. (2.22) into Eq. (2.23):

$$EI(x) \frac{\partial^4 w(x,t)}{\partial x^4} = -m \frac{\partial^2 w(x,t)}{\partial t^2} + I\rho \frac{\partial^4 w(x,t)}{\partial x^2 \partial t^2} \quad (2.24)$$

Because the slope of the deflection curve depends on the rotation of the cross-section as well as on the shear, more accurate results for vibration are obtained if the deflection due to shear is also taken into account. If the angle of beam rotation, when the shear force is neglected, is denoted by  $\psi$  and the shear angle of the cross-section of the beam is  $\varphi$ , then the total angle is expressed as:

$$\frac{\partial w(x,t)}{\partial x} = \psi + \varphi \quad (2.25)$$

The bending moment and shear force are:

$$M(x,t) = EI(x) \frac{\partial \psi(x,t)}{\partial x} \quad (2.26)$$

$$Q = k' \psi AG = k' \left( \frac{\partial w(x,t)}{\partial x} - \psi(x,t) \right) AG \quad (2.27)$$

In the equations,  $k'$  represents a numerical factor that depends on the shape of the cross-section and also called as shear coefficient.

For a rectangular cross-section, it is taken as  $k' = 2/3$  [42]. The final form of the governing differential equation of Timoshenko Theory for translational vibration of the beam is given by:

$$EI(x) \frac{\partial^4 w(x,t)}{\partial x^4} + \rho A \frac{\partial^2 w(x,t)}{\partial t^2} - \left( I\rho + \frac{EI\rho}{k'G} \right) \frac{\partial^4 w(x,t)}{\partial x^2 \partial t^2} + \rho I \frac{\rho}{k'G} \frac{\partial^4 w(x,t)}{\partial t^4} = 0 \quad (2.28)$$

In another formulation, Eq. (2.28) can be rewritten as:

$$\frac{\partial^4 w(x,t)}{\partial x^4} + \frac{1}{D_0^4} \frac{\partial^2 w(x,t)}{\partial t^2} - \left( \frac{1}{c_b^2} + \frac{1}{k'c_t^2} \right) \frac{\partial^4 w(x,t)}{\partial x^2 \partial t^2} + \frac{1}{k'c_b^2 c_t^2} \frac{\partial^4 w(x,t)}{\partial t^4} = 0 \quad (2.29)$$

The fundamental difference between Bress and Volterra Theories on one hand and the Timoshenko Theory on the other is that in Timoshenko Theory the correction factor is introduced in the initial equations, whereas in other theories it appears as a result of shear and rotary effects. In Timoshenko Theory, constant state of transverse shear strain and thus constant shear stress with respect to the thickness coordinate is included. Therefore, the Timoshenko Beam Theory requires shear correction factor  $k'$  to compensate the error due to the constant shear stress assumption. The dispersive relationship, then, can be stated as:

$$2k_{w1/2}^2 = k_b^2 + \frac{k_t^2}{k'} \pm \sqrt{\left( k_b^2 - \frac{k_t^2}{k'} \right)^2 + 4k_0^4} \quad (2.30)$$

Timoshenko Model describes the vibration of short beams or high modes of a thin beam with high precision [41].

## 2.3 Dynamic Analysis

### 2.3.1 Vibration of a Single Degree-of-Freedom (DOF) System

The number of degrees of freedom of a vibrating system is defined by the minimum number of displacement components required to describe the configuration of the system during vibration. The essential features of vibrating system include (1) a mass  $m$  producing an inertial force  $m\ddot{x}$ , (2) stiffness of a spring  $k$  producing a restoring force  $kx$ , and (3) a damping mechanism that dissipates the energy. If the equivalent viscous damping coefficient is denoted as  $c$ , the damping force produced is  $c\dot{x}$ [44].

#### 2.3.1.1 Free Vibration

In the absence of damping, the equation of motion of a single degree-of-freedom system is given by;

$$m\ddot{x} + kx = f(t) \quad (2.31)$$

where  $f(t)$  is the force acting on the mass and  $x(t)$  is the displacement of the mass  $m$ . The free vibration of system, in the absence of forcing function  $f(t)$ , is governed by the equation;

$$m\ddot{x} + kx = 0 \quad (2.32)$$

The solution of Eq. (2.32) is;

$$x(t) = x_0 \cos \omega_n t + \frac{\dot{x}_0}{\omega_n} \sin \omega_n t \quad (2.33)$$

where  $\omega_n$  is the natural frequency of the system, and is given by;

$$\omega_n = \sqrt{\frac{k}{m}} \quad (2.34)$$

$x_0 = x(t = 0)$  is the initial displacement and  $\dot{x}_0 = \frac{dx(t=0)}{dt}$  is the initial velocity of the system. Eq. (2.34) can also be expressed as;

$$x(t) = A \cos(\omega_n t - \phi) \quad (2.35)$$

$$x(t) = A \sin(\omega_n t + \phi_0) \quad (2.36)$$

where;

$$A = \left[ x_0^2 + \left( \frac{\dot{x}_0}{\omega_n} \right)^2 \right]^{1/2} \quad (2.37)$$

$$\phi = \tan^{-1} \frac{\dot{x}_0}{x_0 \omega_n} \quad (2.38)$$

$$\phi_0 = \tan^{-1} \frac{x_0 \omega_n}{\dot{x}_0} \quad (2.39)$$

The equation of motion for the vibration of a viscously damped system is given by;

$$m\ddot{x} + c\dot{x} + kx = f(t) \quad (2.40)$$

By dividing throughout by  $m$ , Eq. (2.40) can be rewritten as;

$$\ddot{x} + 2\zeta\omega_n\dot{x} + \omega_n^2x = F(t) \quad (2.41)$$

where  $\zeta$  is the damping ratio, given by;

$$\zeta = \frac{c}{2m\omega_n} = \frac{c}{c_c} \quad (2.42)$$

where  $c_c$  is known as the critical damping constant :

$$c_c = 2m\omega_n = 2\sqrt{km} \quad (2.43)$$

and

$$F(t) = \frac{f(t)}{m} \quad (2.44)$$

The system is considered to be underdamped, critically damped, and overdamped if the value of the damping ratio is less than 1, equal to 1, and greater than 1, respectively.

The free vibration of a damped system is governed by the equation,

$$\ddot{x} + 2\zeta\omega_n\dot{x} + \omega_n^2x = 0 \quad (2.45)$$

The free vibration response of the system [i.e., the solution of Eq. (2.45)], with different levels of the damping can be expressed as follows:

1. Underdamped system ( $\zeta < 1$ ):

$$x(t) = e^{-\zeta\omega_n t} \left( x_0 \cos \omega_d t + \frac{\dot{x}_0 + \zeta\omega_n x_0}{\omega_d} \sin \omega_d t \right) \quad (2.46)$$

where  $x_0 = x(t = 0)$  is the initial displacement and  $\dot{x}_0 = dx(t = 0) / dt$  is the initial velocity, and  $\omega_d$  is the frequency of damped vibration given by;

$$\omega_d = \omega_n \sqrt{(1 - \zeta^2)} \quad (2.47)$$

2. Critically damped system ( $\zeta = 1$ ):

$$x(t) = [x_0 + (\dot{x}_0 + \omega_n x_0)t] e^{-\omega_n t} \quad (2.48)$$

3. Overdamped system ( $\zeta > 1$ ):

$$x(t) = C_1 e^{(-\zeta + \sqrt{\zeta^2 - 1})\omega_n t} + C_2 e^{(-\zeta - \sqrt{\zeta^2 - 1})\omega_n t} \quad (2.49)$$

where

$$C_1 = \frac{x_0 \omega_n (\zeta + \sqrt{\zeta^2 - 1}) + \dot{x}_0}{2\omega_n \sqrt{\zeta^2 - 1}} \quad (2.50)$$

$$C_2 = \frac{-x_0 \omega_n (\zeta - \sqrt{\zeta^2 - 1}) - \dot{x}_0}{2\omega_n \sqrt{\zeta^2 - 1}} \quad (2.51)$$

### 2.3.1.2 Free Vibration Under Harmonic Force

For an undamped system subjected to the harmonic force  $f(t) = f_0 \cdot \cos \omega t$ , the equation of motion is [44];

$$m\ddot{x} + kx = f_0 \cdot \cos \omega t \quad (2.52)$$



where  $f_0$  is the magnitude and  $\omega$  is the frequency of the applied force. The steady-state solution or the particular integral of Eq. (2.52) is;

$$x_p(t) = X \cos \omega t \quad (2.53)$$

where

$$X = \frac{f_0}{k - m\omega^2} = \frac{\delta_{st}}{1 - (\omega/\omega_n)^2} \quad (2.54)$$

Denotes the maximum amplitude of the steady-state response and

$$\delta_{st} = \frac{f_0}{k} \quad (2.55)$$

Indicates the static deflection of the mass under the force  $f_0$ . The ratio

$$\frac{X}{\delta_{st}} = \frac{1}{1 - (\omega/\omega_n)^2} \quad (2.56)$$

Represents the ratio of the dynamic to static amplitude of motion, and is called the amplification factor, magnification factor, or amplitude ratio. The general solution of Eq. (2.52) including the homogeneous solution and the particular integral becomes;

$$\begin{aligned} x(t) = & \left( x_0 - \frac{f_0}{k - m\omega^2} \right) \cos \omega_n t + \frac{\dot{x}_0}{\omega_n} \sin \omega_n t \\ & + \frac{f_0}{k - m\omega^2} \cos \omega_n t \end{aligned} \quad (2.57)$$

At resonance,  $\omega/\omega_n = 1$ , and the solution given by Eq. (2.57) can be expressed as;

$$x(t) = x_0 \cos \omega_n t + \frac{\dot{x}_0}{\omega_n} \sin \omega_n t + \frac{\delta_{st} \omega_n t}{2} \sin \omega_n t \quad (2.58)$$

When a viscously damped system is subjected to the harmonic force,  $f(t) = f_0 \cdot \cos \omega t$ , the equation of motion becomes;

$$m\ddot{x} + c\dot{x} + kx = f_0 \cdot \cos \omega t \quad (2.59)$$

The particular solution of Eq. (2.59) can be expressed as;

$$x_p(t) = X \cos(\omega t - \phi) \quad (2.60)$$

where  $X$  is the amplitude and  $\phi$  is the phase angle denoted by;

$$X = \frac{f_0}{\left[ (k - m\omega^2)^2 + c^2\omega^2 \right]^{1/2}} = \frac{\delta_{st}}{\left[ (1 - r^2)^2 + (2\zeta r)^2 \right]^{1/2}} \quad (2.61)$$

$$\phi = \tan^{-1} \frac{c\omega}{k - m\omega^2} = \tan^{-1} \frac{2\zeta r}{1 - r^2} \quad (2.62)$$

where

$$\delta_{st} = \frac{f_0}{k} \quad r = \frac{\omega}{\omega_n} \quad (2.63)$$

Indicates the frequency ratio, and

$$\zeta = \frac{c}{c_c} = \frac{c}{2\sqrt{mk}} = \frac{c}{2m\omega_n} \quad (2.64)$$

Represents the damping ratio. The variations of the amplitude ratio or magnification factor,

$$\frac{X}{\delta_{st}} = \frac{1}{\sqrt{(1 - r^2)^2 + (2\zeta r)^2}} \quad (2.65)$$

and the phase angle ratio,  $\phi$ , given by Eq. (2.29), with the frequency ratio,  $r$ .

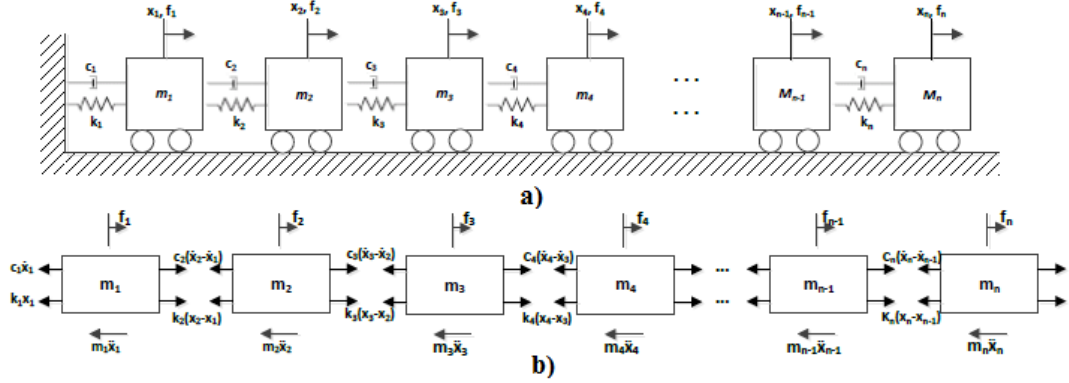
The general solution of Eq. (2.59) including the homogeneous solution and the particular integral, in the case of an underdamped system, can be expressed as;

$$x(t) = X_0 e^{-\zeta\omega_n t} \cos(\omega_d t - \phi_0) + X \cos(\omega t - \phi) \quad (2.66)$$

### 2.3.2 Vibration of Multidegree-of-Freedom System

A typical  $n$ -degree-of-freedom system is shown in Fig. 2.3a. For multidegree of freedom systems, it is more convenient to use matrix notation in expression of the equations of motion and describe the vibrational response. Let  $x_i$  denote the displacement of mass  $m_i$  measured from its static equilibrium position for  $i = 1, 2, \dots, n$ .

The equation of motion of the n-degree-of-freedom system shown in Fig. 2.3a can be derived from the free-body diagram of the masses shown in Fig. 2.3b, and can be expressed in the matrix form as [44];



**Figure 2.3 :** a) An n-degree-of-freedom system.b) free-body diagrams of the masses [44].

$$[m]\ddot{\vec{x}} + [c]\dot{\vec{x}} + [k]\vec{x} = \vec{f} \quad (2.67)$$

where  $[m]$ ,  $[c]$ , and  $[k]$  denote the mass, damping, and stiffness matrices, respectively:

$$[m] = \begin{bmatrix} m_1 & 0 & 0 & \dots & 0 \\ 0 & m_2 & 0 & \dots & 0 \\ 0 & 0 & m_3 & \dots & 0 \\ \vdots & & & \ddots & \\ 0 & 0 & 0 & \dots & m_n \end{bmatrix} \quad (2.68)$$

$$[c] = \begin{bmatrix} c_1 + c_2 & -c_2 & 0 & \dots & 0 \\ -c_2 & c_2 + c_3 & -c_3 & \dots & 0 \\ 0 & -c_3 & c_3 + c_4 & \dots & 0 \\ \vdots & \vdots & \vdots & \ddots & \vdots \\ 0 & 0 & 0 & -c_n & c_n \end{bmatrix} \quad (2.69)$$

$$[k] = \begin{bmatrix} k_1 + k_2 & -k_2 & 0 & \cdots & 0 \\ -k_2 & k_2 + k_3 & -k_3 & \cdots & 0 \\ 0 & -k_3 & k_3 + k_4 & \cdots & 0 \\ \vdots & \vdots & \vdots & \ddots & \vdots \\ 0 & 0 & 0 & -k_n - 1 & k_n \end{bmatrix} \quad (2.70)$$

The vectors  $\vec{x}$ ,  $\dot{\vec{x}}$  and  $\ddot{\vec{x}}$  indicate, respectively, the vectors of displacements, velocities, and accelerations of the various masses, and  $\vec{f}$  represents the vector of forces acting on the masses:

$$\vec{x} = \begin{Bmatrix} x_1 \\ x_2 \\ x_3 \\ \vdots \\ x_n \end{Bmatrix}, \quad \dot{\vec{x}} = \begin{Bmatrix} \dot{x}_1 \\ \dot{x}_2 \\ \dot{x}_3 \\ \vdots \\ \dot{x}_n \end{Bmatrix}, \quad \ddot{\vec{x}} = \begin{Bmatrix} \ddot{x}_1 \\ \ddot{x}_2 \\ \ddot{x}_3 \\ \vdots \\ \ddot{x}_n \end{Bmatrix}, \quad \vec{f} = \begin{Bmatrix} f_1 \\ f_2 \\ f_3 \\ \vdots \\ f_n \end{Bmatrix} \quad (2.71)$$

where a dot over  $x_i$  represents its time derivative.

Note that the spring-mass-damper system shown in Fig. 2.3 is a particular case of a general n-degree-of-freedom system. In their general form, the mass, damping, and stiffness matrices in Eq. (2.67) are fully populated and can be expressed as;

$$[m] = \begin{bmatrix} m_{11} & m_{12} & m_{13} & \cdots & m_{1n} \\ m_{12} & m_{22} & m_{23} & \cdots & m_{2n} \\ m_{13} & m_{23} & m_{33} & \cdots & m_{3n} \\ \vdots & & & \ddots & \\ m_{1n} & m_{2n} & m_{3n} & \cdots & m_{nn} \end{bmatrix} \quad (2.72)$$

$$[c] = \begin{bmatrix} c_{11} & c_{12} & c_{13} & \cdots & c_{1n} \\ c_{12} & c_{22} & c_{23} & \cdots & c_{2n} \\ c_{13} & c_{23} & c_{33} & \cdots & c_{3n} \\ \vdots & & & \ddots & \\ c_{1n} & c_{2n} & c_{3n} & \cdots & c_{nn} \end{bmatrix} \quad (2.73)$$

$$[k] = \begin{bmatrix} k_{11} & k_{12} & k_{13} & \cdots & k_{1n} \\ k_{12} & k_{22} & k_{23} & \cdots & k_{2n} \\ k_{13} & k_{23} & k_{33} & \cdots & k_{3n} \\ \vdots & & & \ddots & \\ k_{1n} & k_{2n} & k_{3n} & \cdots & k_{nn} \end{bmatrix} \quad (2.74)$$

Equation (2.67) denotes a system with n-coupled second-order ordinary differential equations. These equations can be decoupled using a procedure called modal analysis, which requires the natural frequencies and normal modes or natural modes of the system. To determine the natural frequencies and normal modes, the Eigen value problem corresponding to the vibration of the undamped system is to be solved [44].

### 2.3.3 Transverse (Bending) Vibration of Beams

The equations of motion of a beam can be derived according to the Euler-Bernoulli, Rayleigh, and Timoshenko Theories. The Euler-Bernoulli Theory neglects the effects of rotary inertia and shear deformation, and is applicable to an analysis of thin beams. The Rayleigh Theory considers the effect of rotary inertia, and the Timoshenko Theory considers the effects of both rotary inertia and shear deformation. The Timoshenko Theory can be used for thick beams. The equations of motion for the transverse vibration of beams are in the form of fourth-order partial differential equations with two boundary conditions at each end. Possible boundary of the beam can involve spatial derivatives up to third order. In this section, the free vibration, including the determination of natural frequencies and mode shapes, is considered according to the Euler-Bernoulli Theory. When the deflection  $w(x,t)$  is assumed to be due to the bending moment only. Newton's Second Law is applied to the free body diagram of an element of the beam shown in Fig. 2.3. The dynamic force equation in the lateral direction is [44];

$$\rho A(x) \frac{\partial^2 w(x,t)}{\partial t^2} dx = - \left( Q + \frac{\partial Q}{\partial x} dx \right) + Q \quad (2.75)$$

$$\rho A(x) \frac{\partial^2 w(x,t)}{\partial t^2} dx = - \frac{\partial Q}{\partial x} \quad (2.76)$$

where  $m$  is the mass per unit length, and  $Q$  is the shear force. From strength of materials, it is known that the relation between bending moment and the shear force is;

$$\frac{\partial M}{\partial x} = Q \quad (2.77)$$

also the beam curvature and the bending moment is related by;

$$EI \frac{\partial^2 w(x,t)}{\partial x^2} = M \quad (2.78)$$

where  $EI$  is the flexural stiffness of the beam. Combining the above relations, the beam equation for its lateral vibration is;

$$\rho A \frac{\partial^2 w(x,t)}{\partial t^2} = - \frac{\partial^2}{\partial x^2} \left( EI \frac{\partial^2 w(x,t)}{\partial x^2} \right) \quad (2.79)$$

$$\frac{\partial^2 w(x,t)}{\partial t^2} + a^2 \frac{\partial^4 w(x,t)}{\partial x^4} = 0, \quad a^2 = \frac{EI}{\rho A} \quad (2.80)$$

Solution of the fourth order partial differential equation will give deflection  $w(x,t)$  as a function of  $x$  and  $t$ . The vibration solution can be found by separation of variables as;

$$w(x,t) = \phi(x).q(t) \quad (2.81)$$

Using Eq. (2.81) in Eq. (2.80) and rearranging yields,

$$-a^2 \frac{1}{\phi(x)} \frac{\partial^4 \phi(x)}{\partial x^4} = \frac{1}{q(t)} \frac{\partial^2 q(t)}{\partial t^2} \quad (2.82)$$

Left side of the equation is only a function of  $x$  and the right side is only a function of  $t$ . Letting each side of the equation be  $-\omega^2$ , where  $\omega$ , natural frequency, is constant.

Part dependent on  $x$  will give the following equation;

$$\frac{\partial^4 \phi(x)}{\partial x^4} - \beta^4 \phi(x) = 0 \quad (2.83)$$

Similarly, from the  $t$  dependent part;

$$\frac{\partial^2 q(t)}{\partial t^2} + \omega^2 q(t) = 0 \quad (2.84)$$

$$\beta^4 = \frac{\omega^2}{a^2} = \frac{\rho A \omega^2}{EI} \quad (2.85)$$

It can be shown from linear differential equations theory that the general solution will be in the following form;

$$\phi(x) = (C_1 \cosh \beta x + C_2 \sinh \beta x + C_3 \cos \beta x + C_4 \sin \beta x) \quad (2.86)$$

$$q(t) = (A \cos \omega t + B \sin \omega t) \quad (2.87)$$

The natural frequencies of the beam can be determined from Eq. (2.88) as,

$$\omega = \beta^2 \sqrt{\frac{EI}{\rho A}} = (\beta L)^2 \sqrt{\frac{EI}{\rho A L^4}} \quad (2.88)$$

The function  $\phi(x)$  is known as the normal mode or characteristic function of the beam and  $\omega$  is called as the natural frequency of vibrating beam. For any beam, there will be an infinite number of normal modes each with an associated natural frequency. The unknown constants,  $C_1$  to  $C_4$  in Eq. (2.86), and the value of  $\beta$  in Eq. (2.89) can be calculated by boundary conditions, and  $A$  and  $B$  can be calculated by initial conditions. If the natural frequencies and mode shapes of beams with a uniform cross section with different boundary conditions are examined, the common boundary conditions for the vibrating beam will be as given in Table 2.1.

If the natural frequency of lateral vibration of a both-end-fixed uniform beam is determined, general solution for lateral vibration of a beam is;

$$w(x, t) = (C_1 \cosh \beta x + C_2 \sinh \beta x + C_3 \cos \beta x + C_4 \sin \beta x) \quad (2.89)$$

\* $(A \cos \omega t + B \sin \omega t)$  from Eq.(2.86)

At the fixed end, the transverse displacement and the slope of the displacement are zero. Hence, the boundary conditions are;

$$x = 0 \quad w(0,t) = 0 \quad \text{and} \quad \frac{\partial w(0,t)}{\partial x} = 0 \quad (2.90)$$

**Table 2.1** : Boundary conditions of beams.

Boundary Conditions	Deflection	Slope	Moment	Shear
	$w(x,t)$	$\theta = \frac{\partial w}{\partial x}$	$M = EI \frac{\partial^2 w}{\partial x^2}$	$Q = EI \frac{\partial^3 w}{\partial x^3}$
<b>Fixed</b>	$w = 0$	$\theta = 0$		
<b>Free</b>			$M = 0$	$Q = 0$
<b>Hinged</b>	$w = 0$		$M = 0$	
<b>Spring Load</b>			$M = -k \frac{\partial w}{\partial x}$	$Q = kw$
<b>Inertia Load</b>			$M = 0$	$Q = m \frac{\partial^2 w}{\partial x^2}$

When Eq. (2.89) is used, the boundary conditions in Eq. (2.90) lead to,

$$C_1 = -C_3 \quad \text{and} \quad C_2 = -C_4 \quad (2.90)$$

Rewriting the deflection with these relations,

$$w(x,t) = [C_1 (\cosh \beta x - \cos \beta x) + C_2 (\sinh \beta x - \sin \beta x)] \quad (2.91)$$

\*( $A \cos \omega t + B \sin \omega t$ )

At right end boundary conditions;

$$\text{At } x = L \quad w(L,t) = 0 \quad \text{and} \quad \frac{\partial w(L,t)}{\partial x} = 0 \quad (2.92)$$

From these conditions, we get

$$w(L,t) = [C_1 (\cosh \beta L - \cos \beta L) + C_2 (\sinh \beta L - \sin \beta L)] * q(t) = 0 \quad (2.93)$$

$$\frac{\partial w(L,t)}{\partial x} = \beta [C_1 (\sinh \beta L + \sin \beta L) + C_2 (\cosh \beta L - \cos \beta L)] * q(t) = 0 \quad (2.94)$$



Equations (2.96) and (2.97) denote a system of two homogeneous algebraic equations with  $C_1$  and  $C_2$  as unknowns. For a nontrivial solution of  $C_1$  and  $C_2$ , we set the determinant of the coefficients of  $C_1$  and  $C_2$  in Eqs. (2.96) and (2.97) to zero in order to obtain,

$$\begin{vmatrix} (\cosh \beta L - \cos \beta L) & (\sinh \beta L - \sin \beta L) \\ (\sinh \beta L + \sin \beta L) & (\cosh \beta L - \cos \beta L) \end{vmatrix} = 0 \quad (2.95)$$

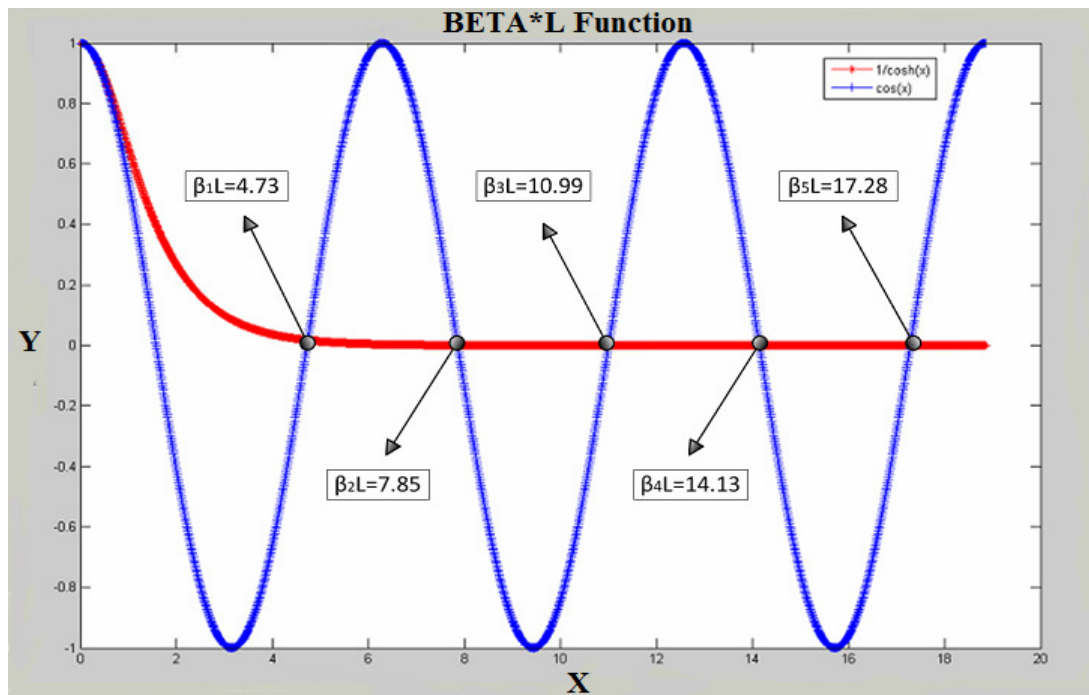
or

$$(\cosh \beta L - \cos \beta L)^2 + (\sinh^2 \beta L - \sin^2 \beta L) = 0 \quad (2.96)$$

Equation (2.96) can be simplified to obtain the frequency equation as,

$$\cosh \beta L \cos \beta L = 1 \quad (2.97)$$

This is a transcendental equation. If we let  $\cos \beta L = k_1$  and  $1/\cosh \beta L = k_2$  the equation is satisfied at  $k_1 = k_2$ . From the intersections as shown in Fig. 2.4.



**Figure 2.4 :**  $\beta L$  values for double-clamped boundary conditions.

Equation (2.93) gives,

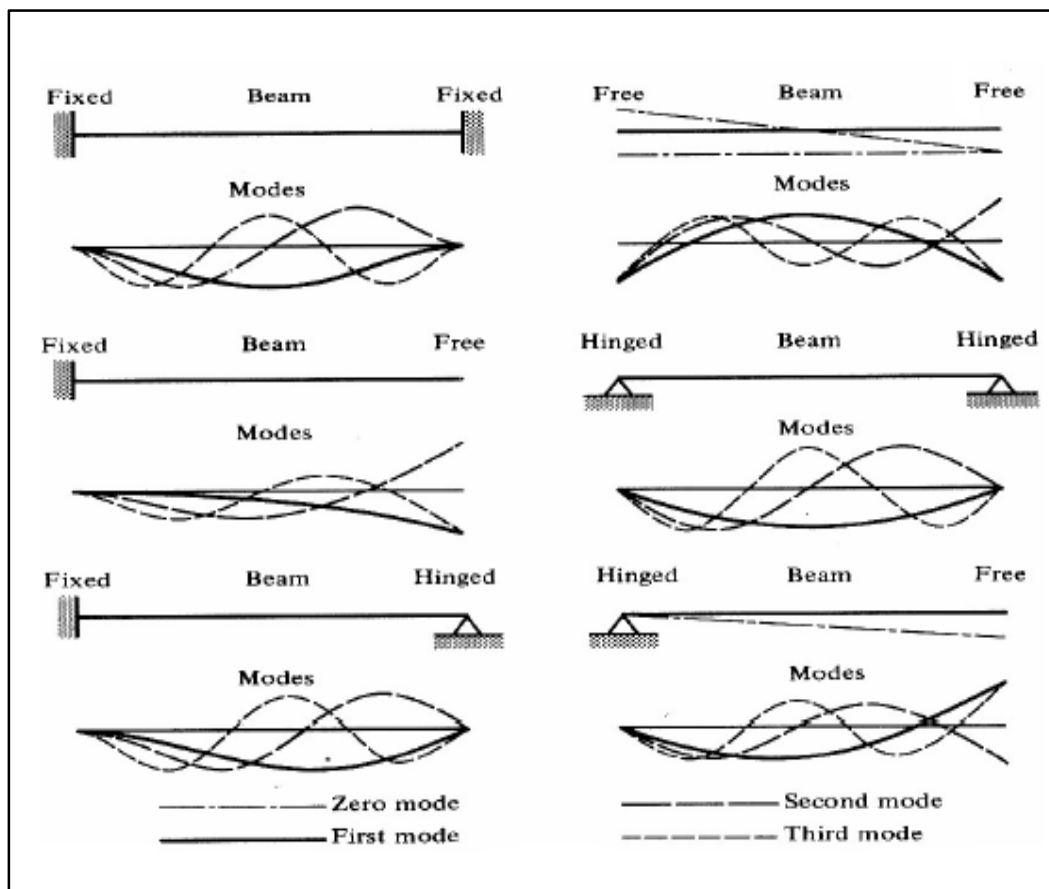
$$C_1 = -\frac{(\sinh \beta L - \sin \beta L)}{(\cosh \beta L - \cos \beta L)} C_2 \quad (2.98)$$

If  $\beta_n L$  denotes the  $n$ th root of the transcendental Eq. (2.97), the corresponding mode shape can be obtained by substituting Eqs. (2.90) and (2.98) into Eq. (2.89),

$$\phi_n(x) = C_n \left[ (\cosh \beta_n x - \cos \beta_n x) - \frac{\sinh \beta_n L - \sin \beta_n L}{\cosh \beta_n L - \cos \beta_n L} (\sinh \beta_n x - \sin \beta_n x) \right] \quad (2.99)$$

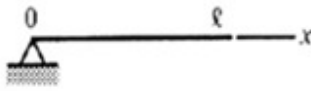


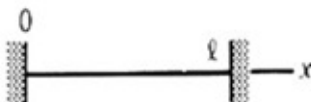

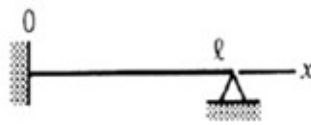
$$w(x,t) = \phi_n(x) \cdot (A \cos \omega_n t + B \sin \omega_n t)$$

The first four natural frequencies and the corresponding mode shapes for different boundary conditions are as shown in Fig. 2.5.



**Figure 2.5 :** Mode shapes for different boundary conditions.

Expressions of the vibrating beams with different boundary conditions are obtained by applying the same process as shown Fig.2.6.

END CONDITIONS	EQUATIONS
	(1) $w(0,t) = w'(0,t) = w(l,t) = w''(l,t) = 0$ (2) $\tan \beta l = \tanh \beta l^*$ (3) $\phi(x) = A \sin \beta x + \sinh \beta x$  $A = \frac{\sinh \beta l}{\sin \beta l} = \frac{\cosh \beta l}{\cos \beta l}$
	(1) $w(0,t) = w''(0,t) = w(l,t) = w''(l,t) = 0$ (2) $\sin \beta l = 0$ (3) $\phi(x) = A \sin \beta x$
	(1) $w(0,t) = w'(0,t) = w''(l,t) = w'''(l,t) = 0$ (2) $\cos \beta l \cosh \beta l = -1$ (3) $\phi(x) = A(\cos \beta x - \cosh \beta x) + (\sin \beta x - \sinh \beta x)$  $A = -\frac{\sin \beta l + \sinh \beta l}{\cos \beta l + \cosh \beta l} = \frac{\cos \beta l + \cosh \beta l}{\sin \beta l - \sinh \beta l}$
	(1) $w(0,t) = w'(0,t) = w(l,t) = w'(l,t) = 0$ (2) $\cos \beta l \cosh \beta l = 1$ (3) $\phi(x) = A(\cos \beta x - \cosh \beta x) + (\sin \beta x - \sinh \beta x)$  $A = -\frac{\sin \beta l - \sinh \beta l}{\cos \beta l - \cosh \beta l} = \frac{\cos \beta l - \cosh \beta l}{\sin \beta l + \sinh \beta l}$
	(1) $w''(0,t) = w'''(0,t) = w''(l,t) = w'''(l,t) = 0$ (2) $\cos \beta l \cosh \beta l = 1^*$ (3) $\phi(x) = A(\cos \beta x + \cosh \beta x) + (\sin \beta x + \sinh \beta x)$  $A = -\frac{\sin \beta l - \sinh \beta l}{\cos \beta l - \cosh \beta l} = \frac{\cos \beta l - \cosh \beta l}{\sin \beta l + \sinh \beta l}$
	(1) $w(0,t) = w'(0,t) = w(l,t) = w''(l,t) = 0$ (2) $\tan \beta l = \tanh \beta l$ (3) $\phi(x) = A(\cos \beta x - \cosh \beta x) + (\sin \beta x - \sinh \beta x)$

**Figure 2.6 :** Expressions of the vibrating beams with different boundary conditions.

The natural frequency of beams is calculated by the following formula below, in agreement with Eq. (2.88) as discussed before, when n is 1.

$$\omega_n = (\beta_n L)^2 \sqrt{\frac{EI}{\rho A L^4}} \quad (2.100)$$

$\beta_n L$  values must be achieved in order to calculate the natural frequencies of systems. The necessary  $\beta_n L$  values for beams with different boundary conditions are obtained through the equation number 2's in Fig. 2.6, and they are listed in Table 2.2.

**Table 2.2 :** Values of  $\beta_n L$  for boundary conditions.

<b>End Conditions</b>	$\beta_1 L$	$\beta_2 L$	$\beta_3 L$	$\beta_4 L$
Both end fixed	4,73004	7,8532	10,9956	14,1372
Both end free	4,73004	7,8532	10,9956	14,1372
Left end fixed, right end simple support	3,9266	7,0686	10,2102	13,5518
Left end simple support, right end free	3,9266	7,0686	10,2102	13,5518
Both end simple supports	3,1416	6,2832	9,4248	12,5664
Left end fixed, right end free	1,8751	4,6941	7,8548	10,9955

The natural frequencies of beams can be calculated using  $\beta_n L$  values given in Table 2.2, and density, cross-sectional area, Young's modulus and the moment of inertia of the beams in Eq. (2.100).

## 2.4 Summary

In this chapter, Bending Equation of Euler Bernoulli, Rayleigh and Timoshenko Beam Theories are discussed first. Then, vibration equations are described for single and multi-degrees of freedom systems, and derivation of analytical formulations required for the calculation of natural frequencies and bending vibrations in beams are shown.  $\beta_n L$  values used in the analytical expression of natural frequencies are listed for various beam boundary conditions.

### **3. FLUID STRUCTURE INTERACTION IN MICRO/NANO-SCALE CANTILEVER BEAMS FOR MRA VIA FINITE ELEMENT ANALYSIS**

#### **3.1 Introduction**

Definitions required for numerical study of vibrational motion and energy transfer between micro/nano-scale doubly-clamped beams via MRA are presented in this section of the thesis. Finite Element Analysis and standard element types widely used in ANSYS FEA Software are briefly introduced first. Then, meticulous description of Acoustic Fluid-Structure Coupling in FEA is provided. Interaction processes in ANSYS are carried out in the *Harmonic Analysis Module*. Therefore, certain element types identified in ANSYS database for fluid-structure interaction in air depicting the acoustic feature are discussed. Finally, Perfectly Matched Layers, PML (Absorbing Layer) used to prevent return of vibration waves from outer-most surface of the model such that they behave as infinite air medium is presented.

#### **3.2 Finite Element Method**

Richard Courant used first the Finite Element Method (FEM) by separating system into triangular pieces in 1943. Over the years, and with the invention and advancement of computers, FEM has developed into a key and indispensable technology in the modelling and simulation of advanced engineering systems in various fields like housing, transportation, communications, and so on. In building such advanced engineering systems, engineers and designers go through a sophisticated process of modelling, simulation, visualization, analysis, design, prototyping, testing, and lastly, fabrication. It is important to note that much work is involved before the fabrication of the final product or system. This is to ensure the workability of the finished product, as well as cost effectiveness [45].

FEM examines structures as compositions of a large number of small finite elements instead of use of large-scale solid objects where traditional methods require continuous mathematical equations. Therefore, FEM as a discrete approach also finds applications in such areas as structural analysis, fluid mechanics, vibration analysis, and so on.

There are many benefits of FEM such as [46];

- Easy examination of complex shape geometries,
- Suitability for various material characteristics,
- Functionality in continuous, discontinuous and variable loads,
- Simple definition of the boundary conditions in equations.

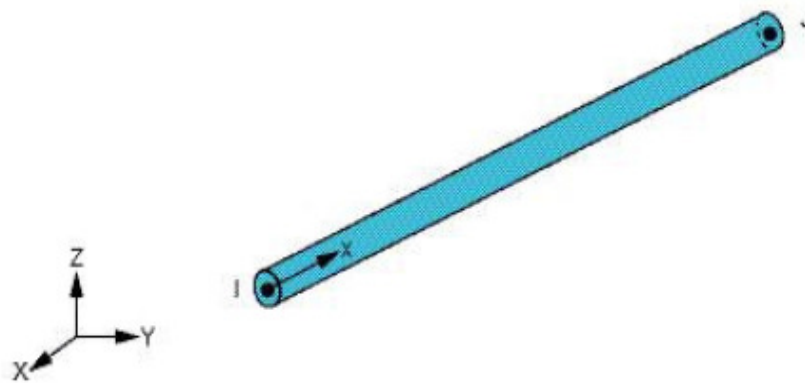
Despite these benefits, there are some restrictions of FEM;

- In general, large computational loads are of concern both in primary memory and processing time needs,
- Reliable results cannot be achieved, unless proper decomposition of continuous media, or accurate definition of material parameters and all other input parameters are not realized.

### **3.3 Common Element Types used in FEM**

#### **3.3.1 Three-Dimensional (3D) Beam Element**

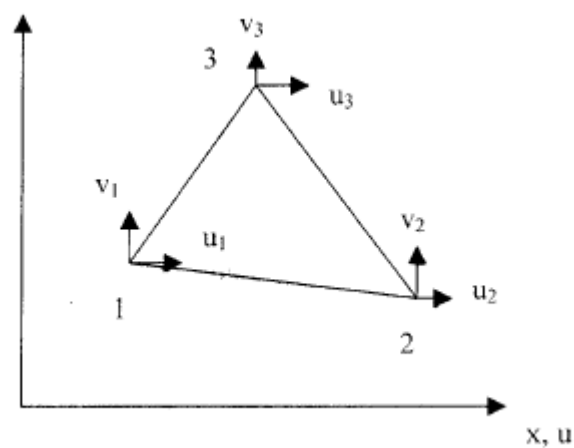
3D Beam Element, as illustrated in Fig. 3.1, is a general-purpose 1D-like finite element type utilized in three-dimensional analysis, which is represented by two nodes in the space. Hence, it is also referred to as the Space Beam Element. On the other hand, the third node, coordinate system of the element, does not have a degree of freedom. Including both the translational and rotational axes systems at the two nodes, 12 degrees of freedom exist. Element has the capacity to resist against forces from any direction or moment of rotation about any axis. Node coordinates, modulus of elasticity, shear modulus, cross-sectional area, moment of inertia, torsional constant and deformation factors perpendicular to the axis of the beam direction are needed to describe the elements [46].



**Figure 3.1 :** Three-dimensional Beam Element.

### 3.3.2 Constant Stress Triangular Element

As shown in Fig. 3.2, Constant Stress Triangular Element is defined as having a constant thickness, and a total of six degrees of freedom, connecting the three-point nodes. Its displacement field is linear along the edges and within the element. As the name refers already, the stress values are constant within its boundaries. Forces in the element are reduced as acting on the node points alone. Constant Stress Triangular Element type is most suitable when investigating small areas with stress gradient in finite element models.



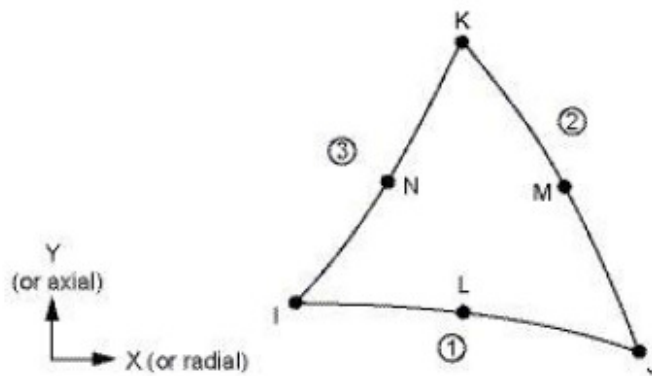
**Figure 3.2 :** Constant Stress Triangular Element.

Element displacement field is described as follows;

$$\begin{aligned} u &= a_1 + a_2x + a_3y \\ v &= a_4 + a_5x + a_6y \end{aligned} \quad (3.1)$$

### 3.3.3 Linear Stress Triangular Element

Unlike Constant Stress Triangular Element, as depicted in Fig. 3.3, Linear Stress Triangular Element has an additional node to the midpoints of the edges as well as the points of vertices. Thus, each Linear Stress Triangle Element has a total of six node points and 12 nodal degrees of freedom. Stress intensity varies linearly with the x and y coordinates in Linear Stress Triangular Element. This particular element type is very well suited to the analysis of the deflection and stress fields in models when structures exposed to bending.



**Figure 3.3 :** Linear Stress Triangular Element.

Element displacement field is described as follows;

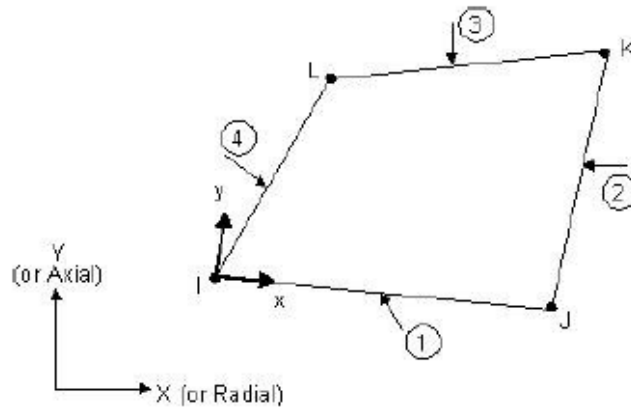
$$\begin{aligned} u &= a_1 + a_2x + a_3y + a_4x^2 + a_5xy + a_6y^2 \\ v &= a_7 + a_8x + a_9y + a_{10}x^2 + a_{11}xy + a_{12}y^2 \end{aligned} \quad (3.2)$$

### 3.3.4 Double Linear Rectangular Element

As shown in Fig. 3.4, another element type towards analysis of two-dimensional problems is Double Linear Quadrilateral Element. There are four nodes in the vertices of the element corresponding to a total of eight nodal degrees of freedom. The element has also four nodes in the midpoints of the edges.



The element is named as being double linear due to the multiplication two linear polynomials with  $u$  and  $v$  displacement equations.



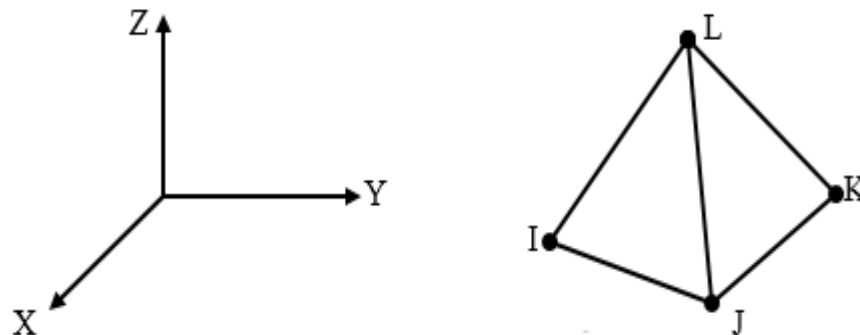
**Figure 3.4 :** Double Linear Quadrilateral Element.

The displacement field for the four- node element is described as follows;

$$\begin{aligned} u &= a_1 + a_2x + a_3y + a_4xy \\ v &= a_5 + a_6x + a_7y + a_8xy \end{aligned} \quad (3.3)$$

### 3.3.5 Four-node Tetrahedral Element

The Four-node Tetrahedral Element is the simplest three-dimensional element used in the analysis of solid mechanics applications. This element has four nodes each with only translational degrees of freedom in the nodal  $X$ ,  $Y$ , and  $Z$  directions. A typical Four-node Tetrahedral Element is as shown in Fig. 3.5.



**Figure 3.5 :** Four-node Tetrahedral Element.

The displacement fields for the Four-node Tetrahedral Element are provided in the following equations [47];

$$\begin{aligned} u &= C_{11} + C_{12}X + C_{13}Y + C_{14}Z \\ v &= C_{21} + C_{22}X + C_{23}Y + C_{24}Z \\ w &= C_{31} + C_{32}X + C_{33}Y + C_{34}Z \end{aligned} \quad (3.4)$$

Solving for the unknown  $C$ -coefficients, substituting the result back into Eq. (3.4), and regrouping the parameters, we obtain;

$$\begin{aligned} u &= S_1u_I + S_2u_J + S_3u_K + S_4u_L \\ v &= S_1v_I + S_2v_J + S_3v_K + S_4v_L \\ w &= S_1w_I + S_2w_J + S_3w_K + S_4w_L \end{aligned} \quad (3.5)$$

The shape functions are;

$$\begin{aligned} S_1 &= \frac{1}{6V} (a_I + b_I X + c_I Y + d_I Z) \\ S_2 &= \frac{1}{6V} (a_J + b_J X + c_J Y + d_J Z) \\ S_3 &= \frac{1}{6V} (a_K + b_K X + c_K Y + d_K Z) \\ S_4 &= \frac{1}{6V} (a_L + b_L X + c_L Y + d_L Z) \end{aligned} \quad (3.6)$$

where  $V$ , the volume of the tetrahedral element, is computed as;

$$6V = \det \begin{bmatrix} 1 & X_I & Y_I & Z_I \\ 1 & X_J & Y_J & Z_J \\ 1 & X_K & Y_K & Z_K \\ 1 & X_L & Y_L & Z_L \end{bmatrix} \quad (3.7)$$

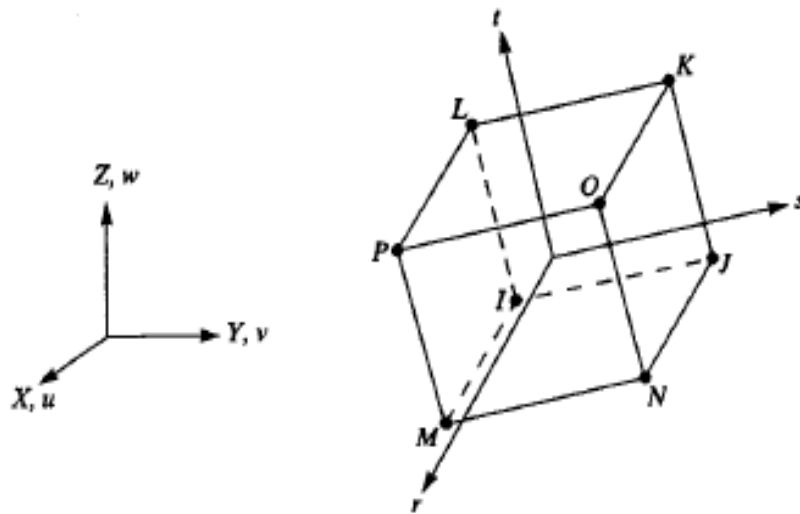
The  $a_I, b_I, c_I, d_I, \dots$  and  $d_L$ -terms are;

$$\begin{aligned}
 a_I &= \det \begin{bmatrix} X_J & Y_J & Z_J \\ X_K & Y_K & Z_K \\ X_L & Y_L & Z_L \end{bmatrix} & b_I &= -\det \begin{bmatrix} 1 & Y_J & Z_J \\ 1 & Y_K & Z_K \\ 1 & Y_L & Z_L \end{bmatrix} \\
 c_I &= \det \begin{bmatrix} X_J & 1 & Z_J \\ X_K & 1 & Z_K \\ X_L & 1 & Z_L \end{bmatrix} & a_I &= \det \begin{bmatrix} X_J & Y_J & 1 \\ X_K & Y_K & 1 \\ X_L & Y_L & 1 \end{bmatrix}
 \end{aligned} \tag{3.8}$$

$a_I, b_I, c_I, d_I, \dots$  and  $d_L$ -terms via similar determinants by rotating through the  $I, J, K$ , and  $L$  subscripts using the right-hand rule.

### 3.3.6 Eight-node Brick Element

The Eight-node Brick Element is three-dimensional used in the analysis of solid mechanics applications. There are eight nodes in the element each of which has only translational degrees of freedom in the nodal  $X, Y$ , and  $Z$  directions. Eight-node Brick Element is shown in Fig. 3.6.



**Figure 3.6 :** Eight-node Brick Element.

The element's displacement field in terms of the nodal displacements and the shape functions can be written as;

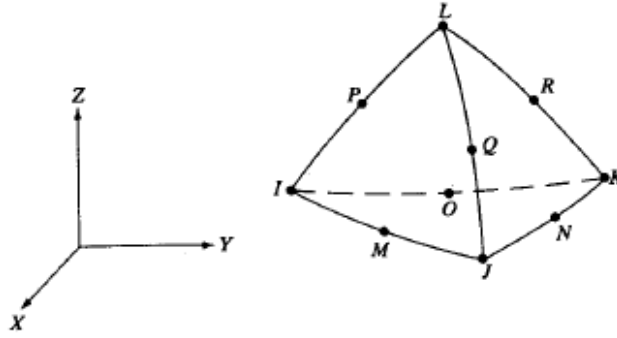
$$\begin{aligned}
u &= \frac{1}{8} (u_I (1-s)(1-t)(1-r) + u_J (1+s)(1-t)(1-r)) & (3.9) \\
&+ \frac{1}{8} (u_K (1+s)(1+t)(1-r) + u_L (1-s)(1+t)(1-r)) \\
&+ \frac{1}{8} (u_M (1-s)(1-t)(1+r) + u_N (1+s)(1-t)(1+r)) \\
&+ \frac{1}{8} (u_O (1+s)(1+t)(1+r) + u_P (1-s)(1+t)(1+r))
\end{aligned}$$

$$\begin{aligned}
v &= \frac{1}{8} (v_I (1-s)(1-t)(1-r) + v_J (1+s)(1-t)(1-r)) & (3.10) \\
&+ \frac{1}{8} (v_K (1+s)(1+t)(1-r) + v_L (1-s)(1+t)(1-r)) \\
&+ \frac{1}{8} (v_M (1-s)(1-t)(1+r) + v_N (1+s)(1-t)(1+r)) \\
&+ \frac{1}{8} (v_O (1+s)(1+t)(1+r) + v_P (1-s)(1+t)(1+r))
\end{aligned}$$

$$\begin{aligned}
w &= \frac{1}{8} (w_I (1-s)(1-t)(1-r) + w_J (1+s)(1-t)(1-r)) & (3.11) \\
&+ \frac{1}{8} (w_K (1+s)(1+t)(1-r) + w_L (1-s)(1+t)(1-r)) \\
&+ \frac{1}{8} (w_M (1-s)(1-t)(1+r) + w_N (1+s)(1-t)(1+r)) \\
&+ \frac{1}{8} (w_O (1+s)(1+t)(1+r) + w_P (1-s)(1+t)(1+r))
\end{aligned}$$

### 3.3.7 Ten-Node Tetrahedral Element

The Ten-node Tetrahedral Element, as shown in Fig. 3.7, is a higher order version of the three-dimensional linear Four-node Tetrahedral Element, providing more accurate results in applications with curved boundaries.



**Figure 3.7 : Ten-node Tetrahedral Element.**

For applications of solids, the displacement field is represented by;

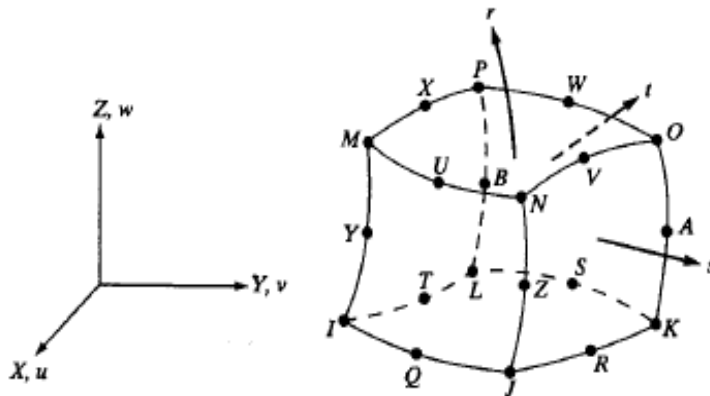
$$u = u_I(2S_1 - 1)S_1 + u_J(2S_2 - 1)S_2 + u_K(2S_3 - 1)S_3 + u_L(2S_4 - 1)S_4 + 4(u_M S_1 S_2 + u_N S_2 S_3 + u_O S_1 S_3 + u_P S_1 S_4 + u_Q S_2 S_4 + u_R S_3 S_4) \quad (3.12)$$

$$v = v_I(2S_1 - 1)S_1 + v_J(2S_2 - 1)S_2 + v_K(2S_3 - 1)S_3 + v_L(2S_4 - 1)S_4 + 4(v_M S_1 S_2 + v_N S_2 S_3 + v_O S_1 S_3 + v_P S_1 S_4 + v_Q S_2 S_4 + v_R S_3 S_4) \quad (3.13)$$

$$w = w_I(2S_1 - 1)S_1 + w_J(2S_2 - 1)S_2 + w_K(2S_3 - 1)S_3 + w_L(2S_4 - 1)S_4 + 4(w_M S_1 S_2 + w_N S_2 S_3 + w_O S_1 S_3 + w_P S_1 S_4 + w_Q S_2 S_4 + w_R S_3 S_4) \quad (3.14)$$

### 3.3.8 Twenty-Node Brick Element

The Twenty-node Brick Element, as depicted in Fig. 3.8, is a higher order version of the three-dimensional Eight-node Brick Element, which is more capable and accurate in models with curved boundaries.



**Figure 3.8 : Twenty-node Brick Element.**

$$\begin{aligned}
u = & \frac{1}{8}(u_I(1-s)(1-t)(1-r)(-s-t-r-2) + u_J(1+s)(1-t)(1-r)(s-t-r-2)) \\
& + \frac{1}{8}(u_K(1+s)(1+t)(1-r)(s+t-r-2) + u_L(1-s)(1+t)(1-r)(-s+t-r-2)) \\
& + \frac{1}{8}(u_M(1-s)(1-t)(1+r)(-s-t+r-2) + u_N(1+s)(1-t)(1+r)(s-t+r-2)) \\
& + \frac{1}{8}(u_O(1+s)(1+t)(1+r)(s+t+r-2) + u_P(1-s)(1+t)(1+r)(-s-t+r+2)) \\
& + \frac{1}{4}(u_Q(1-s^2)(1-t)(1-r) + u_R(1+s)(1-t^2)(1-r)) \quad (3.15) \\
& + \frac{1}{4}(u_S(1-s^2)(1+t)(1-r) + u_T(1-s)(1-t^2)(1-r)) \\
& + \frac{1}{4}(u_U(1-s^2)(1-t)(1+r) + u_V(1+s)(1-t^2)(1+r)) \\
& + \frac{1}{4}(u_W(1-s^2)(1+t)(1+r) + u_X(1-s)(1-t^2)(1+r)) \\
& + \frac{1}{4}(u_Y(1-s)(1-t)(1-r^2) + u_Z(1+s)(1-t)(1-r^2)) \\
& + \frac{1}{4}(u_A(1+s)(1+t)(1-r^2) + u_B(1-s)(1+t)(1-r^2))
\end{aligned}$$

The  $v$  and  $w$ -components of the displacement are similar to the  $u$ -component;

$$\begin{aligned}
v = & \frac{1}{8}(v_I(1-s)(1-t)(1-r)(-s-t-r-2) + v_J(1+s)(1-t)(1-r)(s-t-r-2)) \\
& + \frac{1}{8}(u_K(1+s)(1+t)(1-r)(s+t-r-2) + \dots) \quad (3.13)
\end{aligned}$$

$$\begin{aligned}
w = & \frac{1}{8}(w_I(1-s)(1-t)(1-r)(-s-t-r-2) + w_J(1+s)(1-t)(1-r)(s-t-r-2)) \\
& + \frac{1}{8}(w_K(1+s)(1+t)(1-r)(s+t-r-2) + \dots) \quad (3.14)
\end{aligned}$$

### 3.4 Acoustic Fluid-Structure Coupling in FEM

For the coupled fluid-structure interaction problem, when the fluid pressure at the interface is added to the structure's equation of motion, the following expression is obtained.

$$\begin{bmatrix} M & 0 \\ 0 & 0 \end{bmatrix} \begin{Bmatrix} \ddot{u} \\ \ddot{v} \end{Bmatrix} + \begin{bmatrix} C & 0 \\ 0 & 0 \end{bmatrix} \begin{Bmatrix} \dot{u} \\ \dot{v} \end{Bmatrix} + \begin{bmatrix} K & K^Z \\ K^{Z^r} & K^d \end{bmatrix} \begin{Bmatrix} u \\ v \end{Bmatrix} = \begin{Bmatrix} F + F^{pr} \\ L \end{Bmatrix} \quad (3.15)$$

where  $M$  is structural mass matrix,  $C$  is structural damping matrix,  $K$  is structural stiffness matrix,  $K^d$  is dielectric conductivity matrix,  $K^Z$  is piezoelectric coupling matrix,  $F$  is structural load vector (vector of nodal forces, surface forces and body forces),  $L$  is electric load vector (applied nodal charge vector),  $F^{pr}$  is fluid pressure load vector.

The fluid pressure load vector at the interface,  $S$ , is obtained by integrating the pressure over the surface of the fluid/structure interface.

$$F^{pr} = \iint \{N'\} P \{n\} dS \quad (3.16)$$

where members of  $\{N'\}$  are the shape functions employed to discretize the displacement components obtained from the structural element,  $u, v, w, \{n\}$  is the unit normal to the fluid/structure boundary.

Theoretical model underlying all mathematical representations of the acoustic propagation is the wave equation. The wave equation is derived from the more fundamental equation of state, continuity and motion. The assumptions made in acoustics and fluid-structure analyses are that the fluid behaves as an ideal acoustic medium. This implies that; (i) the fluid is isotropic and homogeneous, (ii) thermodynamic processes are adiabatic, (iii) the fluid is inviscid (no viscous damping), and (iv) acoustic pressure and displacement amplitudes are small relative to the fluid's ambient state.

The acoustic wave equation is given by;

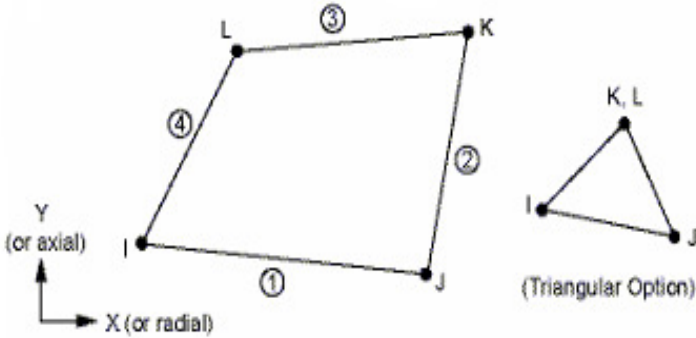
$$\nabla^2 p = \frac{1}{c^2} \frac{\partial^2 p}{\partial t^2} \quad (3.17)$$

where  $c$  is the acoustic wave speed, expressed in  $c^2 = K/\rho$ ,  $\rho$  is the density of fluid, and  $K$  is the fluid bulk modulus.

Motion and energy transfer between the beams utilizing MRA is an acousto-mechanical multiphysics problem modeled as Fluid-Structure Interaction problem. In this thesis, mechanical energy transfer between the beams via MRA is simulated in a commercial FEM analysis software, namely ANSYS (ANSYS Inc., USA). Acoustic and Fluid-Structure Interaction processes in ANSYS are carried out in the harmonic analysis module. Certain element types identified in ANSYS database for fluid-structure interaction in the air show the acoustic feature. These element types are referred to FLUID29, FLUID30, FLUID129, FLUID130, FLUID220 and FLUID221. FLUID29 and FLUID129 are used to represent two-dimensional (2D) structures, while FLUID30, FLUID130, FLUID220 and FLUID221 are used towards three-dimensional (3D) ones. Below are detailed information about the acoustic element types [49];

**FLUID29** is used to model both the fluid medium and the interface in fluid/structure interaction applications. Typical uses include sound wave propagation and submerged structure dynamics. The governing equation for acoustics, namely the 2D wave representation, has been discretized taking into account the coupling of acoustic pressure and structural motion at the interface.

The element has four corner nodes each with three degrees of freedom, namely pressure and translations in the nodal x and y directions. The translations, however, are applicable only at the nodes on the interface. Acceleration effects, such as in sloshing problems, may be included into the nodes. The element has the capability to include damping effects of sound absorbing material at the interface. It can be employed with other 2D structural elements to perform asymmetric or damped modal, full harmonic and full transient method analyses.

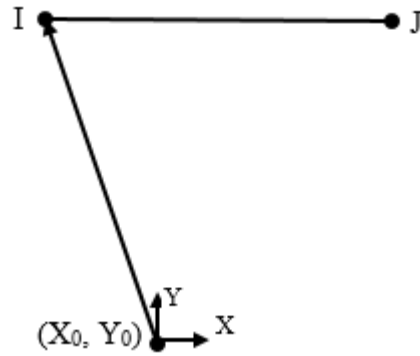


**Figure 3.9 : FLUID29 geometry.**



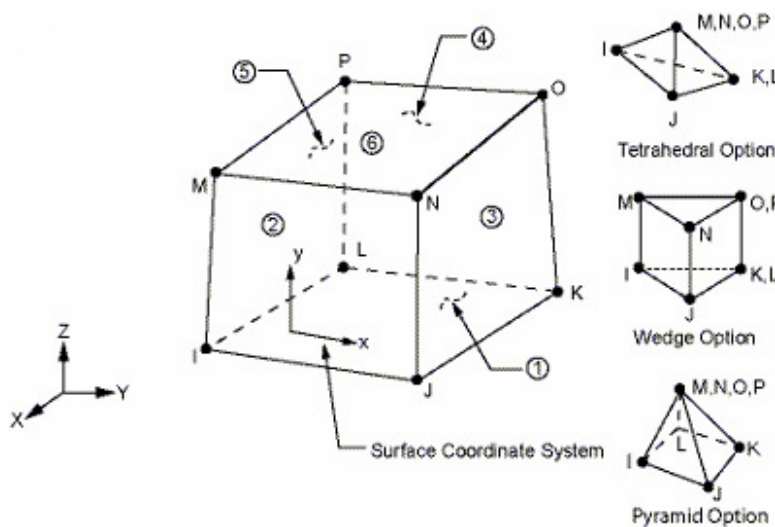
The geometry, node locations, and the coordinate system for this element are as shown in Fig. 3.9. The element is defined by such four nodes under the MODE command as the number of harmonic waves (MODE), the symmetry condition (ISYM), a reference pressure (PREF), and the isotropic material properties (MU). The reference pressure is deployed to calculate sound pressure level of the element for which the default is  $20 \times 10^{-6} \text{ N/m}^2$ . The speed of sound in the fluid (SONC),  $\sqrt{k/\rho_0}$ , is accessed, where  $k$  is the bulk modulus of the fluid, and  $\rho_0$  is the mean fluid density (DENS). The dissipative effect due to viscosity of fluid is neglected, but absorption of sound at the interface is accounted for by generating a damping matrix using the surface area and boundary admittance at the interface. Experimental values of the boundary admittance for the sound absorbing material may be input as material property. MU values are recommended to be in the range from 0.0 to 1.0. However, values greater than 1.0 are also allowed. While MU being 0.0 indicates no sound absorption, MU being 1.0 indicates full sound absorption. DENS, SONC and MU values are evaluated at the average temperatures of the nodes.

**FLUID129**, as illustrated in Fig. 3.10, has been developed as a companion element to FLUID29. It is intended to be used as an envelope to a model made of FLUID29 finite elements. It simulates the absorbing effects of a fluid domain that extends to infinity beyond the boundary of FLUID29 finite element domain. FLUID129 realizes a second-order absorbing boundary condition so that an outgoing pressure wave reaching the boundary of the model is "absorbed" with minimal reflections back into the fluid domain. The element can be used to model the boundary of 2D (planar or axisymmetric) fluid regions and as such, it is a line element; it has two nodes with one pressure degree of freedom per node. FLUID129 may be used in transient, harmonic, and modal analyses. Typical applications include structural acoustics, noise control, underwater acoustics, and others.



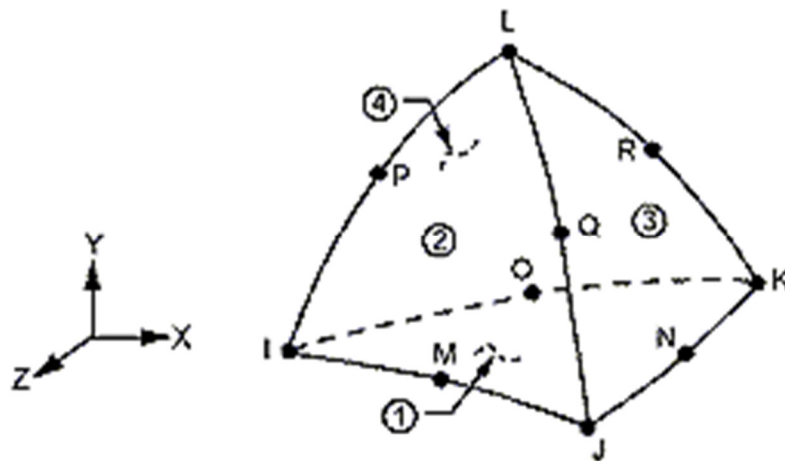
**Figure 3.10 :** FLUID129 geometry.

**FLUID30** element is used to model both the fluid medium and the interface in fluid/structure interactions. Typical applications include sound wave propagation and submerged structure dynamics. The governing equation for acoustics, namely the 3D wave representation, has been discretized taking into account the coupling of acoustic pressure and structural motion at the interface. The element has eight corner nodes each with such four degrees of freedom as pressure and translations in the nodal x, y and z directions as depicted in Fig. 3.11. The translations, however, are applicable only at the nodes on the interface. Acceleration effects, such as in sloshing problems, may also be included in the element. The element has the capability to include damping effects of sound absorbing material at the interface as well as that within the fluid. It can be used with other 3D structural elements to perform asymmetric or damped modal, full harmonic and full transient method analyses.



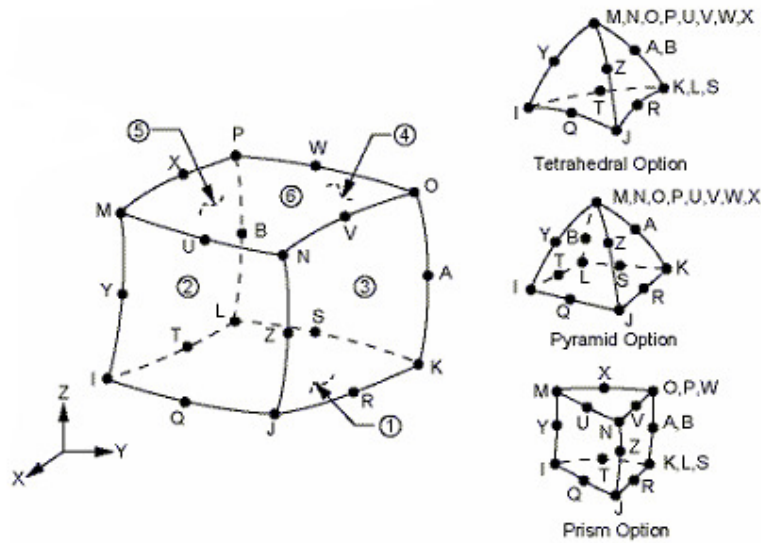
**Figure 3.11 :** FLUID30 geometry.

**FLUID221** is a higher order 3D 10-node solid element that exhibits quadratic pressure behavior, and is used to model both the fluid medium and the interface in fluid-structure interactions. Typical uses include sound wave propagation and submerged structure dynamics. The governing equation for acoustics, namely the 3D wave representation, has been discretized, taking into account the coupling of acoustic pressure and structural motion at the interface. The element has four degrees of freedom per node: pressure and translations in the nodal x, y and z direction as shown in Fig. 3.12. The translations are applicable only at the nodes on the interface. It has the capability to include damping effects of sound absorbing material at the interface as well as that within the fluid. It can be used with other 3D structural elements to perform asymmetric or damped modal, full harmonic and full transient method analyses. When there is no structural motion, the element is also applicable to modal analyses.



**Figure 3.12 :** FLUID221 geometry.

**FLUID220** is similar to element FLUID221 in its use and properties except that it has 20-nodes. The geometry, node locations, and the coordinate system are as shown in Figure 3.13. The element is defined by 20 nodes, a reference pressure, and the isotropic material properties. The reference pressure is utilized to calculate sound pressure level for which default value is  $20 \times 10^{-6} \text{ N/m}^2$ . The speed of sound in the fluid needs to be accessed as an input parameter.



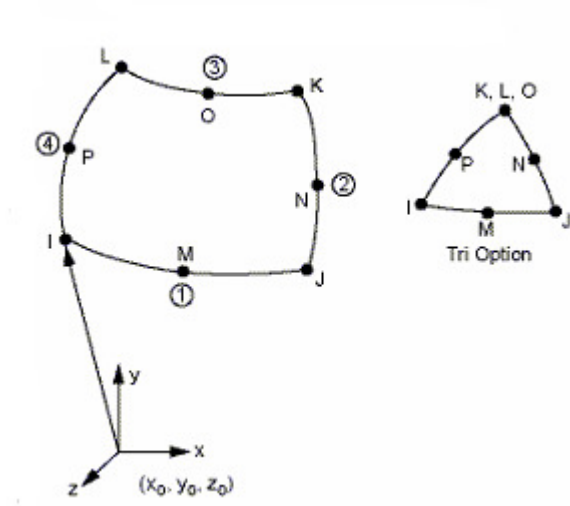
**Figure 3.13 :** FLUID220 geometry.

Node and element loads are accessible. Fluid-structure interfaces (FSI) may be flagged by surface loads at the element faces as shown by the circled numbers in Figure 3.13. Specifying the FSI label without a value (SF, SFA and SFE) will couple the structural motion and fluid pressure at the interface.

When FLUID30, FLUID220, and FLUID221 are employed in acoustic analysis, existence of Fluid-Structure Interaction between selected elements is defined by the particular value of KEYOPT(2). In the case of absence of a structure at the interface and coupling between the fluid and structure, a value of 1 is assigned to KEYOPT(2). Since the absence of coupling produces symmetric element matrices, a symmetric eigensolver may be used within the modal analysis. KEYOPT(2) having a value of 0, the default, specifies a coupled (asymmetric) situation requiring a corresponding unsymmetric eigensolver. In the presence of FSI coupling, KEYOPT(2) is set to 2 or 3, where a symmetric eigensolver may also be used for modal analysis and a symmetric linear equation solver may be used for full harmonic analysis.

**FLUID130** has been developed as a companion element to FLUID30, FLUID220, and FLUID221. It is intended to be used as an envelope to a model made of FLUID30, FLUID220, and FLUID221 finite elements. It simulates the absorbing effects of a fluid domain extending to infinity beyond the boundary of the finite element domain made of FLUID30, FLUID220, and FLUID221. FLUID130 realizes a second-order absorbing boundary condition so that an outgoing pressure wave reaching the

boundary of the model is "absorbed" with minimal reflections back into the fluid domain. The element can be used to model the boundary of 3D fluid regions and as such, it is a plane surface element composed of four nodes each with one-pressure degrees of freedom. FLUID130 may be used in transient, harmonic, and modal analyses. Typical applications include structural acoustics, noise control, underwater acoustics, and others.

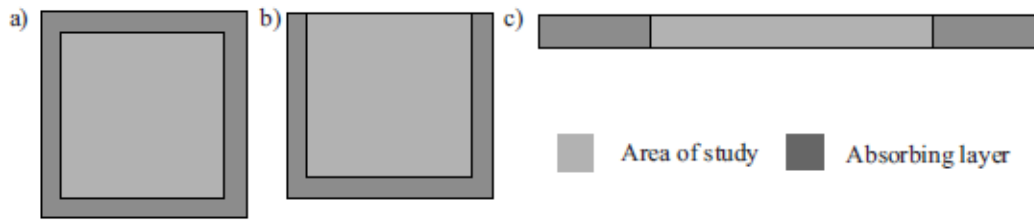


**Figure 3.14 :** FLUID130 geometry.

The geometry, node locations, and the coordinate system for this element are shown in Figure 3.14. The element is defined by four nodes as  $I, J, K, L$ , or eight nodes as  $I, J, K, L, M, N, O, P$ , the material property, speed of sound, and the real constants. A triangular element may be formed by defining duplicate  $K$  and  $L$  node numbers. The element must be at the spherical boundary of an acoustic fluid domain meshed via FLUID30, FLUID220, and FLUID221 elements, with a radius of  $RAD$  centered at or near the core of the structure. The radius should be described through the real constants.

### 3.4.1 Perfectly Matched Layers, PML (Absorbing Layer)

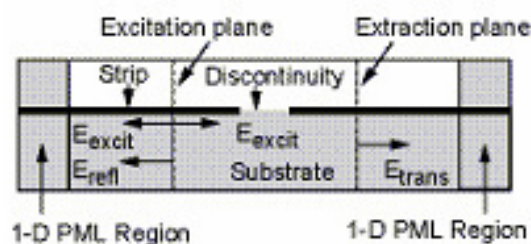
Absorbing layers are finite regions attached at the extremities of a model as seen in Fig. 3.15. They are targeted to approximate an unbounded problem case with absorbing waves directed inwards. Small reflections from the absorbing region exist, but they can be made negligible by correct definition of the layer parameters [50].



**Figure 3.15 :** Concept of absorbing layer in 2D models: a) infinite medium, b) semi-infinite medium, c) plate.

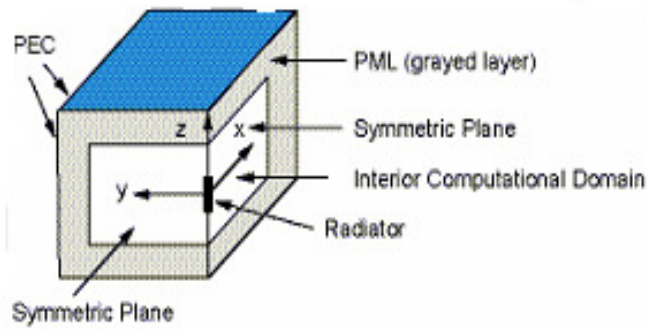
Use of PML was created in 1994 by Berenger for electromagnetism, and has been extended to such other fields as acoustics, and seismological and other elastic waves [50]. As its name indicates, a PML matches perfectly the impedance of the area of study meaning that, in theory, a wave enters a PML without reflection. Inside the PML, wave decays exponentially with location. A PML can, therefore, be used to achieve total radiation of a wave at the outer boundary of the simulation volume.

The purpose of an absorbing boundary condition is to eliminate reflections of the outgoing electromagnetic wave back into the FEA computational domain. PML layers are absorbing electromagnetic wave elements designed for the mesh truncation of an open FEA domain in a harmonic or modal analysis. It is at the same time an artificial anisotropic material transparent and heavily lossy to incoming electromagnetic waves. PML can reduce the size of the computational domain significantly with very small numerical reflections. A PML region is backed by a PEC boundary condition. If the electromagnetic wave needs to be absorbed in only one direction, as in the case of a traditional waveguide port, a 1D PML region in the global Cartesian coordinate system or a local Cartesian coordinate system as shown in the following figure of Fig. 3.16 must be constructed.



**Figure 3.16 :** Microstrip structure with PML regions [49].

A 3D PML region consists of element layers extending from the interior volume towards the open domain as shown in Fig. 3.17. A block about the origin of the global Cartesian coordinate system or a local Cartesian coordinate system is constructed. The edges of the 3D PML region with the axes of the Cartesian coordinate system is aligned.



**Figure 3.17 :** PML region attached to interior region [49].

PML must be created at the outside of the air layer in order for the acoustic waves spread without any back-reflection from the air boundary. The aforementioned acoustic element types of FLUID30, FLUID220 and FLUID221 are assigned to this specific layer in the FEA software. KEYOPT(4) is used to describe PML feature. Pressure on the exterior enclosure of PML must be constrained to zero, unless it is on the symmetric planes.

### 3.5 Summary

In this chapter, Finite Element Analysis (FEA) is introduced and common element types used in FEA are mentioned shortly. Acoustic Fluid-Structure Coupling and the expression of acoustic waves in FEA are presented towards investigation of numerical mechanical energy transfer interaction between doubly-clamped beams via MRA. Then, acoustic element types are defined such that air will resemble acoustic properties in the commercial FEM analysis software at hand. Later, necessary environment characteristics for the element types are also summarized. Finally, the absorbing layer (Perfectly Matched Layers, PML) behaving as an infinite medium of modeled air environment in order to prevent back-reflection by absorption of acoustic waves created by the target beam are described.





## **4. CONCEPT AND MODEL OF THE ENERGY TRANSFER VIA MRA BETWEEN THE BEAMS**

### **4.1 Introduction**

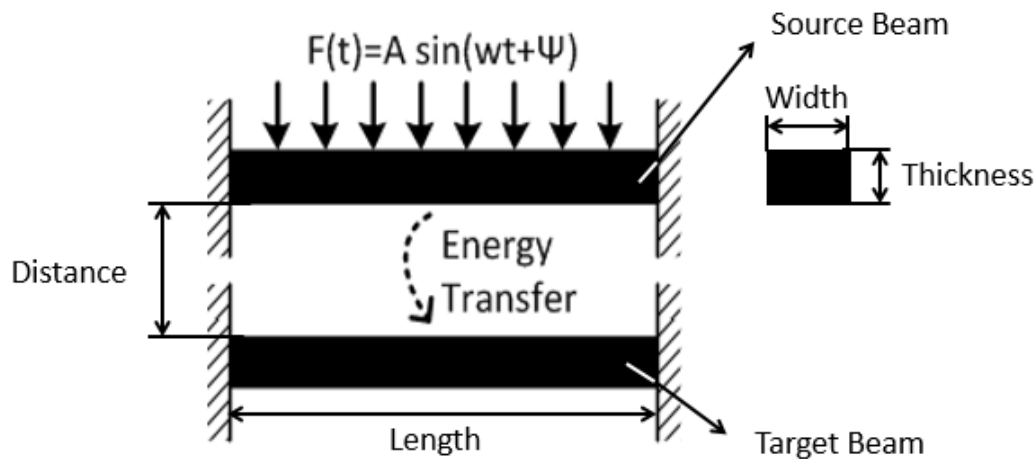
In this section of the thesis, energy transfer with the help of MRA based on the widely known absorbance example between two identical tuning forks in the literature is discussed first. Energy interaction via MRA is inefficient in conventional tuning forks due to their large size and distances in between. Novelty of this thesis is to improve the insufficient performance of MRA taking place on macro-scaled structures by deploying micro/nano-scale structured beams. Main purpose of the energy transfer concept between micro/nano-scale doubly-clamped beams is explained. Then, modeling energy transfer between such beams is described in *Harmonic Analysis Module*. Herein, respective definition of material properties, geometry creation of beams and air medium, identification of element types, separate mesh processes, application of the boundary conditions and force values and identification of FSI interaction with the help of APDL codes are stated in detail.

### **4.2 Concept of Energy Transfer**

In this study, energy interaction via *MRA* between two identical micro/nano cantilever beams positioned at certain distances relative to each other are examined. In addition, creating fields of application in micro / nano-scale structures, such as remote drive and selective resonance are targeted by achieving the regular relationship between energy transfer values and distance changes.

Concept investigated in this study is as given in Fig. 4.1. Herein, the first and second beams are called as source and target beams, respectively. The source beam gets mechanically excited by sinusoidal dynamic load exerted on its top surface in a distributed manner. Vibrations on the source beam bring about pressure change in air molecules causing propagate acoustic waves towards the target beam. The target beam in return absorbs those at the resonant frequency and start to vibrate, as a consequence,

the energy interaction is realized. The interaction of beams is scaled in the squared-deflections ratio. Then, those rates are analyzed for various distances and geometries. Use of micro/nano-scale beams not only increases the efficiency of energy transfer, but also it eases fabrication, testing and characterization, particularly at oscillations with high-frequency vibrations. In the following section, numerical study of energy transfer between beams via MRA in FEM Software is presented.



**Figure 4.1 :** Conceptual illustration.

### 4.3 Modeling of Energy Transfer Between Beams in FEM Analysis

Motion and energy transfer between micro/nano-scale beams via MRA are analyzed with the help of both modal and harmonic analysis modules in FEM Software. Both the natural frequencies and mode shapes of beams are obtained in the modal analysis section. Energy transition from the source to target beam is examined as an acoustic-feature in the harmonic analysis module. After the natural frequency of beams are determined through modal analysis, harmonic analysis is conducted at the frequency range in the vicinity of the first natural frequency of beams.

#### 4.3.1 Material identification and geometric model

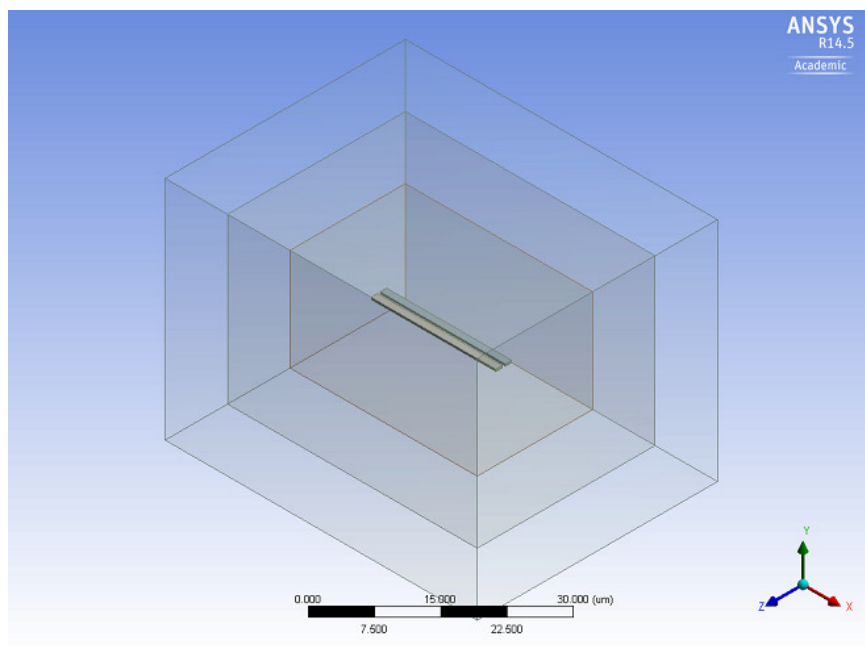
In the harmonic analysis, first, materials must be selected from the list of available materials or their properties must be specified manually in so-called *Engineering Data* section of the harmonic analysis. In this thesis, silicon is used as beam material, and air as the medium of energy transfer. Therefore, such material properties of silicon and air as density, Young's Modulus and Poisson's Ratio must be defined in the module.

Material properties of silicon and air are as given in Table 4.1. Density, Young's Modulus and Poisson Ratio for silicon are respectively 2330 kg/m<sup>3</sup>, 165 GPa and 0.27. Density, Young's Modulus and Poisson Ratio for air are respectively 1.2 kg/m<sup>3</sup>, 150 kPa and 0.49.

**Table 4.1** : Material properties of silicon and air.

	Silicon	Air
Density	2330 kg/m <sup>3</sup>	1.2 kg/m <sup>3</sup>
Young's Modulus	165 GPa	150 kPa
Poisson's Ratio	0.27	0.49
Bulk Modulus	119.57 GPa	2.5 MPa
Shear Modulus	64.961 GPa	50.336 kPa

In addition to the material properties, the beam and air layer geometries are defined in so-called *Geometry Module* of the FEM Software. As shown in Fig. 4.2, air medium is subdivided into three layers using Boolean function. Each air layer is defined as a separate region. Finally, all elements are selected and defined as a single piece with the help of so-called *Form New Part* command.



**Figure 4.2** : Geometric model of the beams and air layers.

### 4.3.2 Definition of analysis settings and results

In this section, both beam and air layer elements are assigned with the corresponding type of material defined as standard or custom in the *Engineering Data*. FLUID220 and FLUID221 element types showing the acoustic properties are assigned to air layers via access to *Commands (APDL) File*.

First, the speed of sound, air density and contact constraints are entered to the inner layer of air via the codes given in Table 4.2. While FLUID220 element type is assigned to air region in contact with beam surfaces, FLUID221, on the other hand, is utilized in remote regions. Hence, FLUID221 element type is considered suitable for the intermediate air layer. As with the inner air layer, the velocity of sound and density values are entered. Unlike the inner air layer, the *KEYOPT(2)* value for FLUID221 element type is set as "1" to indicate direct non-contact with the solid in the intermediate air layer. Codes used for the intermediate layer of air are as listed in Table 4.2. This layer simplifies the mesh process, and it provides a better quality mesh operation with smaller number of nodes and elements. Thus, computer constraints are avoided and simulation results are obtained in a shorter period.

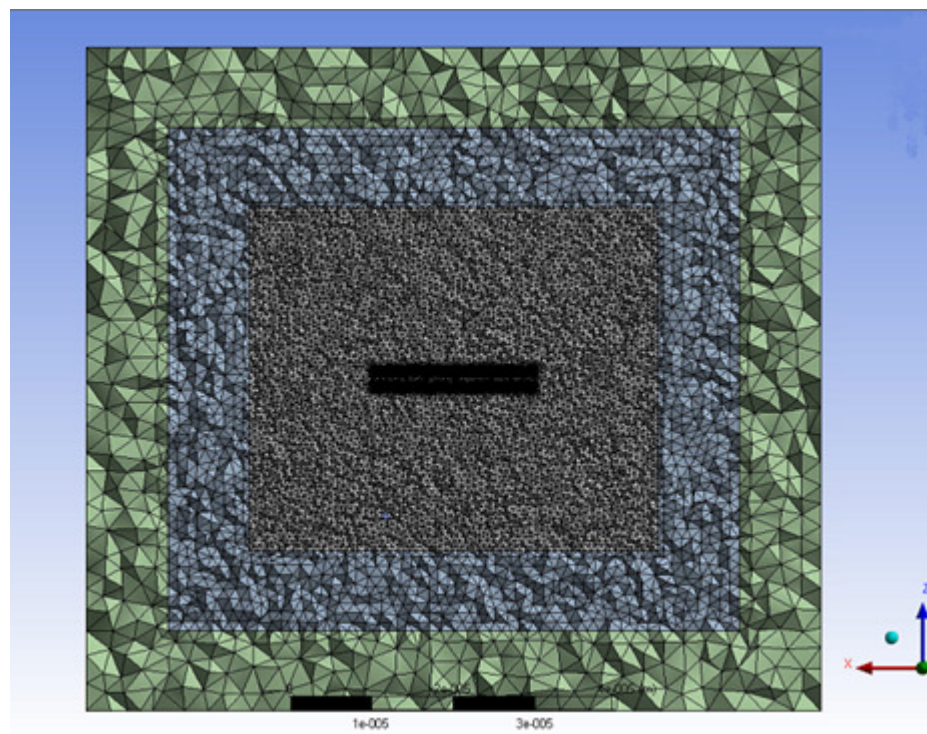
**Table 4.2 :** APDL codes for air layers.

Inner Air Layer	Intermediate Air Layer	Outer Air Layer
et,MATID,221	et,MATID,221,,1	et,MATID,221,,1,,1
et,MATID+1,220	mpdele,all,MATID	mpdele,all,MATID
mpdele,all,MATID	mp,dens,MATID,1.2	mp,dens,MATID,1.2
mpdele,all,MATID+1	mp,sonc,MATID,343	mp,sonc,MATID,343
mp,dens,MATID,1.2		
mp,sonc,MATID,343		
mpcopy,,MATID,MATID+1		

The outer layer is created to absorb acoustic waves emitted from the source and to prevent their back-reflection. The modeled air medium acts as an infinite ambient. In addition, element type used in this layer, FLUID221, is defined with *KEYOPT(4)* being "1" to demonstrate their absorption feature. Thus, acoustic element acts as

Perfect Matching Layer (PML). The velocity of sound and density values are also specified for this layer. Related codes are also noted in Table 4.2. After element types are assigned, the selected regions are created in *Named Selections* to define boundary conditions of the system and create suitable mesh for each element. In this section, the external surfaces of the air model are selected and called as PML. The surfaces of beams are individually selected and source beam is referred to as *BEAM1*, target beam is called as *BEAM2*. Finally, in order to apply force on the upper surface of the source beam, nodes on the same surface are selected, and a new *Named Selections* is created.

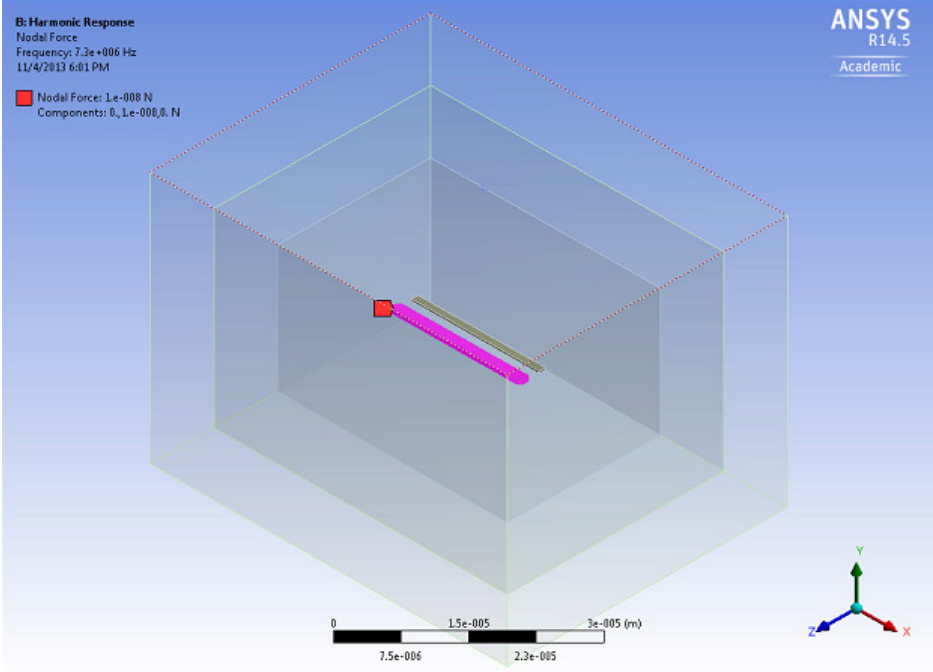
Separate mesh processes with different element sizes for each air layer and beams are deployed. Meshed model is as given in Fig. 4.3. Then, the desired frequency range and the solution step are entered into the system under *Analysis Setting*. Moreover, *Full* is selected. Then, the boundary conditions for the system are set.



**Figure 4.3 :** Meshed geometric model with beams and air layers.

Once both ends of the beams in the model are fixed as boundary conditions, the load is applied. Load can be applied in the system in one of such options as the surface force, body force, pressure or nodal force. Here, as illustrated in Fig. 4.4, the nodal force is applied to the top surface of the source beam.

The *Commands (APDL) File* is created in order to set the pressure value on boundaries to zero and to ensure interaction between the beams and air. Commands employed in this section are as provided in Table 4.3.



**Figure 4.4 :** The nodal force illustration on the geometric model.

Zero pressure is given to the outer air surface described as PML in the *Named Selections* with the first line of code in order to absorb the waves from the source beam. The interaction between the source beam and air, and the target beam and air is defined by the following codes. Furthermore, if desired, operating frequency range and the solution step can be defined in this section as well. The model gets established at this stage.

**Table 4.3 :** APDL codes for *Analysis Setting* and FSI.

```

d,PML,pres,0
esel,s,ename,,220,221
esel,a,ename,,30
sf,BEAM1,fsi
sf,BEAM2,fsi
allsel,all
outres,m'sc,all
harfrg,ARG1,ARG2
nsubst,20
  
```

To calculate the energy transfer rate, frequency-dependent deformation values should be calculated for each beam. In this process, first, *Solution* is right-clicked with the mouse. Then, *Frequency Response-Deformation* is selected from *Insert*. After the top surface of the beam is selected as geometry in *Detail* window of *Frequency Response*, the direction of desired deformation is chosen under *Orientation*. This operation is carried out separately for both beam surfaces. If required, deformation values can be extracted at a single frequency by right-clicking *Solution* and choosing *Total Deformation* under *Insert*. Besides, for single frequency deformations, the beam needs to be defined as *Geometry*, and deformation distribution of the beams is calculated at the desired frequency.

#### **4.4 Summary**

In this chapter, initially, such concepts as representation of the cross-section of beam geometries used in the investigation of motion and energy transfer between the beams, relative positioning, the direction of the applied dynamic force, and representation of the source and target beams are studied. Then, the interaction model, material properties, acoustic element types in air, and the program codes required to define the fluid-structure interaction between air and the beams in FEA software are described one-by-one before reporting on the study results.





## **5. RESULTS**

### **5.1 Introduction**

In this section, results of doubly-clamped source and target beams placed in parallel both in and out-of-plane directions are presented. The source beam is excited mechanically by the distributed harmonic force. Generated mechanical vibrations on the source beam create pressure difference so called acoustic waves in air. The target beam absorbs acoustic waves at its resonance frequency and starts vibration with large gain in deflection magnitudes. While the motion and energy transition between the beams are nearly zero at off-resonant frequency band, they increase as approached to the vicinity of resonant frequency. Motion and energy transfer is studied separately for several beam geometries, various separation distances, relative positioning of the beams, and the viscous-damping ratios. For each condition simulated in ANSYS Inc., as described in Chapter 4, deformation values are numerically calculated via harmonic analysis. Energy transfer rates are obtained based on the obtained deformation values. Numerical results are as provided in the following sections of this chapter.

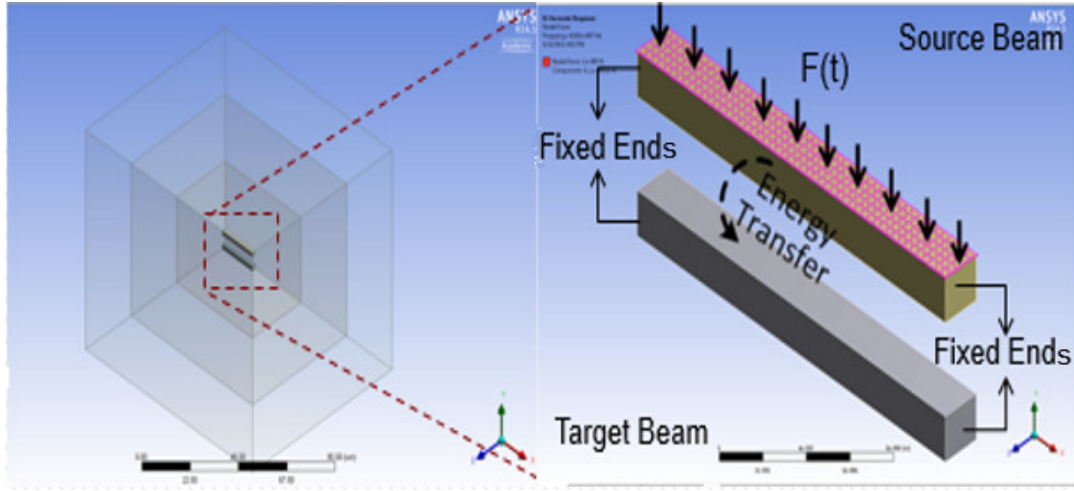
### **5.2 Energy Transfer between Beams with Neglected Viscous Damping Ratios**

Energy transfer rates are investigated in case of neglected viscous damping ratios at different separation values between beams, cross-section beam geometries, and relative positioning (alignment).

#### **5.2.1 Energy transfer between beams with square cross-section at out-of-plane alignment**

Doubly-clamped beams with square cross-sections are located in the out of plane direction. Harmonic oscillation is generated by exciting the source beam located on top. The acoustic effect of the vibration motion of the source beam on the target beam's vibration through the air is examined. Conceptual structure is as given in Fig. 5.1.

The beams are identical, and they are 20 $\mu\text{m}$ -long, and have a square cross-sectional area of 4 $\mu\text{m}^2$ .



**Figure 5.1 :** Simulation model utilized in the FEM Analysis.

First, natural frequencies of beams are calculated, and mode shapes are obtained in the *Modal Analysis Module*. As mentioned in Chapter 4, silicon is used as the beam material. After its natural frequencies are found numerically, they are verified analytically as well. Equation (2.100) in Chapter 2 is used in the analytical calculations. Equation (2.100) can be rewritten;

$$\omega = \beta^2 \sqrt{\frac{EI}{\rho A}} = (\beta L)^2 \sqrt{\frac{EI}{\rho AL^4}} \quad (5.1)$$

where  $E$  is Young's Modulus,  $\rho$  is the density,  $L$  is the length of the beam with their respective values of 165Gpa, 2330kg/m<sup>3</sup>, 20 $\mu\text{m}$ . In addition,  $A$  is the cross-sectional area, and  $I$  is the moment of inertia of the beam as well. Cross-sectional area is calculated using Eq. (5.2);

$$A = w.t \quad (5.2)$$

$$A = 2.10^{-6} m * 2.10^{-6} m = 4.10^{-12} m^2 \quad (5.3)$$

where  $w$  is width, and  $t$  is thickness with the values of 2.10<sup>-6</sup> m and 2.10<sup>-6</sup> m in order. With the help of Eq. (5.4), moment of inertia is calculated as given Eq. (5.5).

$$I = \frac{w.t^3}{12} \quad (5.4)$$

$$I = \frac{2 \cdot 10^{-6} \cdot (2 \cdot 10^{-6})^3}{12} \Rightarrow I = 1,3333 \cdot 10^{-24} m^4 \quad (5.5)$$

$\beta L$  is taken as 4,73 from Table 2.2, and used together with  $E$ ,  $I$ ,  $A$ ,  $L$  and  $\rho$  in Eq. (5.1). First natural frequency of the beam is calculated as given in Eq. (5.6);

$$\omega_1 = (4,73)^2 \sqrt{\frac{168 \cdot 10^9 * 1,3333 \cdot 10^{-24}}{2330 * 4 \cdot 10^{-12} (20 \cdot 10^{-6})^4}} \quad (5.6)$$

$$\omega_1 = 271747600 rad / sn \Rightarrow f_1 = 43,25 MHz$$

Natural frequencies of the beam in the vertical and horizontal directions,  $f_1$  and  $f_2$ , respectively, are same, 43,25MHz, due to square cross-section. The other natural frequencies of the beams can be calculated using Eq. (5.1) with corresponding values for density, cross-sectional area, Young's modulus, moment of beam inertias, and  $\beta_n L$  values as extracted from Table 2.2. 12 natural frequencies in different directions obtained numerically are as provided in Table 5.1.

**Table 5.1** : Numerical natural beam frequencies.

	<i>Natural Frequency (MHz)</i>	<i>Mode</i>
<b>1.</b>	40,944	1 <sup>st</sup> Mode in Y direction
<b>2.</b>	40,944	1 <sup>st</sup> Mode in Z direction
<b>3.</b>	105,15	2 <sup>nd</sup> Mode in Y direction
<b>4.</b>	105,15	2 <sup>nd</sup> Mode in Z direction
<b>5.</b>	121,66	1 <sup>st</sup> Torsional Mode
<b>6.</b>	190,45	3 <sup>rd</sup> Mode in Y direction
<b>7.</b>	190,45	3 <sup>rd</sup> Mode in Z direction
<b>8.</b>	211,33	1 <sup>st</sup> Mode in X direction
<b>9.</b>	243,31	2 <sup>nd</sup> Torsional Mode
<b>10.</b>	289,79	4 <sup>th</sup> Mode in Y direction
<b>11.</b>	289,79	4 <sup>th</sup> Mode in Z direction
<b>12.</b>	364,94	3 <sup>rd</sup> Torsional Mode

Five natural frequencies obtained analytically per horizontal and vertical directions are listed in Table 5.2 both in units of radian per second and Hertz.

**Table 5.2 :** Analytical natural beam frequencies.

	$\beta_n L$	Natural Frequency (rad/sec)	Natural Frequency (MHz)	Mode
1	4,7304	271747600	43,25	1 <sup>st</sup> Mode both in Y and Z directions
2	7,8532	749094700	119,22	2 <sup>nd</sup> Mode both in Y and Z directions
3	10,9956	1468525000	233,72	3 <sup>rd</sup> Mode both in Y and Z directions
4	14,1372	2427561000	386,36	4 <sup>th</sup> Mode both in Y and Z directions
5	17,2800	3626861000	577,23	5 <sup>th</sup> Mode both in Y and Z directions

Comparison of numerical and analytical natural frequency results yields Deviation Percentage (DP) as defined in Eq. (5.7);

$$DP = \frac{f_{analytical} - f_{numerical}}{f_{analytical}} * 100 \quad (5.7)$$

$$DP = \frac{43250000 - 40944000}{43250000} * 100 = 5,3\%$$

Having found the  $DP$  value as 5,3%, next maximum static deformations are calculated from;

$$EI \frac{\partial^4 w(x)}{\partial x^4} = -q \quad (5.8)$$

where  $w(x)$  is deflection of the beam as a function of position in  $x$  direction, and  $q$  is the distributed load. Both sides of the equation are then integrated four consecutive times to find  $w(x)$  as

$$w(x) = -\frac{qx^4}{24EI} + \frac{ax^3}{6} + \frac{bx^2}{2} + cx + d \quad (5.9)$$

In Eq. (5.9),  $a$ ,  $b$ ,  $c$ , and  $d$  are constants found from the boundary conditions. Deflection and slope are zero at  $x=0$  and  $x=L$  for doubly-clamped beams. Therefore;

$$w(0) = 0 \Rightarrow d = 0, \quad \frac{\partial w(0)}{\partial x} = 0 \Rightarrow c = 0, \quad (5.10)$$

$$w(L) = 0, \quad \frac{\partial w(L)}{\partial x} = 0 \Rightarrow a = \frac{qL}{2EI} \text{ and } b = -\frac{qL^2}{12EI} \quad (5.11)$$

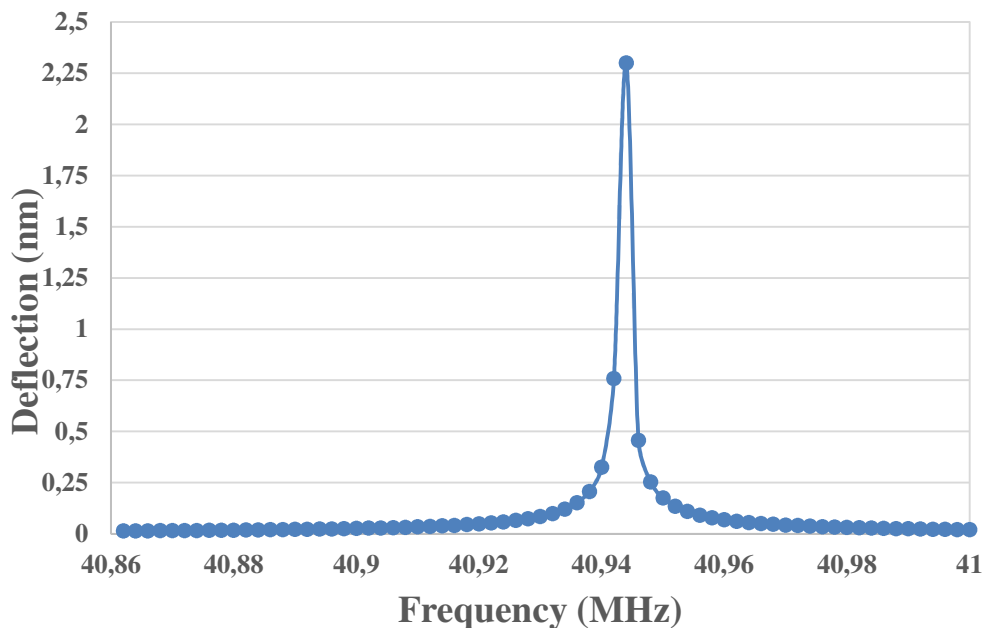
Provided that  $a$ ,  $b$ ,  $c$ , and  $d$  are constants obtained from the boundary conditions as written in Eq. (5.9),  $w(x)$  can be rewritten as depicted in Eq. (5.12);

$$w(x) = -\frac{qx^4}{24EI} + \frac{qLx^3}{12EI} + \frac{qL^2x^2}{24EI} \quad (5.12)$$

Maximum deflection, calculated for the distributed load of  $5 \cdot 10^{-11} \text{N/m}$  through Eq. (5.12), occurs at the beam midpoint.

$$w_{\max}(x) = -0,095 \cdot 10^{-12} \text{m} \quad (5.13)$$

After analytical calculation, a numerical maximum deflection value of  $-0,10495 \cdot 10^{-12} \text{m}$  is also obtained. Both values agree very well. The beam is studied numerically at the natural frequency range of the first mode in the *Harmonic Analysis Module* and deflection values obtained are as given in Table 5.3. Deflection results provided in Table 5.3 are plotted and illustrated in the chart Fig. 5.2. Both indicate a maximum deflection of 2,30nm at the natural frequency of the fundamental mode.

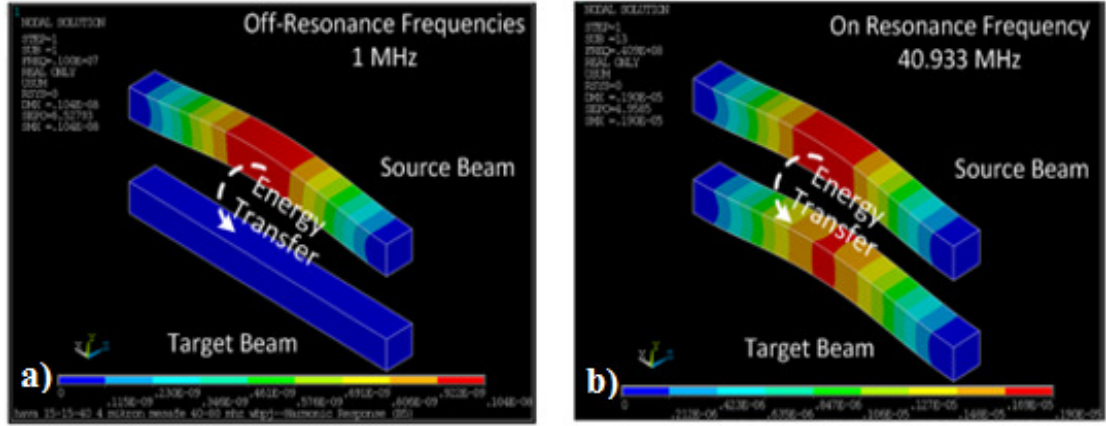


**Figure 5.2** : Beam deflection values about the fundamental mode frequency.

**Table 5.3 :** Frequency-dependent deformation values.

<i>Frequency (MHz)</i>	<i>Deflection (nm)</i>	<i>(cont'd) Frequency (MHz)</i>	<i>(cont'd) Deflection (nm)</i>
40,862	0,014	40,932	0,0991
40,864	0,0144	40,934	0,12
40,866	0,0147	40,936	0,152
40,868	0,0151	40,938	0,207
40,87	0,0155	40,94	0,325
40,872	0,016	40,942	0,758
40,874	0,0164	40,944	2,3
40,876	0,0169	40,946	0,457
40,878	0,0174	40,948	0,254
40,88	0,018	40,95	0,176
40,882	0,0186	40,952	0,134
40,884	0,0192	40,954	0,109
40,886	0,0198	40,956	0,0913
40,888	0,0206	40,958	0,0787
40,89	0,0213	40,96	0,0691
40,892	0,0222	40,962	0,616
40,894	0,0231	40,964	0,0556
40,896	0,024	40,966	0,0507
40,898	0,0251	40,968	0,0465
40,9	0,0262	40,97	0,0430
40,902	0,0275	40,972	0,04
40,904	0,0289	40,974	0,0374
40,906	0,0304	40,976	0,0351
40,908	0,0321	40,978	0,033
40,91	0,0341	40,98	0,0312
40,912	0,0362	40,982	0,0296
40,914	0,0387	40,984	0,0281
40,916	0,0415	40,986	0,0268
40,918	0,0447	40,988	0,0256
40,92	0,0485	40,99	0,0245
40,922	0,053	40,992	0,0235
40,924	0,0585	40,994	0,0226
40,926	0,0652	40,996	0,0217
40,928	0,0736	40,998	0,0209
40,93	0,0845	41	0,0202

Then, beam deflections are calculated in air at the existence of a pair of beams, namely source and target beams. Effect of source beam on target beam is examined at the resonant and off-resonant frequencies. While there is no energy transition from source to target at off-resonant frequencies, significant transition at the resonant frequency is observed as evidenced in Figs. 5.3a and 5.3b.



**Figure 5.3 :** Coupled vibration responses of beams with square cross-section at out-of-plane alignment: a) At off-resonant frequencies. b) At on-resonant frequency.

The model is simulated around the first natural frequency. When efficiency of energy interaction between the beams are investigated, strain energies of source and target beams are used for quantitative comparison.

A ratio called as Energy Transfer Rate (*ETR*) is employed to characterize changes in the energy interaction as a function of distance. As given in Eq. (5.14), percent *ETR* values are calculated as a fraction of strain energy of target beam over that of the source beam.

$$ETR = \frac{U_{T,max}}{U_{S,max}} * 100 \quad (5.14)$$

where  $U_{S,max}$  and  $U_{T,max}$  are strain energies of source and target beams, respectively. Strain energy formulation is given in Eq. (5.15);

$$U_{max} = \frac{1}{2} q w_{max} \quad (5.15)$$

where  $w_{max}$  is the maximum deflection of beams,  $q$  is the distributed load. The expression of energy in Eq. (5.15) is an equation dependent on the force and deflection.

The expression of the force dependency on deflection for both-end-fixed beam can be written as Eq. (5.16);

$$q = \frac{384EI}{L^4} w_{\max} \quad (5.16)$$

Equation (5.15) is inserted in Eq. (5.16) in order to achieve energy-only expression dependent on the deformations as obtained in Eq. (5.17);

$$U_{\max} = \frac{192EI}{L^4} w_{\max}^2 \quad (5.17)$$

As indicated in Eq. (5.17), strain energy is proportional to the square of beam deflections. If Eq. (5.17) is inserted into Eq. (5.14), *ETR* can be rewritten as;

$$ETR = \frac{\frac{192 E_T I_T}{L_T^4} w_{T,\max}^2}{\frac{192 E_S I_S}{L_S^4} w_{S,\max}^2} * 100 \quad (5.18)$$

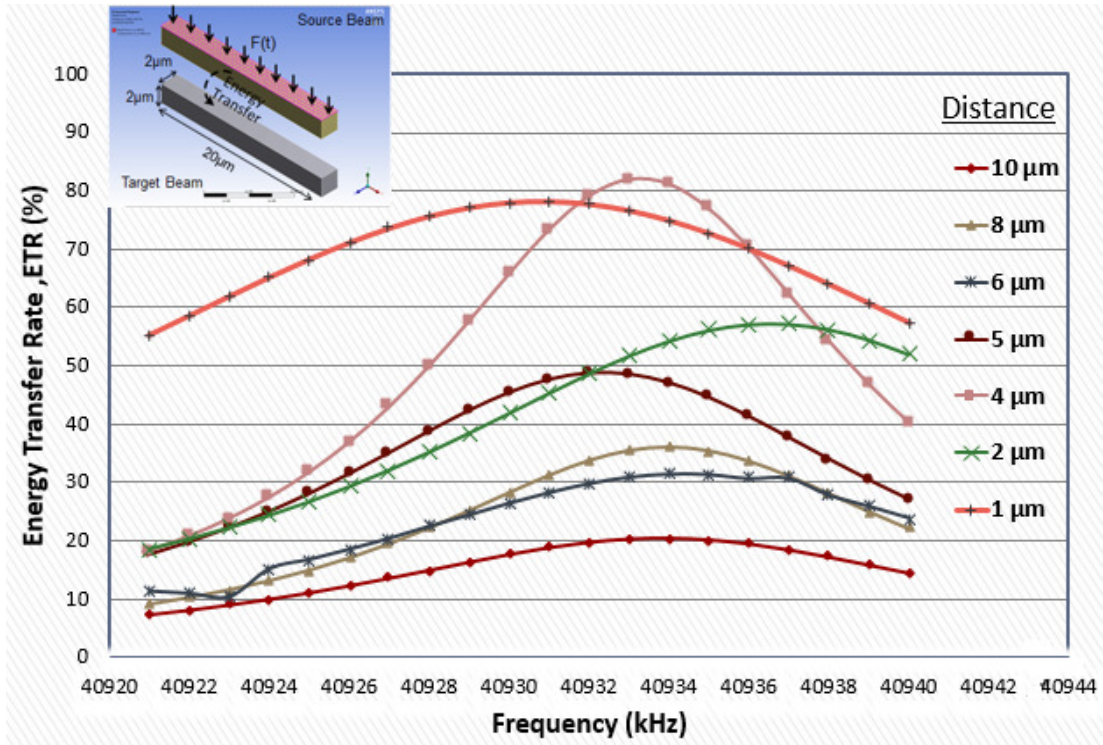
where  $E_S$ ,  $I_S$ ,  $L_S$  and  $w_{S,\max}$  are Young's modulus, moment of inertia, length and maximum deflection of the source beam, respectively.

$E_T$ ,  $I_T$ ,  $L_T$  and  $w_{T,\max}$  are Young's modulus, moment of inertia, length and maximum deflection of the target beam, respectively. Since the dimensions and material of the source and target beams are same,  $E_S$  and  $E_T$ ,  $I_S$  and  $I_T$ , and  $L_S$  and  $L_T$  parameters also become identical. Therefore,  $E$ ,  $I$  and  $L$  values cancel each other in Eq. (5.18) yielding;

$$ETR = \frac{w_{T,\max}^2}{w_{S,\max}^2} * 100 \quad (5.19)$$

Energy transfer between beams with square cross-section at out of plane alignment has been simulated for various distances. Deflection and *ETR* results are as listed in Tables A.1-7 in Appendix A. *ETRs* are calculated using those deflections in Eq. (5.19) also given in Fig. 5.4.





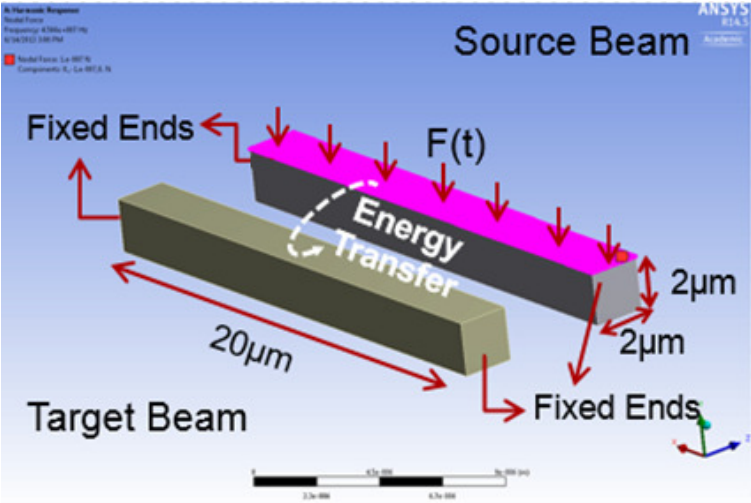
**Figure 5.4 :** *ETRs* depending on distance between beams with square cross-section at out of plane alignment.

As indicated in Figure 5.4, *ETRs* dependency on the distance are calculated utilizing seven distance values between 1 and 10 $\mu\text{m}$ , and 20-frequency values between 40920 and 40940kHz. Minimum *ETR* is obtained to be 21% at 40933kHz at the 10 $\mu\text{m}$  distance. Maximum *ETR*, on the other hand, is 82% at 40933kHz at 4 $\mu\text{m}$  distance. However, a steady increase in *ETR* is not observed with the decrease in distance.

Reasons why *ETRs* show an irregular behavior of increase with the distance are investigated, two possible causes are considered. The first reason is that distances constantly change during oscillations since the beams are placed at out of plane alignment. The second reason is the use of square cross-section beams, where provided that natural frequencies in both directions are equal, target beam gets coupled in both directions without any direction selectivity. This situation adversely affects the energy transferred from source beam to target beam. Hence, developing a steady relationship between *ETR* with the distance by eliminating these problems in the following sections is aimed.

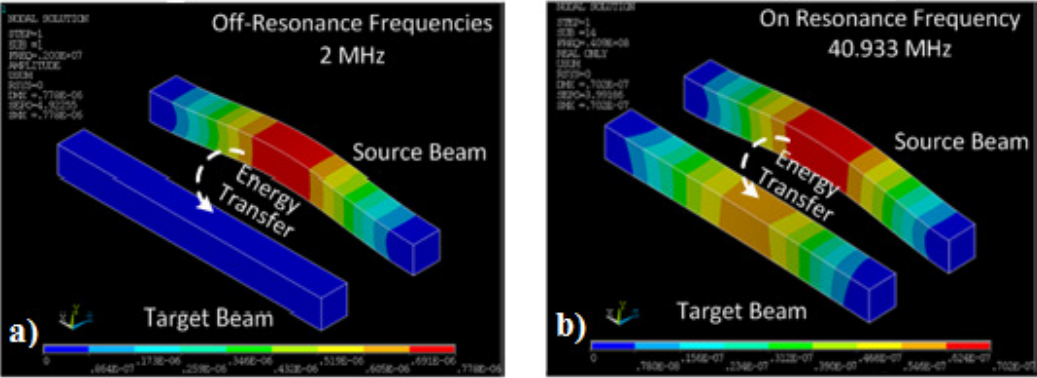
**5.2.2 Energy transfer between beams with square cross-section at in-plane alignment**

In this section, the problem mentioned in the previous section is aimed to be eliminated. Hence, beams placed vertically are studied at in-plane alignment. Both beams are considered to move in parallel relatively by electrostatic force exerted to the upper surface of the source beam. Thus, the first problem would be eliminated. The beam dimensions do not change, and the relevant model concept evolves to what is seen in Fig. 5.5.



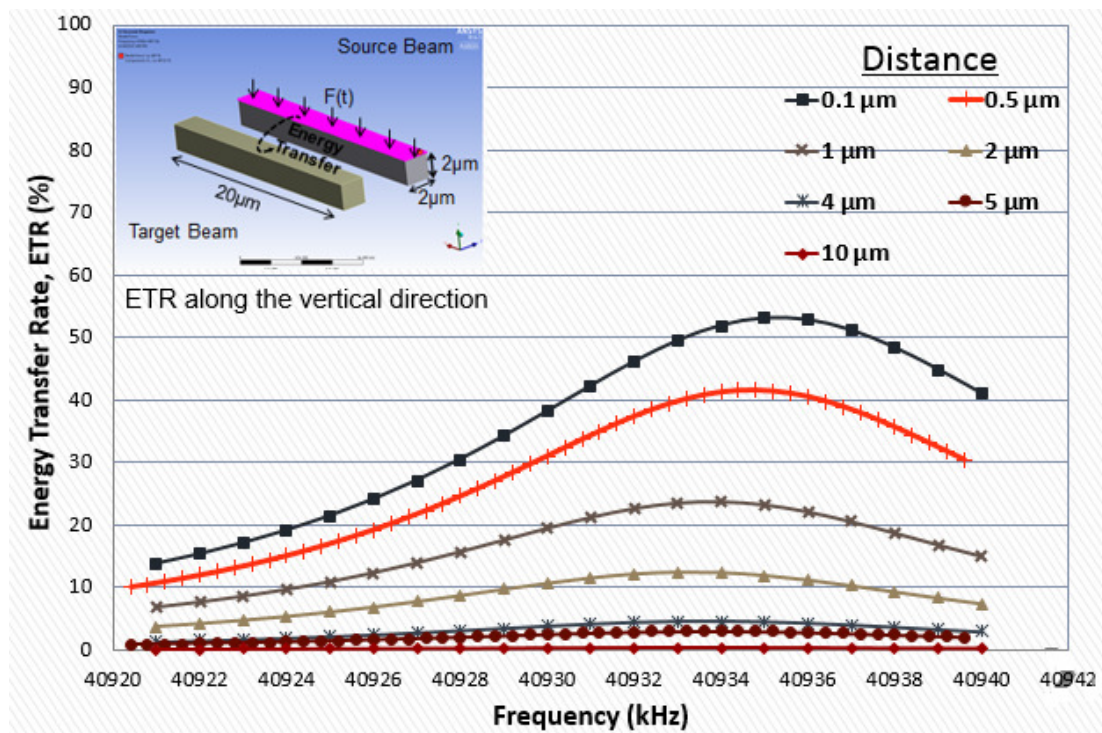
**Figure 5.5 :** Beam geometries with square cross-section at in-plane alignment.

First, beams placed in-plane are simulated for off and on resonant frequencies, and vibration responses as given in Figs. 5.6a and 5.6b are obtained. While energy transfer between beams is not observed at off-resonant frequencies, it is observed at on-resonant frequency band.



**Figure 5.6 :** Coupled vibration responses of beams placed at in-plane alignment: a) At off-resonant frequencies. b) At on-resonant frequency.

Simulations are repeated for seven distance values between  $0.1\mu\text{m}$  and  $10\mu\text{m}$ . Obtained deflection values are listed in Tables B.1-7 in Appendix B. Then, as illustrated in Fig. 5.7, *ETRs* as a function of distance are calculated in a band from  $40920\text{kHz}$  to  $40940\text{kHz}$ . When distance value is decreased from  $10\mu\text{m}$  to  $0.1\mu\text{m}$ , *ETR* shows a steady increase. Maximum energy transfer rate is found as  $53\%$  for  $0.1\mu\text{m}$ . *ETR* decreases with the increase of distance, and is about  $41\%$  for  $0.5\mu\text{m}$ ,  $24\%$  for  $1\mu\text{m}$ ,  $12.5\%$  for  $2\mu\text{m}$ ,  $4.6\%$  for  $4\mu\text{m}$ ,  $3\%$  for  $5\mu\text{m}$ ,  $0.35\%$  for  $10\mu\text{m}$ . *ETR* is nearly zero for values less than  $10\mu\text{m}$ .

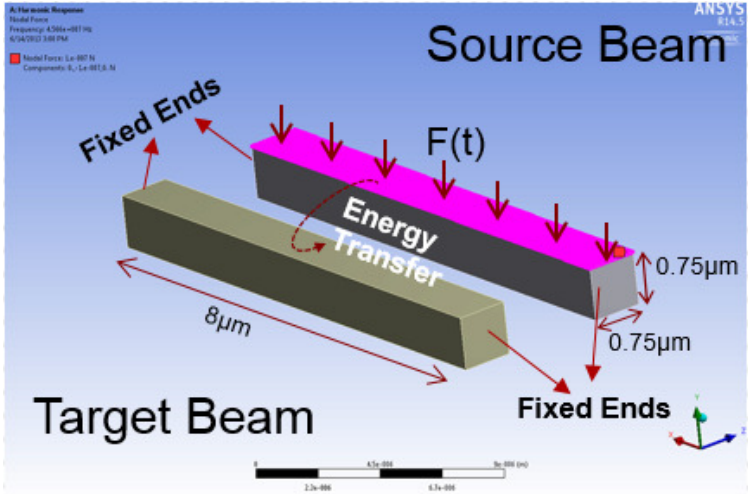


**Figure 5.7 :** *ETRs* versus distance results between beams with square cross-section at in-plane alignment.

Although *ETR* properly increases with decreasing distance, these values are even insufficient at very small distances about  $0.1\mu\text{m}$ . Energy transfer between beams with smaller geometries is investigated to increase *ETR*. Hence, as discussed in the next section, beam sizes are reduced by three-folds, and change in *ETR* is examined.

**5.2.3 Energy transfer for smaller beams with square cross-section at in-plane alignment**

In this section, beams three times smaller are utilized, because *ETRs* obtained in the previous section are at insufficient levels. As demonstrated in Fig. 5.8, the new beams are 8µm-long, and have a square cross-sectional area of 0.75×0.75µm<sup>2</sup>.



**Figure 5.8 :** Smaller beam geometries with square cross-section at in-plane alignment.

Beams are arranged in parallel within the same horizontal plane. First, beam natural frequencies are calculated by *Modal Analysis* in ANSYS FEA software. Natural frequencies are confirmed analytically as well as listed in Tables 5.4 and 5.5.

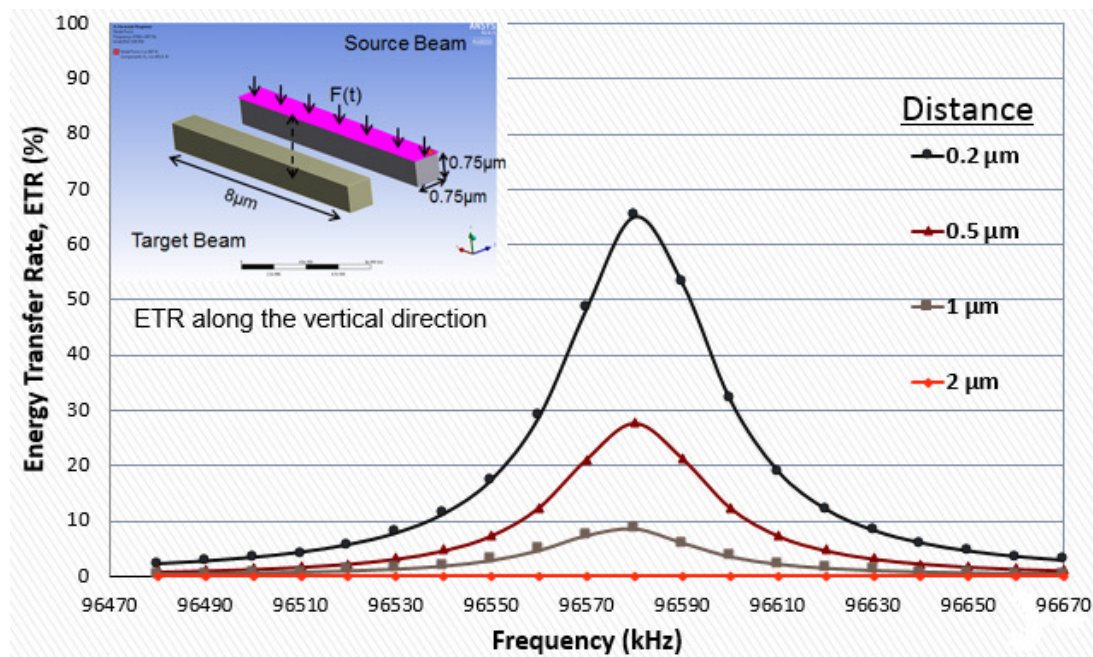
**Table 5.4 :** Natural frequencies of smaller beam by simulation.

	<i>Natural Frequency(MHz)</i>	<i>Mode</i>
1.	96,634	1 <sup>st</sup> Mode in Y direction
2.	96,634	1 <sup>st</sup> Mode in Z direction
3.	249,67	2 <sup>nd</sup> Mode in Y direction
4.	249,67	2 <sup>nd</sup> Mode in Z direction
5.	303,99	1 <sup>st</sup> Torsional Mode
6.	455,28	3 <sup>rd</sup> Mode in Y direction
7.	455,29	3 <sup>rd</sup> Mode in Z direction
8.	528,04	1 <sup>st</sup> Mode in X direction
9.	607,95	2 <sup>nd</sup> Torsional Mode
10.	696,87	4 <sup>th</sup> Mode in Y direction
11.	696,87	4 <sup>th</sup> Mode in Z direction
12.	911,87	3 <sup>rd</sup> Torsional Mode

**Table 5.5 :** Natural frequencies of smaller beam analytically.

	$\beta nL$	Natural Frequency(rad/sec)	Natural Frequency(MHz)	Mode
1	4,73	636908400	101,37	1 <sup>st</sup> Mode both in Y and Z directions
2	7,8532	1755691000	279,43	2 <sup>nd</sup> Mode both in Y and Z directions
3	10,9956	3441855000	547,79	3 <sup>rd</sup> Mode both in Y and Z directions
4	14,1372	5689597000	905,53	4 <sup>th</sup> Mode both in Y and Z directions
5	17,28	8500455000	1352,9	5 <sup>th</sup> Mode both in Y and Z directions

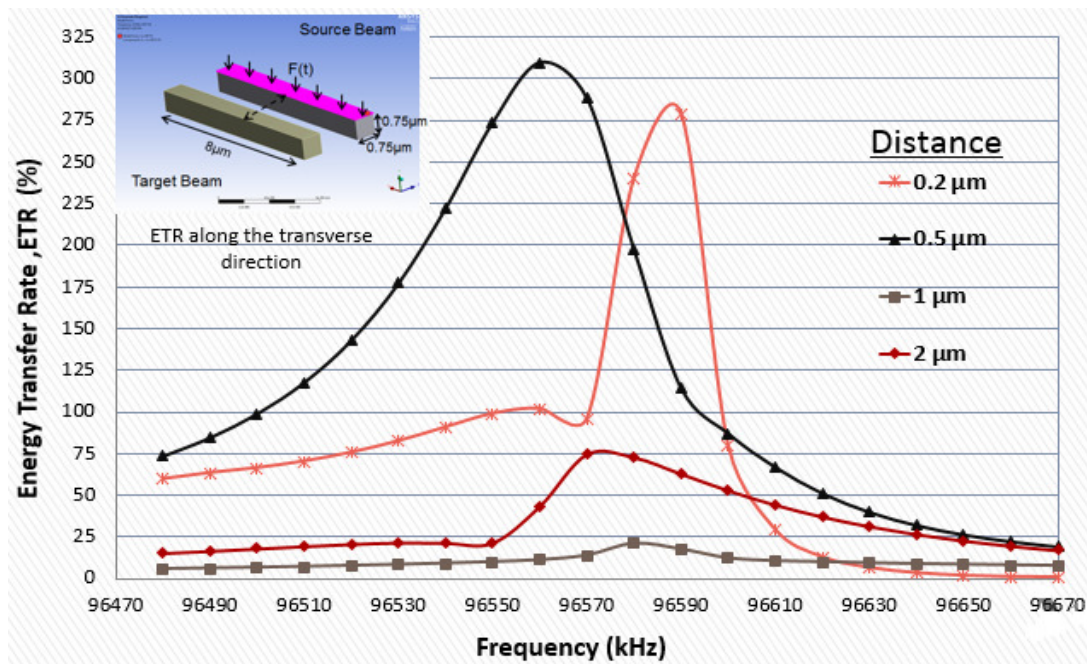
Natural frequency of the first mode in Y direction obtained from simulations, 96533kHz, is smaller approximately by 4% than that from the analytical solution, which is attributed to the minimum mesh size achievable with available computational resources at hand. *ETRs* for a certain distance are numerically studied at every 10kHz from 96470kHz to 96670kHz. Corresponding deflection and *ETR* values are listed in Tables C.1-8 in Appendix C. The study is recurred for a total of four distances as 0.2 $\mu\text{m}$ , 0.5 $\mu\text{m}$ , 1 $\mu\text{m}$  and 2 $\mu\text{m}$ . *ETRs* calculated are as depicted in Fig. 5.9. *ETRs* presented herein are calculated considering beam deflection values in the out-of-plane direction.



**Figure 5.9 :** *ETRs* in the out-of-plane direction as a function of distance between smaller beams with square cross-section at in-plane alignment.

As seen in Figure 5.9, *ETR* increases with decreasing distances. Maximum *ETR* is obtained to be approximately 65% at  $0.2\mu\text{m}$  at  $96580\text{kHz}$ . While The *ETR* is slightly larger with respect to the energy transfer between the larger size beams at  $0.2\mu\text{m}$ , it is slightly less at greater than  $0.5\mu\text{m}$ . *ETRs* decrease down to almost zero in distances greater than  $2\mu\text{m}$ .

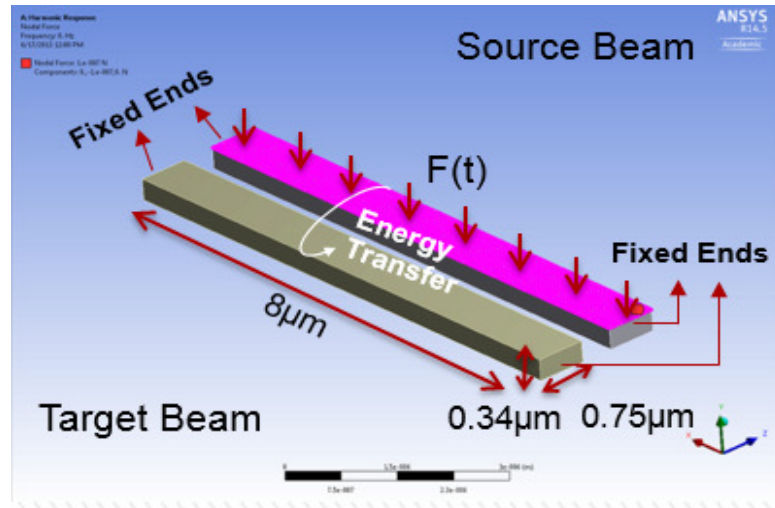
After *ETRs* are examined in the out-of-plane direction, they are investigated also in the in-plane direction. Obtained values are as shared in Fig. 5.10. A regular change is not observed with the change in the distance in *ETR*. Maximum energy transfer rate is obtained at  $0.5\mu\text{m}$  about  $96560\text{kHz}$ . Although, consistent increase in *ETR* with decreasing distance is expected, results yielded indicate an irregular order. This particular phenomenon of the disorders are thought to arise from the use of square-sectioned beams, where natural frequencies of the beams become equal inducing shared mechanical coupling in both Y and Z directions. Therefore, target beam may be adversely affected in energy transfer with *MRA* because of identical natural frequencies in both directions. The issue, as presented in the next section, is addressed via utilization of beams with rectangular cross-section rather than those with square cross-section in order to obtain a regular change in *ETRs* in both directions as a function of distance.



**Figure 5.10 :** *ETR* in the transverse direction with distance between smaller beams with square cross-section at in-plane alignment.

### 5.2.4 Energy transfer for beams with rectangular cross-section at in-plane alignment

In order to achieve regularly ordered change with distance and maximum *ETR*, *MRA* between beams with rectangular cross-section at in-plane alignment using out-of-plane vibration directions is investigated in this section as shown in Fig. 5.11. Beams employed herein are  $8\mu\text{m}$ -long,  $0.75\mu\text{m}$ -wide and  $0.34\mu\text{m}$ -thick.



**Figure 5.11** : Beam geometries with rectangular cross-section.

Natural frequencies are numerically calculated with *Modal Analysis* for new beam geometry in ANSYS FEA software as provided in Table 5.6. Then, the natural frequencies are validated analytically, whose results are as listed in Table 5.7.

**Table 5.6** : Natural frequencies of the beam with rectangular cross-section studied numerically.

	<i>Natural Frequency(MHz)</i>	<i>Mode</i>
<b>1</b>	45,716	1 <sup>st</sup> Mode in Y direction
<b>2</b>	96,309	1 <sup>st</sup> Mode in Z direction
<b>3</b>	124,09	2 <sup>nd</sup> Mode in Y direction
<b>4</b>	235,78	1 <sup>st</sup> Torsional Mode
<b>5</b>	238,59	3 <sup>rd</sup> Mode in Y direction
<b>6</b>	249,17	2 <sup>nd</sup> Mode in Z direction
<b>7</b>	385,29	4 <sup>th</sup> Mode in Y direction
<b>8</b>	454,49	3 <sup>rd</sup> Mode in Z direction
<b>9</b>	472,58	2 <sup>nd</sup> Torsional Mode
<b>10</b>	527,47	1 <sup>st</sup> Mode in X direction
<b>11</b>	560,44	5 <sup>th</sup> Mode in Y direction
<b>12</b>	695,85	4 <sup>th</sup> Mode in Z direction

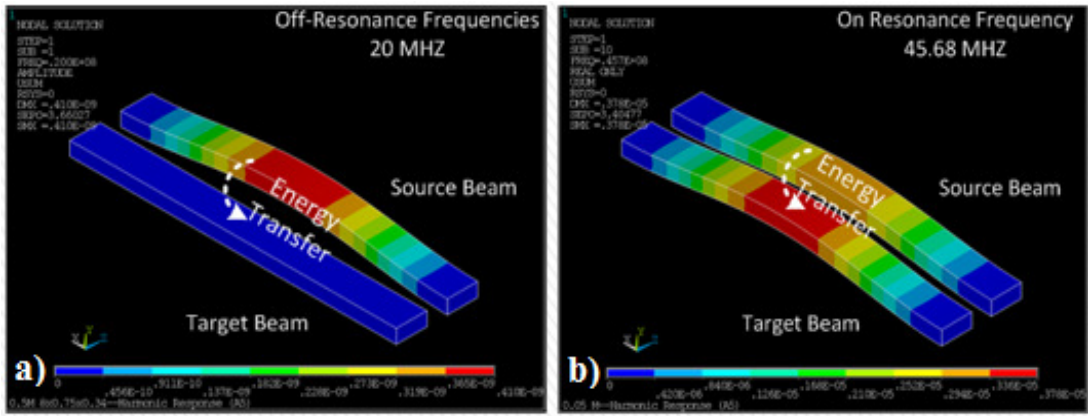
**Table 5.7 :** Natural frequencies of the beam with rectangular cross-section studied analytically.

	$\beta nL$	Natural Frequency(rad/sec)	Natural Frequency(MHz)	Mode
1	4,73	288731797	45,953093	1 <sup>st</sup> Mode in Y direction
2	4,73	636908375	101,367116	1 <sup>st</sup> Mode in Z direction
3	7,8532	795913090	126,673503	2 <sup>nd</sup> Mode in Y direction
4	10,9956	1560307503	248,330652	3 <sup>rd</sup> Mode in Y direction
5	7,8532	1755690640	279,426844	2 <sup>nd</sup> Mode in Z direction
6	14,1372	2579283831	410,505771	4 <sup>th</sup> Mode in Y direction
7	10,9956	3441854786	547,788203	3 <sup>rd</sup> Mode in Z direction
8	17,28	3853539437	613,309850	5 <sup>th</sup> Mode in Y direction
9	14,1372	5689596687	905,527437	4 <sup>th</sup> Mode in Z direction
10	17,28	8500454641	1352,889375	5 <sup>th</sup> Mode in Z direction

When numerical and analytical natural frequencies are compared, it is seen that these values are in very good agreement, where the difference is only 0.5%, the former being smaller. Disagreement between the numerical and analytical solutions is understood to decrease from 4% to 0.5% when beams with rectangular cross-sections compared to those with square ones are utilized provided that mesh sizes are identical.

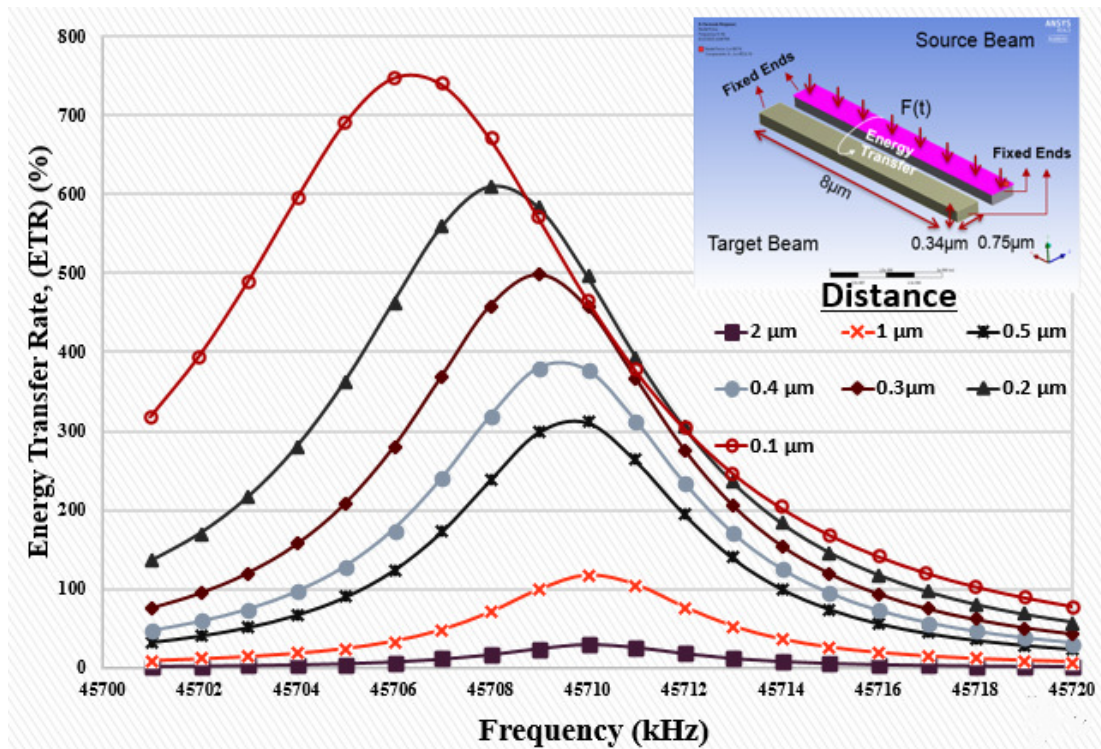
After the calculation of natural frequencies, energy transfer with *MRA* between the beams with rectangular cross-section are investigated at off-resonant and on-resonant frequencies in *Harmonic Analysis Module*. Dynamic response is obtained from the numerical results are as given in Figs. 5.12a and 5.12b for both cases, respectively. As can be seen in Fig. 5.12, while there is no energy transfer from source to target beam at off-resonant frequencies, there is remarkable energy transfer at on-resonant frequency band.





**Figure 5.12 :** Coupled vibration responses of beams with rectangular cross-section placed at in-plane alignment: a) At off-resonant frequencies. b) At on-resonant frequency.

*ETR* at rectangular cross-sections are studied for distances in the range from 100nm to 2 $\mu$ m, and results are as presented in Fig. 5.13, and the deflection results are as listed in Tables D.1-7 in Appendix D. *ETRs* are increasing meaningfully with the decreasing distance. While *ETR* is 29.3% at 2 $\mu$ m, it reaches upto 117% at 1 $\mu$ m. Energy transfer rates are over 100% in the distance values smaller than 1 $\mu$ m. *ETRs* over 100% are obtained owing to the fact that target beam may deform greater than the source beam at resonance in a beam structure as stated in Strain Energy Formulations.



**Figure 5.13 :** *ETR* versus distance between beams with rectangular cross-section at in-plane alignment.

*ETRs* are not only examined in the out-of-plane vibration direction, but they are also studied in the transverse direction. Results prove that *ETRs* in the vertical direction are understood to be identical with those in the transverse direction. The conflict of having identical natural frequencies in both Y and Z directions is prevented by use of beams with rectangular cross-sections instead of those with square cross-section. As a result, deployment of beams with rectangular cross-section provides two important benefits. First, *ETRs* become equal in both directions, and change regularly with the separation distance. Second, *ETRs* become larger than those with square cross-sections.

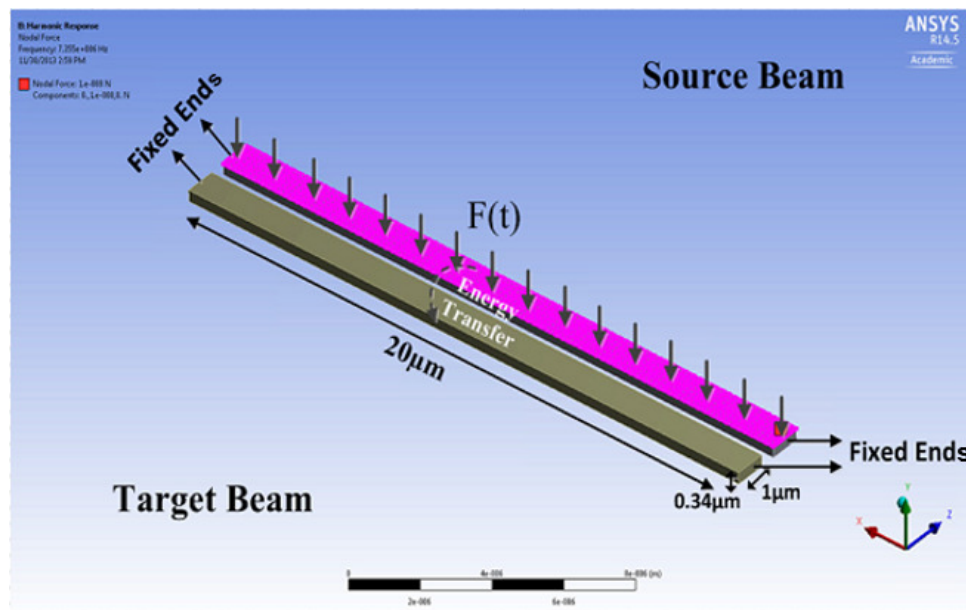
Another remarkable aspect in utilization of such a system configuration is that for distance values definitely less than or equal to 430nm, redshift in the system's resonance frequency takes place. The effect is thought to be due to the change in the damping ratio at very small distances, or probably fast return of acoustic waves from the target beam located in very close proximity of the source beam, or interaction due to such surface molecular forces as Van der Waals or Casimir, or a combination of those. Exact reasoning of the cause of the particular effect is intended to be clarified after experimental study. However, it is certain that the results obtained in this section show how important use of beams with rectangular cross-section is.

### **5.2.5 Energy transfer in micromachinable and characterizable cantilever beams with rectangular cross-section aligned at in-plane orientations**

In this part of the study, beam geometries are reconsidered by taking constraints of manufacturing and measurement into account in order for confirmation of experimental energy transfer rates obtained in the simulations. Any unsuitability noticed is to be corrected such that beams we will experimentally investigate are also going to satisfy requirements of micro/nano-fabrication and characterization. In case of any geometry modification in the beams, *ETRs* need to be recalculated for update purposes while all of the previously understood concepts remain applicable and unchanged. For instance, as discussed in the previous sections, use of beams with rectangular cross-section still remains advantageous. In the selection of geometrical dimensions of beams, such facts as that wafers with not all thicknesses are available to us, only thicknesses as 500nm and 340nm at device silicon layer are available, play an important role. Characteristics of measurement equipment are also critical as other constraints so as to properly characterize micromachined devices exist. For example,

beam thickness should be about 340nm in order to perform optical measurements of mechanical oscillations of beams precisely and in real-time for embedded accurate characterization on single-mode 340 nm-thick waveguides as Optical Directional Coupler (ODC) sensors.

The beam length has been determined according to constraints of characterization equipment. For example, operating ranges of signal generator and piezoelectric voltage amplifier are used to actuate source beam electrostatically. Hence, maximum frequency studiable is 10MHz for non-sinusoidal excitation waves used to apply electrostatic forces over a wide range. Beam widths are selected as to be 1 $\mu$ m so that the beam thickness is different in order to achieve rectangular cross-section for effective energy transfer as aforementioned. Because the operating frequency is less than 10MHz, natural frequencies of the beams with different lengths are calculated, and the length of beam is optimized as 20 $\mu$ m. Therefore, the beams are 20 $\mu$ m-long, 1 $\mu$ m-wide and 0.34 $\mu$ m-thick, and they are placed at in-plane orientation. Conceptual illustration is as given in Fig. 5.14.



**Figure 5.14** : Finalized beam geometries at in-plane orientation.

After determination of beam size, natural frequencies and mode shapes are recalculated in *Modal Analysis* in ANSYS FEA software. Natural frequencies obtained numerically are as listed in Table 5.8. Then, natural frequencies are analytically calculated, and given in Table 5.9.

**Table 5.8 :** Numerical natural frequency values of the beam.

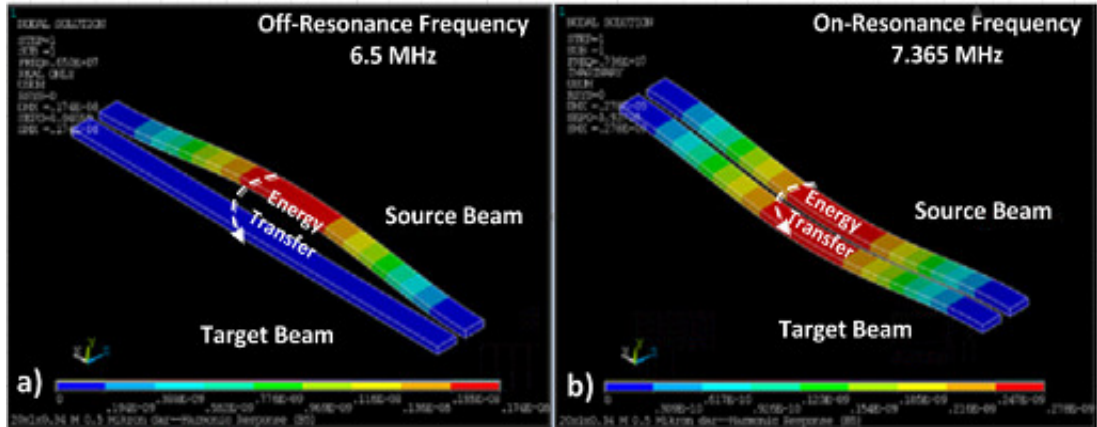
	<i>Natural Frequency(MHz)</i>	<i>Mode</i>
<b>1</b>	7,3665	1 <sup>st</sup> Mode in Y direction
<b>2</b>	20,256	2 <sup>nd</sup> Mode in Y direction
<b>3</b>	21,314	1 <sup>st</sup> Mode in Z direction
<b>4</b>	39,580	3 <sup>rd</sup> Mode in Y direction
<b>5</b>	57,554	2 <sup>nd</sup> Mode in Z direction
<b>6</b>	65,165	4 <sup>th</sup> Mode in Y direction
<b>7</b>	76,588	1 <sup>st</sup> Torsional Mode
<b>8</b>	96,877	5 <sup>th</sup> Mode in Y direction
<b>9</b>	109,910	3 <sup>rd</sup> Mode in Z direction
<b>10</b>	134,560	6 <sup>th</sup> Mode in Y direction
<b>11</b>	153,350	2 <sup>nd</sup> Torsional Mode
<b>12</b>	176,130	4 <sup>th</sup> Mode in Z direction

**Table 5.9 :** Analytical natural frequency values of the beam.

	$\beta nL$	<i>Natural Frequency(rad/sec)</i>	<i>Natural Frequency(MHz)</i>	<i>Mode</i>
<b>1</b>	4,73	46197087	7,352495	1 <sup>st</sup> Mode in Y direction
<b>2</b>	7,8532	127346094	20,267760	2 <sup>nd</sup> Mode in Y direction
<b>1</b>	4,73	135873787	21,624985	1 <sup>st</sup> Mode in Z direction
<b>3</b>	10,9956	249649200	39,732904	3 <sup>rd</sup> Mode in Y direction
<b>2</b>	7,8532	374547337	59,611060	2 <sup>nd</sup> Mode in Z direction
<b>4</b>	14,1372	412685413	65,680923	4 <sup>th</sup> Mode in Y direction
<b>5</b>	17,28	616566310	98,129576	5 <sup>th</sup> Mode in Y direction
<b>3</b>	10,9956	734262354	116,861483	3 <sup>rd</sup> Mode in Z direction
<b>4</b>	14,1372	1213780627	193,179187	4 <sup>th</sup> Mode in Z direction
<b>5</b>	17,28	1813430323	288,616400	5 <sup>th</sup> Mode in Z direction

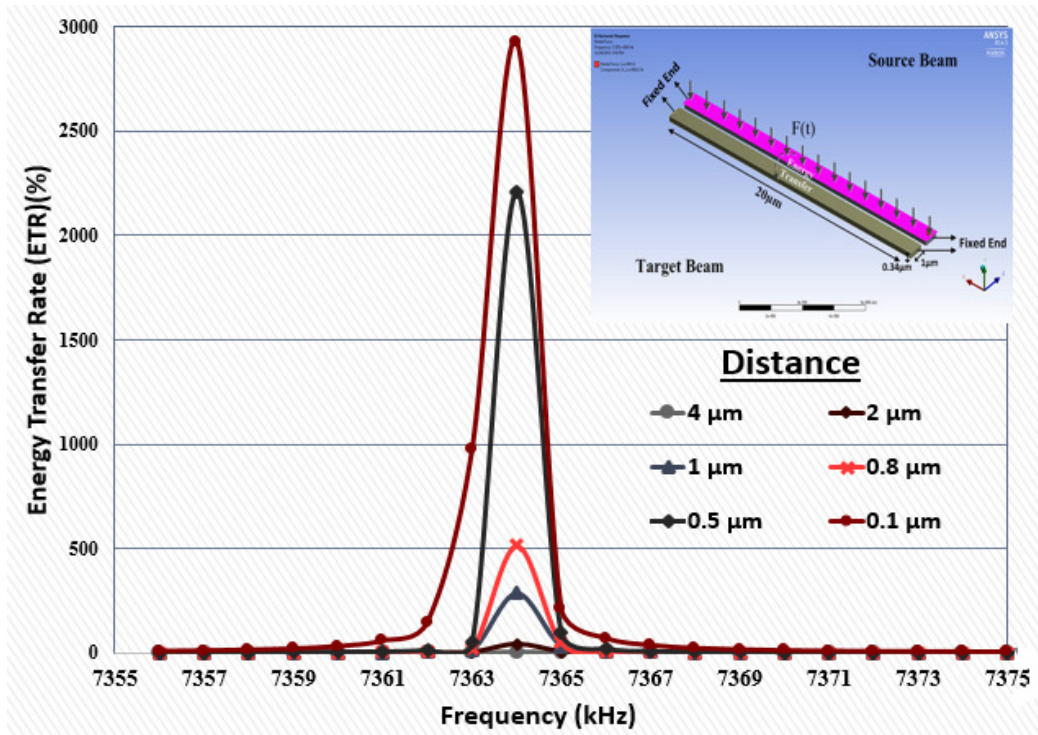
Analytical and numerical natural frequencies obtained are compared. The disagreement is as small as 0.19%.

As mentioned in the previous sections, beams are analyzed at off-resonant and on-resonant frequencies. Energy transfer has not been observed at off-resonant frequencies. Coupled vibration responses are as given in Fig. 5.15.



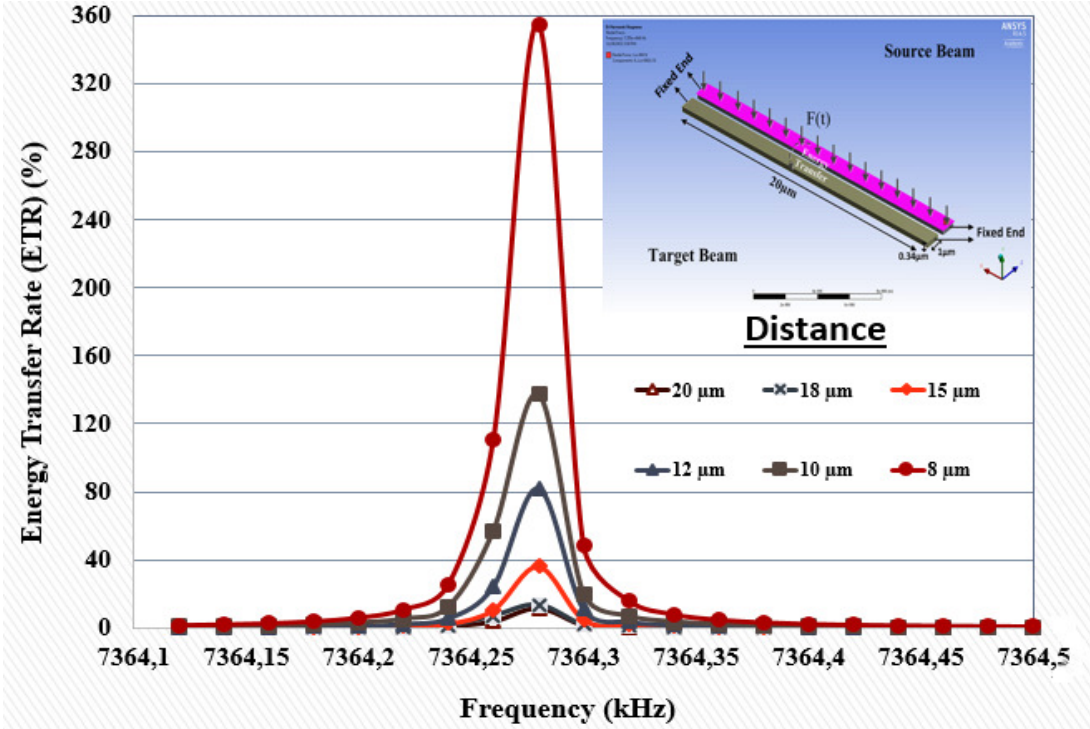
**Figure 5.15 :** Coupled vibration responses of micromachinable beams: a) Off-resonant frequencies. b) On-resonance frequency.

After calculation of natural frequencies, *ETR* between the beams are calculated in *Harmonic Analysis* around the fundamental natural frequency. *ETRs* are obtained by repetitive simulations at the resonance frequency for various distances. *ETRs* obtained are given in Fig. 5.16. Corresponding deflection values are listed in Tables E.1-6 in Appendix E.



**Figure 5.16 :** *ETRs* as a function of distance for micromachinable beams.

As shown in Fig. 5.16, the simulations are performed for six different distances between  $0.1\mu\text{m}$  and  $4\mu\text{m}$ . *ETR* is about 5% at  $4\mu\text{m}$ , 42% at  $2\mu\text{m}$ , 286% at  $1\mu\text{m}$ , 513% at  $0.8\mu\text{m}$ , and 2210% at  $0.5\mu\text{m}$ . When distance is reduced down to  $0.1\mu\text{m}$ , *ETR* reaches its maximum, 2925%. *ETRs* quickly increase with decreasing distance from  $2\mu\text{m}$  to  $1\mu\text{m}$ . *ETR* values in the vertical direction increase in an ordered manner depending on the distance. In addition, *ETRs* in vertical and transverse directions are at similar levels. *ETRs* calculated for micromachinable beams are at higher levels compared to those in the previous sections. Increase in both the length and width of the beam from  $8\mu\text{m}$  to  $20\mu\text{m}$ , and from  $0.75\mu\text{m}$  to  $1\mu\text{m}$ , respectively, ensure both reduction in excitation frequency and obtaining higher *ETRs*. Therefore, the ultimate geometry is understood to be better than previously studied. Results of *ETRs* obtained at 1kHz frequency intervals are as presented in Fig.5.16. They are almost zero at distances greater than  $4\mu\text{m}$ , and this is attributed to the fact that intervals of 1kHz in the study is relatively wide in range such that results may indeed be belonging to frequencies far from the resonance. Thus, simulations are repeated by narrowing the frequency range under investigation for greater distances. *ETRs* obtained from the numerical study are as presented in Fig. 5.17. Corresponding deflection values are listed meticulously in Tables E.7-12 in Appendix E.



**Figure 5.17 :** *ETRs* as a function of greater distances for micromachinable beams at narrower frequency ranges.

As shown in Fig. 5.17, *ETRs* are calculated for six different distances between  $8\mu\text{m}$  and  $20\mu\text{m}$  in the frequency band of  $20\text{Hz}$ . While *ETR* is  $5\%$  at  $4\mu\text{m}$  distance in the frequency band of  $1000\text{Hz}$ , energy is thought to be transferrable from the source beam to the target beam at distances even greater than  $20\mu\text{m}$  in very narrow frequency ranges. *ETR* at  $7364280\text{Hz}$  is about  $11.7\%$  at  $20\mu\text{m}$ ,  $13\%$  at  $18\mu\text{m}$ ,  $36.3\%$  at  $15\mu\text{m}$ ,  $81.8\%$  at  $12\mu\text{m}$ ,  $137.4\%$  at  $10\mu\text{m}$ , and  $355\%$  at  $8\mu\text{m}$  distances. Increase in *ETRs* at narrow bands is due to being very close to the resonance frequency. While wide bands as  $1\text{kHz}$  are suitable for applications at distances less than  $4\mu\text{m}$ , such narrow bands as  $20\text{Hz}$  are useful for those with distances greater than  $4\mu\text{m}$ . *ETR* is almost zero at below  $7364,20\text{kHz}$  and above  $7364,36\text{kHz}$  in the range from  $8\mu\text{m}$  to  $20\mu\text{m}$ , and is zero at below  $7363,00\text{kHz}$  and above  $7365,00\text{kHz}$  in the range from  $0.1\mu\text{m}$  to  $4\mu\text{m}$ . As depicted in Fig. 5.17, another noteworthy feature is that while changes in *ETR* in the range from  $18\mu\text{m}$  to  $20\mu\text{m}$  is as small as  $1.3\%$ , exchange in the *ETR* is a far greater value as  $217\%$ .

Very large *ETR* values are achieved at distances less than  $1\mu\text{m}$ . achieving such high *ETRs* may be due to neglecting viscous damping. Because viscous damping ratio has a remarkable influence on the system's dynamic behavior provided submicron beam dimensions and separation distances are in use. Therefore, effect of viscous damping ratio on *ETR* is investigated for the same beam geometry in the following section.

### **5.3 Effect of Viscous Damping on Energy Transfer between Micromachinable Beams**

In the previous sections, *ETRs* between micro/nano-scale beams are investigated by neglecting viscous damping effect. While viscous damping effect between macro-scale structures are very small owing to large distances between structures and low natural frequencies, it does affect mechanical behavior significantly between micro/nano-scale structures. When viscous effects are not taken into account, as in the previous sections, *ETRs* are found to be large in value at small separation distances. Therefore, in this section, effect of viscous damping on *ETR* is examined for small distances. Alike the previous sections, micromachinable and characterizable beams  $20\mu\text{m}$ -long,  $1\mu\text{m}$ -wide and  $0.34\mu\text{m}$ -thick are deployed. Viscous damping ratios are calculated for 10 distances in the range from  $0.1\mu\text{m}$  to  $2\mu\text{m}$ , and damping coefficients

are calculated with the help of following formulations. When a viscously damped system is subjected to an external force of  $f$ , the equation of motion is;

$$m \frac{\partial^2 x}{\partial t^2} + b_{sys} \frac{\partial x}{\partial t} + kx = f \quad (5.20)$$

where  $m$  is mass,  $b_{sys}$  is viscous damping coefficient,  $k$  is spring constant.  $b_{sys}$  can be found by Eq. (5.21);

$$b_{sys} = \eta_{eff,s} \frac{A}{d} \quad (5.21)$$

where  $\eta_{eff,s}$  is effective viscosity of air,  $A$  is beam-air contact surface area of and  $d$  is separation distance between beams.  $\eta_{eff,s}$  is obtained by Eq. (5.22);

$$\eta_{eff,s} = \frac{\eta_{air}}{1 + 2K_n} \quad (5.22)$$

where  $\eta_{air}$  is viscosity of air,  $K_n$  is Knudsen Number given in Eq. (5.23);

$$K_n = \frac{\lambda_{air}}{d} \quad (5.23)$$

where  $\eta_{air}$  is equal to 0.0000179kg/(m/sec) and  $\lambda_{air}$ , mean free path of air, is equal to  $6.404 \times 10^{-8}$ m.

Towards calculation of viscous damping ratio at 2 $\mu$ m separation of beams, first,  $K_n$  must be retracted from Eq. (5.23) as;

$$K_n = \frac{6.404 \times 10^{-8} m}{2 \times 10^{-6} m} \Rightarrow K_n = 3.202 \times 10^{-2} \quad (5.24)$$

Then,  $\eta_{eff,s}$  is obtained from Eq.(5.22);

$$\eta_{eff,s} = \frac{0.0000179 \text{ kg / (m / sec)}}{1 + 2(0.03202)} \quad (5.25)$$

$$\eta_{eff,s} = 1.68227 \times 10^{-5} \text{ kg / (m / sec)}$$



Next,  $b_{sys}$  is calculated by writing  $\eta_{eff,s}$  in Eq. (5.21);

$$b_{sys} = 1.68227 \times 10^{-5} \text{ kg } /(\text{m} / \text{sec}) * \frac{6.8 \times 10^{-12} \text{ m}^2}{2 \times 10^{-6} \text{ m}} \quad (5.26)$$

$$b_{sys} = 5.71971 \times 10^{-11} (\text{N} \cdot \text{sec}) / \text{m}$$

Herein, when Laplace Transformation is applied to Eq. (5.20) with all initial conditionals being zero, it can be rewritten as given in Eq. (5.27);

$$ms^2 X(s) + b_{sys} s X(s) + k X(s) = F(s) \quad (5.27)$$

$X(s)$  is left alone;

$$X(s) = \frac{1}{ms^2 + b_{sys} s + k} F(s) \quad (5.28)$$

After Eq. (5.28) is put in bracket by  $m$ ;

$$X(s) = \frac{1}{m \left( s^2 + \frac{b_{sys}}{m} s + \frac{k}{m} \right)} F(s) \quad (5.29)$$

Equation (5.28) is rewritten as in Eq. (5.30);

$$X(s) = \frac{F(s)}{m} \cdot \frac{1}{s^2 + 2\zeta\omega_n s + \omega_n^2} \quad (5.30)$$

By comparison of Eq. (5.29) and Eq. (5.30);

$$2\zeta\omega_n = \frac{b_{sys}}{m} \quad \text{and} \quad \omega_n = \sqrt{\frac{k}{m}} \quad (5.31)$$

where  $\zeta$ , damping ratio, is equal to ;

$$\zeta = \frac{b_{sys}}{2\omega_n m} \quad (5.32)$$

where  $\omega_n$  is known to be 46197087rad/sec (7352,495kHz) from Table 5.9,  $m$  is calculated as  $0.15844 \times 10^{-13}$ kg, and  $b_{sys}$  from Eq. (5.26) is  $5.71971 \times 10^{-11} (\text{N} \cdot \text{sec}) / \text{m}$ . Hence,  $\zeta$  from Eq. (5.32) at 2 $\mu$ m distance becomes;

$$\zeta = \frac{5.71971 \times 10^{-11}}{2 * 46197087 * 0.15844 \times 10^{-13}} \quad (5.33)$$

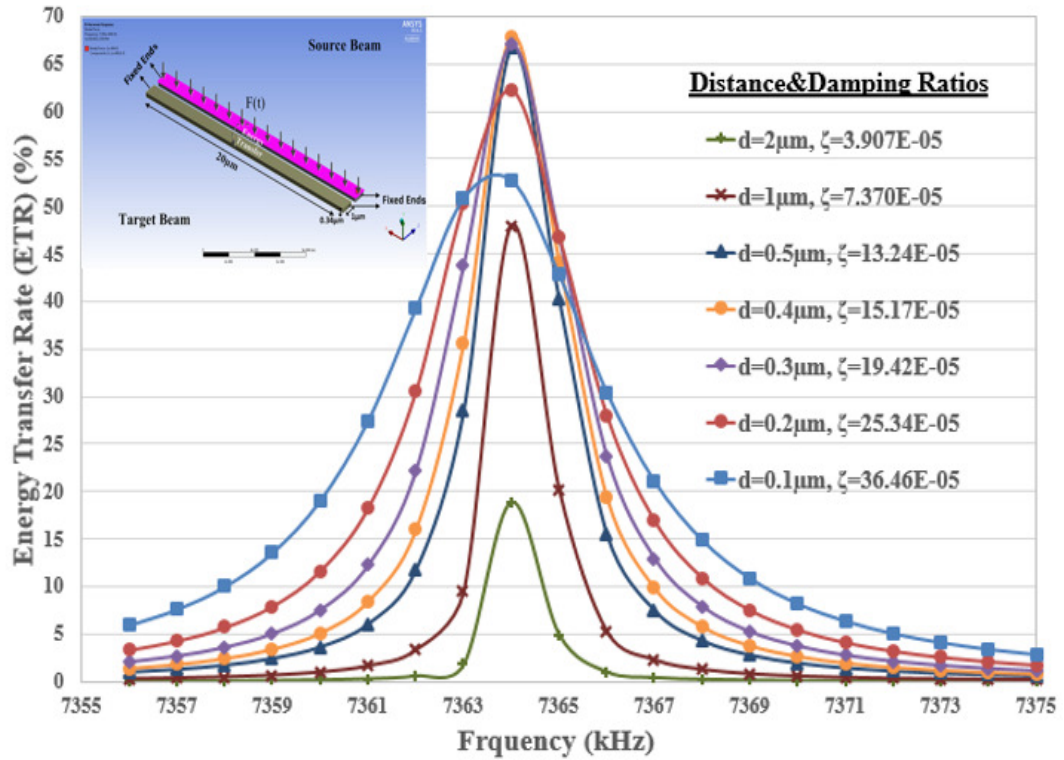
$$\zeta = 3.9072 \times 10^{-5}$$

Then, viscous damping ratios are calculated for the other distances similarly, results are given in Table 5.10.

**Table 5.10** : Viscous damping ratios for various separation distances.

Distance (d), (μm)	Knudsen Number (K <sub>n</sub> )	Effective Viscosity of Air (η <sub>eff, s</sub> ), Kg/(m.sec)	Viscous Damping Coefficient (b <sub>sys</sub> ), (N.sec)/m	Damping Ratio (ζ )
2	0,03202	1,68227E-05	0,571971E-10	3,90719E-05
1	0,06404	1,58677E-05	1,079E-10	7,37077E-05
<b>0,50</b>	0,12808	1,42498E-05	1,93797E-10	13,2385E-05
<b>0,45</b>	0,14231	1,39341E-05	2,10559E-10	14,3835E-05
<b>0,40</b>	0,16010	1,35586E-05	2,30495E-10	15,7454E-05
<b>0,35</b>	0,18297	1,31045E-05	2,54602E-10	17,3921E-05
<b>0,30</b>	0,21347	1,25444E-05	2,84339E-10	19,4235E-05
<b>0,25</b>	0,25616	1,18361E-05	3,21942E-10	21,9922E-05
<b>0,20</b>	0,32020	1,0912E-05	3,71007E-10	25,3439E-05
<b>0,10</b>	0,64040	0,784812E-05	5,33672E-10	36,4557E-05

As seen in Table 5.10, when the distance between the beams decreases, viscous damping ratios increase. While it is  $0.3907 \times 10^{-4}$  at  $2 \mu\text{m}$ , it increases up to  $3.646 \times 10^{-4}$  at  $0.1 \mu\text{m}$  distance. Since viscous damping ratios increase with the decreasing distance, its effect on the *ETR* will increase. After viscous damping ratios are found for various distances, *ETRs* are updated by performing simulations for each calculated viscous damping ratio. While obtained *ETRs* are partially presented in Fig. 5.18, both deflection and *ETR* values are provided in full in Appendix F.



**Figure 5.18 :** Spectral *ETR* response for micromachinable and characterizable beams at various viscous damping caused by various separation distances.

As can be seen in Fig. 5.18, although *ETRs* are observed to increase as separation distance decreases from  $2\mu\text{m}$  down to  $0.4\mu\text{m}$ , they start to decrease for distances smaller than  $0.4\mu\text{m}$ , indicating its maximum at  $0.4\mu\text{m}$  at on-resonant frequencies. Hence, we can consider  $0.4\mu\text{m}$  as the ideal distance within resonance region. On the other hand, change in *ETR* is different at frequency bands below  $7363\text{kHz}$  and above  $7366\text{kHz}$ . At these off-resonant frequency bands, *ETRs* increase regularly with the decreasing distances. Results of simulations with neglected viscous damping are compared to those with calculated viscous damping in order to understand effect of damping on *ETR* at micro/nano-scale beams. Results indicate that effect of disagreement between neglected and manually calculated viscous damping ratios on *ETR* is highest at  $0.1\mu\text{m}$  distance, and that it decays with increasing distance. Having figured out significance of viscous damping ratio on *ETR*, and the fact that its accurate calculation theoretically can not be guaranteed, experimental characterization of viscous damping as future work of this study will play an important role for in-depth understanding of the concept.

## 5.4 Summary

In this chapter, Energy Transfer Rates (ETR) are studied numerically in various beam distances for two different cases where viscous damping ratios are first neglected and, then considered. Initially, ETR values are studied in a band about resonance frequency for two cross-sectional geometries, namely, square and rectangular shapes, at two-settlement options as in-plane and out-of-plane alignments, and for several beam geometries. Then, ETR depending on the distance between beams with rectangular cross-section at in-plane alignment is examined under the influence of viscous damping.

First, *ETR* values between 20 $\mu\text{m}$ -long beams with  $2\times 2\mu\text{m}^2$  square cross-section at out-of-plane alignment are investigated. It shows an irregular behavior depending on the distance between beams. There exist two reasons underneath the concept. The first reason is that distances constantly change when beams are placed out-of-plane directions vibrate towards each other. The second reason is the use of square cross-sectioned beams, where natural frequencies in both directions become equal. The latter situation adversely affects the energy transferred from the source beam to the target beam. Therefore, ETR between beams with square cross-sectional area at in-plane alignment is investigated between 40920kHz and 40940kHz. When distance is decreased from 10 $\mu\text{m}$  to 0.1 $\mu\text{m}$ , ETR values show a steady increase, but these values are even insufficient at a very small distance about 0.1 $\mu\text{m}$ .

Second, energy transfer between beams having smaller geometries is investigated to extend *ETR* levels. Thus, beam sizes are reduced by three-folds, and change in *ETR* values depending on the distance are examined. *ETR* is slightly less compared to the energy transfer between the larger size beams. After their examination in the vertical direction, beam *ETRs* are investigated in the horizontal direction as well. Nevertheless, a regular change in *ETR* are not observed with the distance change. The cause of these disorders are thought to arise from the use of square-section beams, where natural frequencies of the beams become equal in both transverse directions. Hence, target beam may be adversely affected in energy transfer with *MRA* due to use of beams with identical natural frequencies in both directions causing coupling at inter-directional resonance.

Then, *ETR* are studied by use of beams with rectangular cross-sections instead of square cross-section and *ETR* values increase meaningfully both in vertical and transverse directions with decreasing distance. *ETR* values in the vertical direction are found to be identical with those in the transverse direction. The conflict of the natural frequencies in both directions is prevented by use of beams with rectangular cross-section instead of square cross-sections. Thus, use of beams with rectangular cross-section provides two important benefits. The first advantage is that *ETR* values become equal in both directions, and they change regularly as a function of the distance. The second advantage is that *ETR* values get larger. Another remarkable aspect of this section is that shift in the resonance frequency of the system takes place for distances less than 430nm. Such an interesting effect is thought to be caused by the change in the damping ratio in very small distances, or by quick return of acoustic waves hitting the target beam since source and target beams are very close, or by interaction due to such surface molecular forces as Van der Waals or Casimir, or a combination of those. The results obtained in this section show that beam use with rectangular cross-section is important. Then, *ETR* between beams 20 $\mu\text{m}$ -long, 1 $\mu\text{m}$ -wide and 0.34 $\mu\text{m}$ -thick at in-plane alignment are investigated. It is found that *ETRs* in the vertical direction change in a regular manner with distance, and the transfer rates are high. When *ETR* in transverse direction is studied, identical levels of transfer rates comparable to those in the vertical direction are observed. Relatively very large *ETRs* are achieved particularly at distances less than 1 $\mu\text{m}$ , which is attributed to neglected value of viscous damping ratios. However, influence of viscous damping on the system performance becomes significant at small separation distances. Thus, viscous damping must be considered at submicron distances for correct characterization. Towards the goal, viscous damping is considered, and viscous damping ratios are calculated for separation distances between 0.1 $\mu\text{m}$  and 2 $\mu\text{m}$ . Results show that when the distance decreases down until 0.4 $\mu\text{m}$ , *ETR* increases. However, it start to decrease distances smaller than 0.4 $\mu\text{m}$ . In other words, an ideal maximum is achieved at 0.4 $\mu\text{m}$  distance. While the largest effect is obtained at 0.1 $\mu\text{m}$ , the smallest effect is observed at 2 $\mu\text{m}$  distance when viscous damping is not neglected.



## 6. CONCLUSION

In this thesis, a novel technique for non-contact motion and energy transfer between micro/nano-scale doubly-clamped cantilever beams at high efficiency via Mechanical Resonance Absorption (*MRA*) is presented. In order to characterize quality of the transfer, resonating beam dimensions and distances, in-plane and out-of-plane transmission directions, and effect of damping by the environment are comprehensively investigated. In addition, fields of application in micro/nano-scale structures, such as remote actuation and selective resonance are targeted by achieving the regular relationship between energy transfer values and distance changes. *ETR* values investigated for various distances, geometries and position, and results obtained by the analysis are presented in this thesis report.

In the first chapter, brief information on the aim, scope and solution steps of the study is given and such previous studies associated with the thesis topic as Micro-Electro-Mechanical Systems (MEMS), micro/nano-scale vibration, Surface Acoustic Waves (SAW), motion and energy transfer and Mechanical Resonance Absorption (*MRA*) referred in literature are investigated. The movement and energy transfer based on Mechanical Resonance Absorption (*MRA*) observed in human and animal hearing mechanisms are also mentioned. In biological hearing, cochlear behaves as a frequency encoding mechanism by decomposing the complex frequency band of sound waves.

In the second chapter, Bending Equation of Euler Bernoulli, Rayleigh and Timoshenko Beam Theories are discussed first. Then, vibration equations are described for single and multi-degrees of freedom systems and derivation of analytical formulations required for the calculation of natural frequencies and bending vibrations in beams are shown.  $\beta nL$  values used in the analytical calculation of natural frequencies are listed for various beam boundary conditions.

In the third chapter, Finite Element Analysis (FEA) is introduced and common element types used in FEA are mentioned shortly. Acoustic Fluid-Structure Coupling and the

expression of acoustic waves in FEA are presented towards investigation of numerical mechanical energy transfer interaction between doubly-clamped beams via *MRA*.

Then, acoustic element types are defined such that air will resemble acoustic properties in the commercial FEM analysis software at hand, namely ANSYS (ANSYS Inc., USA). Later, necessary environment characteristics for the element types are also summarized. Finally, the absorbing layer (Perfectly Matched Layers, PML) behaving as an infinite medium of modeled air environment in order to prevent back-reflection by absorption of acoustic waves created by the target beam are described.

In the fourth chapter, initially, such concepts as representation of the cross-section of beam geometries used in the investigation of motion and energy transfer between the beams, relative positioning, the direction of the applied dynamic force, and representation of the source and target beams are studied. Then, the interaction model, material properties, acoustic element types in air, and the program codes required to define the fluid-structure interaction between air and the beams in FEA software are described.

In the fifth chapter, Energy Transfer Rates (*ETR*) are studied numerically in various beam distances for two different cases where first, viscous damping ratio is neglected and, then considered. At first, *ETR* values are studied in a band about resonance frequency for two cross-sectional geometries, namely, square and rectangular shapes, at two-settlement options as in-plane and out-of-plane alignments, and for several beam geometries. In the second half, *ETR* values depending on the distance between the beams with rectangular cross-section at in-plane alignment are examined under the influence of viscous damping.

To be specific, first, *ETR* values between 20 $\mu\text{m}$ -long beams with 2 $\times$ 2 $\mu\text{m}^2$  square cross-section at out-of-plane alignment are investigated. While there is almost no energy transition from source beam to target beam at off-resonant band, significant is observed at on-resonant frequencies, but it shows an irregular behavior depending on the distance between beams. There exist two reasons underneath the concept. The first reason is that distances constantly change when beams are placed out-of-plane directions vibrate towards each other. The second reason is the use of square cross-sectioned beams, where natural frequencies in both directions become equal. The latter situation adversely affects the energy transferred from the source beam to the target



beam. Therefore, *ETR* between beams with square cross-sectional area at in-plane alignment is investigated between 40920kHz and 40940kHz. While energy transfer between beams is not observed at off-resonant frequencies, efficient energy transfer at on-resonant frequencies takes place. When distance is decreased from 10 $\mu\text{m}$  to 0.1 $\mu\text{m}$ , *ETR* values show a steady increase, but these values are even insufficient at a very small distance about 0.1 $\mu\text{m}$ .

Second, energy transfer between beams having smaller geometries is investigated to extend *ETR* levels. Thus, beam sizes are reduced by three-folds, and change in *ETR* values depending on the distance are examined. *ETR* is slightly less compared to the energy transfer between the larger size beams. After their examination in the vertical direction, beam *ETRs* are investigated in the horizontal direction as well. Nevertheless, a regular change in *ETR* are not observed with the distance change. The cause of these disorders are thought to arise from the use of square-section beams, where natural frequencies of the beams become equal in both transverse directions. Hence, target beam may be adversely affected in energy transfer with *MRA* due to use of beams with identical natural frequencies in both directions causing coupling at inter-directional resonance.

Afterwards, in order to eliminate irregularities existing in the square cross-section, utilization of beams with rectangular cross-sections are considered. *ETR* values increase meaningfully both in vertical and transverse directions with decreasing distance. *ETR* values in the vertical direction are found to be identical with those in the transverse direction. The conflict of the natural frequencies in both directions is prevented by use of beams with rectangular cross-section instead of square cross-sections. Thus, use of beams with rectangular cross-section provides two important benefits. The first advantage is that *ETR* values become equal in both directions, and they change regularly as a function of the distance. The second advantage is that *ETR* values get larger. Another remarkable aspect of this section is that shift in the resonance frequency of the system takes place for distances less than 430nm. Such an interesting effect is thought to be caused by the change in the damping ratio in very small distances, or by quick return of acoustic waves hitting the target beam since source and target beams are very close, or by interaction due to such surface molecular forces as Van der Waals or Casimir, or a combination of those. The results obtained in this section show that beam use with rectangular cross-section is important.

Then, *ETR* between beams 20 $\mu\text{m}$ -long, 1 $\mu\text{m}$ -wide and 0.34 $\mu\text{m}$ -thick at in-plane alignment are investigated. It is found that *ETRs* in the vertical direction change in a regular manner with distance, and the transfer rates are high. When *ETR* in transverse direction is studied, identical levels of transfer rates comparable to those in the vertical direction are observed. Relatively very large *ETRs* are achieved particularly at distances less than 1 $\mu\text{m}$ , which is attributed to neglected value of viscous damping ratios. However, influence of viscous damping on the system performance becomes significant at small separation distances. Thus, viscous damping must be considered at submicron distances for correct characterization. Towards the goal, viscous damping is considered, and viscous damping ratios are calculated for separation distances of 0.1 $\mu\text{m}$ , 0.2 $\mu\text{m}$ , 0.25 $\mu\text{m}$ , 0.3 $\mu\text{m}$ , 0.35 $\mu\text{m}$ , 0.4 $\mu\text{m}$ , 0.45 $\mu\text{m}$ , 0.5 $\mu\text{m}$ , 1 $\mu\text{m}$ , and 2 $\mu\text{m}$ . Results show that when the distance decreases down until 0.4 $\mu\text{m}$ , *ETR* increases. However, it start to decrease distances smaller than 0.4 $\mu\text{m}$ . In other words, an ideal maximum is achieved at 0.4 $\mu\text{m}$  distance. While the largest effect is obtained at 0.1 $\mu\text{m}$ , the smallest effect is observed at 2 $\mu\text{m}$  distance when viscous damping is not neglected. As a result, in-plane orientation between beams should be used in order to establish a stable energy transfer relation with the distance. *ETR* increases slightly when beam dimensions are reduced by three-folds. Natural frequency overlap can be prevented by use of rectangular cross-sectioned beams instead of the square-sectioned ones. Increasing the chord length provides higher *ETR* and possibility to work at lower frequencies. The viscous damping effect has a significant impact on energy transfer at small distances. Such micro/nano-scale structure beam designs with rectangular cross-sections at in-plane alignment can create application fields in remote actuation by selective resonance with their stable relationship between energy transfer and distance. In the future, numerical studies are to be experimentally confirmed. In the experimental section, first, an electrostatically driven single beam will be micromachined on silicon wafers, and dynamic mechanical behavior of the beam will be examined at on and off-resonant frequencies. Next, doubly-clamped beams of two located at various distances will be produced again on silicon wafers, and characterization of *ETR* via *MRA* as a function of the distance will be conducted. The effect of viscous damping ratio on micro/nano-scale structures will be investigated as well. In the mechanical characterization, ODC-based sensors developed already in our laboratory will be embedded into the test devices for precise and real-time *ETR*

measurements. Then, deviation between the numerical and experimental results, if any, and its sources will be understood. Finally, we plan to investigate effect of ambient environment parameters on the viscous damping, and indirectly on the energy transfer.



## REFERENCES

- [1] **Feynman, R. P.** (1992). There's plenty of room at the bottom, the American Physical Society Meeting in Pasadena CA, USA, (1959); (re-print) *Journal of Microelectromechanical Systems*, 1, 60-66.
- [2] **Kaplan, H., Dolen, M.** (2003). *Mikro-Elektro-Mekanik-Sistemler (MEMS): Üretim teknikleri*, 11. Ulusal Makina Teorisi Sempozyumu, Gazi Üniversitesi, Ankara, Turkey.
- [3] **Weinstein, D.** (2007). Bhave, S.A., Mechanical coupling of 2D resonator arrays for MEMS filter applications, *IEEE Int. Conf. on Micro Electro Mechanical Systems (MEMS)*, USA, 1362-1365.
- [4] **Jiang, C., Chen, B., Li, J., Zhu, K.** (2011). Mass spectrometry based on a coupled Cooper-pair box and nanomechanical resonator system, *Nanoscale Research Letters*, 6, 570-577.
- [5] **Kaajakari, V., Mattila, T., Lipsanen, A., Oja, A.** (2005). Nonlinear mechanical effects in silicon longitudinal mode beam resonators, *Sensors And Actuators A: Physical*, 120(1), 64-70.
- [6] **Ishino, T., Makita, S., Tanigawa, H., Suzuki, K.** (2009). Characteristics of three-dimensional resonant vibration in a MEMS silicon beam resonator, *IEEJ Transactions on Sensors and Micromachines*, 129, 289-294.
- [7] **Baskaran, R., Garten, M., Turner, K.** (2002). Experimental characterization of an electrostatically coupled oscillator MEM filter, *SEM Annual Conference and Exposition*, Milwaukee, Wisconsin, USA.
- [8] **Zhu, R., Wang, D., Zhou, Z., Ye, X.** (2006). Design of a hybrid micro/nano cantilever-based resonant sensor and its fabrication method, *IEEE Int. Conf. on Nano/Micro Engineered and Molecular Systems*, Zhuhai, China, 18-21.
- [9] **Zhang, W., Turner, K. L.** (2004). Mass sensor based on parametric resonance, *Solid-State Sensor, Actuator and Microsystems Workshop*, Hilton Head Island, South Carolina, USA, 49-52.
- [10] **Yu, H., Zhang, W.W., Lei, S. Y., Lu, L. B., Sun, C., Huang, Q. A.** (2012). Study on vibration behavior of doubly clamped silicon nanowires by molecular dynamics, *Journal of Nanomaterials*, 342329.
- [11] **Murmu, T., Pradhan, S.C.** (2009). Small-scale effect on the vibration of nonuniform nanocantilever based on nonlocal elasticity theory, *Physica E*, 41, 1451-1456.
- [12] **Murmu, T., Pradhan, S.C.** (2009). Thermo-mechanical vibration of a single-walled carbon nanotube embedded in an elastic medium based on nonlocal elasticity theory, *Computational Materials Science*, 46, 854–859.

- [13] **Murmu, T., Pradhan, S.C.** (2009). Small-scale effect on the free in-plane vibration of nanoplates by nonlocal continuum model, *Physica E*, 41, 1628-1633.
- [14] **Murmu, T., Pradhan, S.C.** (2009). Vibration analysis of nano-single-layered graphene sheets embedded in elastic medium based on nonlocal elasticity theory, *Journal of Applied Physics*, 105, 064319.
- [15] **Wang, L.** (2009). Vibration and instability analysis of tubular nano- and micro-beams conveying fluid using nonlocal elastic theory, *Physica E*, 41, 1835-1840.
- [16] **Napoli, M., Zhang, W., Turner, K., Bamieh, B.** (2003). Dynamics of mechanically and electrostatically coupled microcantilevers, the 12th Int. Conf. on Solid State Sensors, Actuators And Microsystems, Boston, USA, 1088-1091.
- [17] **Hamidon, M.N., Skarda, V., White, N.M., Krispel, F., Krempl, P., Binhack, M., Buff, W.** (2005). Fabrication of high temperature surface acoustic wave devices for sensor applications, *Sensors and Actuators*, 403-407.
- [18] **Springer, A., Weigel, R., Pohl, A., Seifert, F.** (1999). Wireless identification and sensing using surface acoustic wave devices, *Mechatronics*, 9, 745-756.
- [19] **Elmazria, O., Benedic, F., El Hakiki, M., Moubchir, H., Assouar, M.B., Silva, F.** (2006). Nanocrystalline diamond films for surface acoustic wave devices, *Diamond and Related Materials*, 15, 193-198.
- [20] **Wohltjen, H. Dessy, R.** (1979). Surface acoustic wave probe for chemical analysis; introduction and instrument description, *Analytical Chemistry*, 51, 1458-1464.
- [21] **Jakubik, W. P.** (2011). Surface acoustic wave-based gas sensors, *Thin Solid Films*, 520, 986-993.
- [22] **Wixforth, A., Kotthaus, J. P.** (1986). Quantum oscillations in the surface-acoustic-wave attenuation caused by a two-dimensional electron system, *Physical Review Letters*, 56, 2104-2106.
- [23] **Welsch, W., Klein, C., Von Schickfus, M., Hunklinger, S.** (1996). Development of a surface acoustic wave immunosensor, *Analytical Chemistry*, 68, 2000-2004.
- [24] **Jakubik, W. P., Urbanczyk, M. W., Kochowski, S., Bodzenta, J.** (2002). Bilayer structure for hydrogen detection in a surface acoustic wave sensor system, *Sensors and Actuators*, 82, 265-271.
- [25] **Hollweg, J.V.** (1997). A simple mechanical model for resonance absorption: the Alfvén resonance, *Journal of Geophysical Research*, 102, 127-137.
- [26] **Powell, D. J., Mould, J., Wojcik, G. L.** (1988). Dielectric and mechanical absorption mechanisms for time and frequency domain transducer modeling, *IEEE Ultrasonic Symposium Proceedings*, Sendai, Japan, 2, 1019-1024.

- [27] **Kerschen, G., Vakakis. A. F., Lee. Y.S., Mcfarland. D. M., Kowtko. J. J., Bergman. L. A.** (2005). Energy transfers in a system of two coupled oscillators with essential nonlinearity: resonance manifold and transient bridging orbits, *Nonlinear Dynamics*, 42, 283–303.
- [28] **Carcaterra, A., Akay. A.** (2007). Theoretical foundations of apparent-damping phenomena and nearly irreversible energy exchange in linear conservative systems, *Acoustical Society of America*, 121(4), 1971-1982.
- [29] **Roveri, N., Carcaterra. A., Akay. A.** (2009). Energy equipartition and frequency distribution in complex attachments, *Acoustical Society of America*, 126(1), 122-128.
- [30] **Roveri, N., Carcaterra. A., Akay. A.** (2009). Vibration absorption using non-dissipative complex attachments with impacts and parametric stiffness, *Acoustical Society of America*, 126(5), 2306-2314.
- [31] **Carcaterra, A., Akay. A., Bernardini C.** (2012). Trapping of vibration energy into a set of resonators: Theory and application to aerospace structures, *Mechanical Systems and Signal Processing*, 26, 1-14.
- [32] **Matheny M. H., Villanueva, L. G., Karabalin, R. B., Sader, J. E., and Roukes, M. L.** (2013). Nonlinear Mode-Coupling in Nanomechanical Systems, *Nano Letters*, 13, 1622–1626.
- [33] **Villanueva, L. G., Karabalin, R. B., Matheny, M. H., Chi, D., Sader, J. E., and Roukes, M. L.** (2013). Nonlinearity in nanomechanical cantilevers, *Physical Review*, 87, 024304.
- [34] **Karabalin, R. B., Villanueva, L. G., Matheny, M. H., Sader, J. E., and Roukes, M. L.** (2012). Stress-Induced Variations in the Stiffness of Micro- and Nano-cantilever Beams, *Physical Review Letters*, 108, 23610.
- [35] **Husain, A., Hone, J., Henk W. Postma, Ch. X. Huang, M. H., Drake, T., Barbic, M. Scherer, A. and Roukes, M. L.** (2013). Nanowire-based very-high-frequency electromechanical resonator, *Applied Physics Letters*, 83, 1240-1242.
- [36] **Feng, J., Ye, X., Esashi, M., and Ono, T.** (2010). Mechanically coupled synchronized resonators for resonant sensing applications, *Journal of Micromechanics and Microengineering*, 20, 115001.
- [37] **Perisanu, S., Barois, T., Poncharal, P., Gaillard, T., Ayari, A., Purcell, S. T. and Vincent, P.** (2011). The mechanical resonances of electrostatically coupled nanocantilevers, *Applied Physics Letters*, 98, 063110.
- [38] **Loizon. P.C.** (1998). Mimicking the human ear, *IEEE Signal Processing Magazine*, 101-130.
- [39] **Meirovitch, L.** (2001). *Fundamentals of Vibrations*, the McGraw-Hill Companies, Inc., New York.
- [40] **Pekoz, Z. Ç.** (2005). Free Vibration Analysis of a Non-Uniform Free-Ended Beam with Weighted Residual Methods, M.Sc. Thesis, Bosphorus University, Turkey.

- [41] **Han, S.** (2001). *Vibration of a Compliant Structure in an Ocean Environment*, Ph.D. Thesis, the State University of New Jersey, USA.
- [42] **Timoshenko, S.,** (1937). *Vibration Problems in Engineering*, D. Van Nostrand Company, Inc., New York, USA.
- [43] **Wang, C. M., Reddy, J. N. and Lee, K. H.** (2000). *Shear Deformable Beams and Plates*, Elsevier Science Ltd., Oxford.
- [44] **Rao, S. S.** (2007). *Vibration of a Continuous systems*, John Wiley and Sons Inc., Hoboken, New Jersey, USA.
- [45] **Liu, G. R., Quek, S. S.** (2003). *The Finite Element Method: A Practical Course*, Elsevier Science Ltd., National University of Singapore, Singapore.
- [46] **Isik, M.** (2008). *Değişken Kesitli Eğri Kirişlerin Titreşimleri*, M.Sc. Thesis, Zonguldak Karaelmas University, Zonguldak.
- [47] **Ergin, A., Bayraktarkatal, E., Unsan, Y.** (2000). *Sonlu Elemanlar Metodu ve Gemi İnşaatı Sektöründeki Uygulamaları*, Yapım Matbaacılık Ltd., Istanbul.
- [48] **Moaveni, S.** (1999). *Finite Element Analysis; Theory and Application with ANSYS*, Prentice Hall Inc., Upper Saddle River, New Jersey, USA.
- [49] **ANSYS, Inc.** (2012). *ANSYS Mechanical APDL Element Reference*, Release 14.5, Southpointe. 275 Technology Drive, Canonsburg, PA 15317, USA.
- [50] **Drozd, M. B.** (2008). *Efficient Finite Element Modelling Of Ultrasound Waves in Elastic Media*, *PhD Thesis*, Imperial College of Science Technology and Medicine University of London, England.



## **APPENDICES**

**APPENDIX A:** Deflection and ETR values for 20 $\mu\text{m}$ -long, 2 $\mu\text{m}$ -wide, and 2 $\mu\text{m}$ -thick beams at out-of-plane alignment under 1nN (nanonewton) dynamic force.

**APPENDIX B:** Deflection and ETR values for 20 $\mu\text{m}$ -long, 2 $\mu\text{m}$ -wide, and 2 $\mu\text{m}$ -thick beams at in-plane alignment under 1nN (nanonewton) dynamic force.

**APPENDIX C:** Deflection and ETR values for 8 $\mu\text{m}$ -long, 0.75 $\mu\text{m}$ -wide, and 0.75 $\mu\text{m}$ -thick beams at in-plane alignment under 1nN (nanonewton) dynamic force.

**APPENDIX D:** Deflection and ETR values for 8 $\mu\text{m}$ -long, 0.75 $\mu\text{m}$ -wide, and 0.34 $\mu\text{m}$ -thick beams at in-plane alignment under 1nN (nanonewton) dynamic force.

**APPENDIX E:** Deflection and ETR values for 20 $\mu\text{m}$ -long, 1 $\mu\text{m}$ -wide, and 0.34 $\mu\text{m}$ -thick beams at in-plane alignment under 1nN and 0.1nN (nanonewton) dynamic force.

**APPENDIX F:** Deflection and ETR values for 20 $\mu\text{m}$ -long, 2 $\mu\text{m}$ -wide, and 2 $\mu\text{m}$ -thick beams at in-plane alignment under 1nN (nanonewton) dynamic force under viscously damped coefficient.

**APPENDIX A:**

*Deflection and ETR values for 20 $\mu$ m-long, 2 $\mu$ m-wide, and 2 $\mu$ m-thick beams at out-of-plane alignment under 1nN (nanonewton) dynamic force.*

**Table A.1 :** Deflection and ETR values at 1 $\mu$ m separation distance.

<b>Frequency (kHz)</b>	<b>Amplitude of First Beam (nm)</b>	<b>Amplitude of Second Beam (nm)</b>	<b>Transfer Rate of Deflection</b>	<b>Percent Transfer Rate of Deflection</b>	<b>Percent Transfer Rate of Energy</b>
40921	0,08777	0,06490	0,74	73,94	54,67
40922	0,09058	0,06927	0,76	76,47	58,48
40923	0,09383	0,07409	0,79	78,96	62,35
40924	0,09766	0,07945	0,81	81,35	66,19
40925	0,10222	0,08545	0,84	83,59	69,88
40926	0,10773	0,09224	0,86	85,62	73,32
40927	0,11447	0,10002	0,87	87,38	76,35
40928	0,12282	0,10903	0,89	88,77	78,81
40929	0,13324	0,11961	0,90	89,77	80,59
40930	0,14638	0,13221	0,90	90,32	81,58
40931	0,16307	0,14742	0,90	90,40	81,73
40932	0,18440	0,16598	0,90	90,01	81,02
40933	0,21161	0,18867	0,89	89,16	79,49
40934	0,24565	0,21589	0,88	87,89	77,24
40935	0,28565	0,24637	0,86	86,25	74,39
40936	0,32549	0,27440	0,84	84,30	71,07
40937	0,35102	0,28828	0,82	82,13	67,45
40938	0,34867	0,27815	0,80	79,77	63,64
40939	0,32149	0,24855	0,77	77,31	59,77
40940	0,28454	0,21282	0,75	74,79	55,94

**Table A.2 :** Deflection and *ETR* values at 2 $\mu$ m separation distance.

<i>Frequency (kHz)</i>	<i>Amplitude of First Beam (nm)</i>	<i>Amplitude of Second Beam (nm)</i>	<i>Transfer Rate of Deflection</i>	<i>Percent Transfer Rate of Deflection</i>	<i>Percent Transfer Rate of Energy</i>
<i>Frequency (kHz)</i>	<i>First Beam Amplitude (nm)</i>	<i>Second Beam Amplitude (nm)</i>	<i>Transfer Rate of Deflection</i>	<i>Transfer Rate (%) of Deflection</i>	<i>Transfer Rate (%) of Energy</i>
40921	0,1115	0,0482	0,43	43,21	18,68
40922	0,1175	0,0531	0,45	45,15	20,38
40923	0,1244	0,0587	0,47	47,21	22,29
40924	0,1324	0,0654	0,49	49,41	24,41
40925	0,1416	0,0732	0,52	51,73	26,76
40926	0,1525	0,0826	0,54	54,18	29,35
40927	0,1657	0,0940	0,57	56,73	32,19
40928	0,1819	0,1080	0,59	59,37	35,25
40929	0,2022	0,1255	0,62	62,06	38,52
40930	0,2281	0,1477	0,65	64,74	41,91
40931	0,2618	0,1763	0,67	67,34	45,34
40932	0,3052	0,2129	0,70	69,76	48,67
40933	0,3581	0,2575	0,72	71,91	51,72
40934	0,4104	0,3023	0,74	73,67	54,27
40935	0,4353	0,3261	0,75	74,92	56,14
40936	0,4121	0,3115	0,76	75,59	57,14
40937	0,3589	0,2714	0,76	75,63	57,19
40938	0,3042	0,2282	0,75	75,02	56,28
40939	0,2594	0,1915	0,74	73,83	54,51
40940	0,2252	0,1624	0,72	72,12	52,01

**Table A.3** : Deflection and *ETR* values at 3 $\mu$ m separation distance.

<i>Frequency (kHz)</i>	<i>Amplitude of First Beam (nm)</i>	<i>Amplitude of Second Beam (nm)</i>	<i>Transfer Rate of Deflection</i>	<i>Percent Transfer Rate of Deflection</i>	<i>Percent Transfer Rate of Energy</i>
40921	0,1424	0,0533	0,37	37,45	14,03
40922	0,1533	0,0607	0,40	39,60	15,68
40923	0,1662	0,0698	0,42	41,97	17,61
40924	0,1818	0,0810	0,45	44,58	19,87
40925	0,2008	0,0953	0,47	47,45	22,52
40926	0,2245	0,1137	0,51	50,62	25,63
40927	0,2549	0,1379	0,54	54,10	29,27
40928	0,2942	0,1703	0,58	57,90	33,52
40929	0,3446	0,2136	0,62	61,97	38,40
40930	0,4046	0,2681	0,66	66,26	43,90
40931	0,4574	0,3230	0,71	70,63	49,88
40932	0,4636	0,3491	0,75	75,30	56,70
40933	0,4194	0,3297	0,79	78,62	61,81
40934	0,3525	0,2874	0,82	81,53	66,48
40935	0,2947	0,2453	0,83	83,23	69,27
40936	0,2623	0,2105	0,80	80,27	64,43
40937	0,2225	0,1828	0,82	82,16	67,49
40938	0,2019	0,1606	0,80	79,55	63,28
40939	0,1873	0,1423	0,76	75,99	57,74
40940	0,1766	0,1269	0,72	71,86	51,64

**Table A.4 :** Deflection and *ETR* values at 4 $\mu$ m separation distance.

<b>Frequency (kHz)</b>	<b>Amplitude of First Beam (nm)</b>	<b>Amplitude of Second Beam (nm)</b>	<b>Transfer Rate of Deflection</b>	<b>Percent Transfer Rate of Deflection</b>	<b>Percent Transfer Rate of Energy</b>
40921	0,1850	0,0793	0,43	42,85	18,36
40922	0,2013	0,0920	0,46	45,71	20,90
40923	0,2195	0,1073	0,49	48,91	23,92
40924	0,2390	0,1254	0,52	52,47	27,53
40925	0,2581	0,1457	0,56	56,44	31,85
40926	0,2736	0,1664	0,61	60,82	36,99
40927	0,2812	0,1845	0,66	65,61	43,04
40928	0,2775	0,1963	0,71	70,73	50,02
40929	0,2632	0,2000	0,76	76,01	57,77
40930	0,2427	0,1969	0,81	81,14	65,83
40931	0,2215	0,1897	0,86	85,65	73,36
40932	0,2032	0,1808	0,89	88,98	79,17
40933	0,1895	0,1716	0,91	90,57	82,03
40934	0,1807	0,1628	0,90	90,13	81,23
40935	0,1760	0,1544	0,88	87,74	76,97
40936	0,1743	0,1461	0,84	83,83	70,28
40937	0,1744	0,1378	0,79	78,98	62,38
40938	0,1751	0,1291	0,74	73,75	54,39
40939	0,1753	0,1201	0,69	68,51	46,94
40940	0,1744	0,1108	0,64	63,53	40,36

**Table A.5** : Deflection and *ETR* values at 5 $\mu$ m separation distance.

<i>Frequency (kHz)</i>	<i>Amplitude of First Beam (nm)</i>	<i>Amplitude of Second Beam (nm)</i>	<i>Transfer Rate of Deflection</i>	<i>Percent Transfer Rate of Deflection</i>	<i>Percent Transfer Rate of Energy</i>
40921	0,1309	0,0553	0,42	42,24	17,84
40922	0,1350	0,0604	0,45	44,70	19,98
40923	0,1390	0,0658	0,47	47,35	22,42
40924	0,1426	0,0716	0,50	50,19	25,19
40925	0,1460	0,0776	0,53	53,18	28,28
40926	0,1491	0,0839	0,56	56,29	31,69
40927	0,1521	0,0904	0,59	59,43	35,32
40928	0,1552	0,0970	0,62	62,47	39,03
40929	0,1588	0,1037	0,65	65,25	42,58
40930	0,1634	0,1104	0,68	67,56	45,65
40931	0,1693	0,1171	0,69	69,21	47,90
40932	0,1769	0,1238	0,70	70,01	49,01
40933	0,1865	0,1303	0,70	69,86	48,81
40934	0,1977	0,1360	0,69	68,80	47,34
40935	0,2097	0,1404	0,67	66,93	44,80
40936	0,2210	0,1424	0,64	64,46	41,55
40937	0,2294	0,1412	0,62	61,57	37,91
40938	0,2329	0,1362	0,58	58,49	34,21
40939	0,2309	0,1278	0,55	55,34	30,63
40940	0,2238	0,1170	0,52	52,25	27,30

**Table A.6 :** Deflection and *ETR* values at 6 $\mu$ m separation distance.

<b>Frequency (kHz)</b>	<b>Amplitude of First Beam (nm)</b>	<b>Amplitude of Second Beam (nm)</b>	<b>Transfer Rate of Deflection</b>	<b>Percent Transfer Rate of Deflection</b>	<b>Percent Transfer Rate of Energy</b>
40921	0,1183	0,0398	0,34	33,63	11,31
40922	0,1238	0,0409	0,33	33,05	10,92
40923	0,1299	0,0418	0,32	32,20	10,37
40924	0,1365	0,0532	0,39	38,97	15,19
40925	0,1439	0,0589	0,41	40,97	16,78
40926	0,1522	0,0655	0,43	43,05	18,53
40927	0,1617	0,0731	0,45	45,19	20,42
40928	0,1723	0,0817	0,47	47,43	22,50
40929	0,1852	0,0916	0,49	49,46	24,46
40930	0,2000	0,1029	0,51	51,45	26,47
40931	0,2173	0,1156	0,53	53,21	28,31
40932	0,2368	0,1294	0,55	54,63	29,85
40933	0,2577	0,1434	0,56	55,65	30,97
40934	0,2773	0,1556	0,56	56,12	31,49
40935	0,2913	0,1633	0,56	56,05	31,42
40936	0,2952	0,1636	0,55	55,43	30,73
40937	0,2816	0,1562	0,55	55,48	30,78
40938	0,2712	0,1432	0,53	52,80	27,88
40939	0,2507	0,1278	0,51	50,97	25,98
40940	0,2297	0,1125	0,49	48,95	23,96

**Table A.7** : Deflection and *ETR* values at 8 $\mu$ m separation distance.

<b>Frequency (kHz)</b>	<b>Amplitude of First Beam (nm)</b>	<b>Amplitude of Second Beam (nm)</b>	<b>Transfer Rate of Deflection</b>	<b>Percent Transfer Rate of Deflection</b>	<b>Percent Transfer Rate of Energy</b>
40921	0,1570	0,0475	0,30	30,25	9,15
40922	0,1686	0,0541	0,32	32,08	10,29
40923	0,1817	0,0619	0,34	34,09	11,62
40924	0,1964	0,0713	0,36	36,31	13,18
40925	0,2128	0,0824	0,39	38,73	15,00
40926	0,2303	0,0953	0,41	41,36	17,11
40927	0,2481	0,1096	0,44	44,19	19,53
40928	0,2641	0,1246	0,47	47,17	22,25
40929	0,2754	0,1383	0,50	50,23	25,23
40930	0,2793	0,1487	0,53	53,23	28,34
40931	0,2748	0,1538	0,56	55,97	31,32
40932	0,2637	0,1535	0,58	58,20	33,87
40933	0,2494	0,1488	0,60	59,66	35,59
40934	0,2350	0,1414	0,60	60,15	36,18
40935	0,2224	0,1326	0,60	59,61	35,53
40936	0,2119	0,1231	0,58	58,10	33,76
40937	0,2034	0,1136	0,56	55,84	31,18
40938	0,1961	0,1041	0,53	53,09	28,18
40939	0,1895	0,0949	0,50	50,08	25,08
40940	0,1830	0,0861	0,47	47,03	22,12



**Table A.8** : Deflection and *ETR* values at 10µm separation distance.

<b>Frequency (kHz)</b>	<b>Amplitude of First Beam (nm)</b>	<b>Amplitude of Second Beam (nm)</b>	<b>Transfer Rate of Deflection</b>	<b>Percent Transfer Rate of Deflection</b>	<b>Percent Transfer Rate of Energy</b>
40921	0,1262	0,0343	0,27	27,19	7,39
40922	0,1320	0,0377	0,29	28,59	8,18
40923	0,1382	0,0416	0,30	30,09	9,06
40924	0,1449	0,0459	0,32	31,69	10,05
40925	0,1521	0,0508	0,33	33,38	11,14
40926	0,1599	0,0562	0,35	35,14	12,35
40927	0,1683	0,0622	0,37	36,95	13,65
40928	0,1776	0,0688	0,39	38,75	15,02
40929	0,1877	0,0760	0,40	40,50	16,40
40930	0,1989	0,0837	0,42	42,10	17,72
40931	0,2110	0,0918	0,43	43,48	18,90
40932	0,2239	0,0997	0,45	44,52	19,82
40933	0,2366	0,1068	0,45	45,15	20,39
40934	0,2478	0,1123	0,45	45,32	20,54
40935	0,2554	0,1149	0,45	44,99	20,24
40936	0,2578	0,1140	0,44	44,21	19,54
40937	0,2540	0,1093	0,43	43,04	18,52
40938	0,2448	0,1018	0,42	41,57	17,28
40939	0,2321	0,0926	0,40	39,90	15,92
40940	0,2178	0,0830	0,38	38,12	14,53

**APPENDIX B:**

*Deflection and ETR values for 20 $\mu$ m-long, 2 $\mu$ m-wide, and 2 $\mu$ m-thick beams at in-plane alignment under 1nN (nanonewton) dynamic force.*

**Table B.1 :** Deflection and ETR values at 0.1 $\mu$ m separation distance.

<b>Frequency (kHz)</b>	<b>Amplitude of First Beam (nm)</b>	<b>Amplitude of Second Beam (nm)</b>	<b>Transfer Rate of Deflection</b>	<b>Percent Transfer Rate of Deflection</b>	<b>Percent Transfer Rate of Energy</b>
40921	0,1312	0,0488	0,37	37,22	13,85
40922	0,1397	0,0548	0,39	39,22	15,38
40923	0,1496	0,0619	0,41	41,40	17,14
40924	0,1611	0,0705	0,44	43,78	19,17
40925	0,1748	0,0810	0,46	46,35	21,48
40926	0,1915	0,0941	0,49	49,13	24,13
40927	0,2122	0,1105	0,52	52,09	27,14
40928	0,2384	0,1317	0,55	55,23	30,51
40929	0,2724	0,1593	0,58	58,49	34,22
40930	0,3165	0,1956	0,62	61,78	38,17
40931	0,3720	0,2417	0,65	64,98	42,22
40932	0,4312	0,2928	0,68	67,89	46,09
40933	0,4667	0,3281	0,70	70,31	49,44
40934	0,4480	0,3226	0,72	72,02	51,86
40935	0,3901	0,2841	0,73	72,83	53,04
40936	0,3288	0,2389	0,73	72,65	52,78
40937	0,2795	0,1998	0,71	71,50	51,12
40938	0,2427	0,1688	0,70	69,53	48,34
40939	0,2156	0,1444	0,67	66,99	44,87
40940	0,1951	0,1250	0,6407	64,0664	41,0451

**Table B.2 :** Deflection and ETR values at 0.5 $\mu$ m separation distance.

<i>Frequency (kHz)</i>	<i>Amplitude of First Beam (nm)</i>	<i>Amplitude of Second Beam (nm)</i>	<i>Transfer Rate of Deflection</i>	<i>Percent Transfer Rate of Deflection</i>	<i>Percent Transfer Rate of Energy</i>
40921	0,1470	0,0448	0,30	30,46	9,28
40922	0,1577	0,0508	0,32	32,22	10,38
40923	0,1701	0,0581	0,34	34,15	11,66
40924	0,1846	0,0669	0,36	36,26	13,15
40925	0,2017	0,0778	0,39	38,56	14,87
40926	0,2219	0,0911	0,41	41,05	16,85
40927	0,2459	0,1075	0,44	43,72	19,12
40928	0,2737	0,1274	0,47	46,55	21,67
40929	0,3043	0,1505	0,49	49,45	24,45
40930	0,3335	0,1746	0,52	52,33	27,39
40931	0,3536	0,1946	0,55	55,03	30,28
40932	0,3559	0,2040	0,57	57,33	32,87
40933	0,3391	0,2001	0,59	59,01	34,83
40934	0,3112	0,1864	0,60	59,88	35,86
40935	0,2815	0,1684	0,60	59,81	35,77
40936	0,2551	0,1500	0,59	58,81	34,59
40937	0,2333	0,1331	0,57	57,03	32,52
40938	0,2158	0,1180	0,55	54,67	29,89
40939	0,2014	0,1046	0,52	51,96	27,00
40940	0,1893	0,0929	0,49	49,09	24,10

**Table B.3** : Deflection and ETR values at 1 $\mu$ m separation distance.

<i>Frequency (kHz)</i>	<i>Amplitude of First Beam (nm)</i>	<i>Amplitude of Second Beam (nm)</i>	<i>Transfer Rate of Deflection</i>	<i>Percent Transfer Rate of Deflection</i>	<i>Percent Transfer Rate of Energy</i>
40921	0,1539	0,0401	0,26	26,06	6,79
40922	0,1649	0,0455	0,28	27,58	7,61
40923	0,1774	0,0519	0,29	29,24	8,55
40924	0,1915	0,0595	0,31	31,05	9,64
40925	0,2072	0,0684	0,33	33,01	10,90
40926	0,2246	0,0789	0,35	35,12	12,33
40927	0,2430	0,0907	0,37	37,35	13,95
40928	0,2612	0,1036	0,40	39,66	15,73
40929	0,2770	0,1162	0,42	41,97	17,61
40930	0,2875	0,1270	0,44	44,17	19,51
40931	0,2904	0,1339	0,46	46,12	21,27
40932	0,2853	0,1359	0,48	47,64	22,70
40933	0,2741	0,1331	0,49	48,57	23,59
40934	0,2601	0,1269	0,49	48,79	23,80
40935	0,2456	0,1186	0,48	48,27	23,30
40936	0,2321	0,1093	0,47	47,08	22,17
40937	0,2199	0,0997	0,45	45,37	20,58
40938	0,2089	0,0904	0,43	43,30	18,74
40939	0,1988	0,0816	0,41	41,03	16,84
40940	0,1893	0,0733	0,39	38,71	14,98

**Table B.4 :** Deflection and ETR values at 2 $\mu$ m separation distance.

<b>Frequency (kHz)</b>	<b>Amplitude of First Beam (nm)</b>	<b>Amplitude of Second Beam (nm)</b>	<b>Transfer Rate of Deflection</b>	<b>Percent Transfer Rate of Deflection</b>	<b>Percent Transfer Rate of Energy</b>
40921	0,1446	0,0281	0,19	19,40	3,76
40922	0,1528	0,0314	0,21	20,54	4,22
40923	0,1616	0,0352	0,22	21,79	4,75
40924	0,1708	0,0395	0,23	23,15	5,36
40925	0,1804	0,0444	0,25	24,62	6,06
40926	0,1901	0,0498	0,26	26,18	6,86
40927	0,1997	0,0556	0,28	27,82	7,74
40928	0,2087	0,0616	0,29	29,50	8,70
40929	0,2169	0,0675	0,31	31,14	9,70
40930	0,2238	0,0731	0,33	32,66	10,67
40931	0,2293	0,0779	0,34	33,95	11,52
40932	0,2335	0,0814	0,35	34,86	12,15
40933	0,2363	0,0834	0,35	35,30	12,46
40934	0,2378	0,0837	0,35	35,19	12,39
40935	0,2378	0,0821	0,35	34,54	11,93
40936	0,2360	0,0789	0,33	33,44	11,18
40937	0,2319	0,0743	0,32	32,05	10,27
40938	0,2257	0,0688	0,30	30,47	9,29
40939	0,2175	0,0627	0,29	28,82	8,30
40940	0,2079	0,0565	0,27	27,16	7,37

**Table B.5** : Deflection and ETR values at 4 $\mu$ m separation distance.

<b>Frequency (kHz)</b>	<b>Amplitude of First Beam (nm)</b>	<b>Amplitude of Second Beam (nm)</b>	<b>Transfer Rate of Deflection</b>	<b>Percent Transfer Rate of Deflection</b>	<b>Percent Transfer Rate of Energy</b>
40921	0,1394	0,1645	1,18	118,01	139,27
40922	0,1473	0,1838	1,25	124,76	155,66
40923	0,1559	0,2060	1,32	132,11	174,52
40924	0,1654	0,2316	1,40	140,06	196,17
40925	0,1756	0,2610	1,49	148,62	220,88
40926	0,1866	0,2945	1,58	157,77	248,91
40927	0,1985	0,3322	1,67	167,39	280,21
40928	0,2109	0,3739	1,77	177,29	314,32
40929	0,2237	0,4185	1,87	187,11	350,12
40930	0,2362	0,4639	1,96	196,40	385,72
40931	0,2478	0,5066	2,04	204,49	418,17
40932	0,2572	0,5419	2,11	210,72	444,03
40933	0,2633	0,5645	2,14	214,42	459,77
40934	0,2650	0,5702	2,15	215,18	463,03
40935	0,2620	0,5578	2,13	212,90	453,25
40936	0,2548	0,5295	2,08	207,84	431,97
40937	0,2444	0,4903	2,01	200,57	402,28
40938	0,2322	0,4453	1,92	191,79	367,82
40939	0,2192	0,3993	1,82	182,16	331,83
40940	0,2062	0,3551	1,72	172,23	296,65

**Table B.6 :** Deflection and ETR values at 5 $\mu$ m separation distance.

<i>Frequency (kHz)</i>	<i>Amplitude of First Beam (nm)</i>	<i>Amplitude of Second Beam (nm)</i>	<i>Transfer Rate of Deflection</i>	<i>Percent Transfer Rate of Deflection</i>	<i>Percent Transfer Rate of Energy</i>
40921	0,1422	0,0125	0,09	8,75	0,77
40922	0,1508	0,0140	0,09	9,27	0,86
40923	0,1603	0,0158	0,10	9,83	0,97
40924	0,1708	0,0178	0,10	10,44	1,09
40925	0,1823	0,0202	0,11	11,10	1,23
40926	0,1948	0,0230	0,12	11,82	1,40
40927	0,2084	0,0262	0,13	12,58	1,58
40928	0,2228	0,0298	0,13	13,38	1,79
40929	0,2376	0,0337	0,14	14,18	2,01
40930	0,2522	0,0377	0,15	14,96	2,24
40931	0,2653	0,0415	0,16	15,66	2,45
40932	0,2757	0,0447	0,16	16,22	2,63
40933	0,2819	0,0468	0,17	16,59	2,75
40934	0,2830	0,0473	0,17	16,71	2,79
40935	0,2788	0,0462	0,17	16,58	2,75
40936	0,2702	0,0438	0,16	16,20	2,63
40937	0,2585	0,0404	0,16	15,63	2,44
40938	0,2450	0,0366	0,15	14,93	2,23
40939	0,2308	0,0327	0,14	14,15	2,00
40940	0,2166	0,0289	0,13	13,35	1,78

**Table B.7** : Deflection and ETR values at 10 $\mu$ m separation distance.

<b>Frequency (kHz)</b>	<b>Amplitude of First Beam (nm)</b>	<b>Amplitude of Second Beam (nm)</b>	<b>Transfer Rate of Deflection</b>	<b>Percent Transfer Rate of Deflection</b>	<b>Percent Transfer Rate of Energy</b>
40921	0,140	0,002	0,018	1,782	0,032
40922	0,148	0,003	0,019	1,886	0,036
40923	0,157	0,003	0,020	1,999	0,040
40924	0,167	0,004	0,021	2,122	0,045
40925	0,178	0,004	0,023	2,255	0,051
40926	0,189	0,005	0,024	2,398	0,058
40927	0,202	0,005	0,025	2,549	0,065
40928	0,215	0,006	0,027	2,706	0,073
40929	0,229	0,007	0,029	2,863	0,082
40930	0,242	0,007	0,030	3,013	0,091
40931	0,254	0,008	0,031	3,146	0,099
40932	0,264	0,009	0,033	3,252	0,106
40933	0,271	0,009	0,033	3,319	0,110
40934	0,274	0,009	0,033	3,339	0,111
40935	0,272	0,009	0,033	3,309	0,109
40936	0,267	0,009	0,032	3,233	0,105
40937	0,258	0,008	0,031	3,120	0,097
40938	0,246	0,007	0,030	2,981	0,089
40939	0,233	0,007	0,028	2,828	0,080
40940	0,220	0,006	0,027	2,671	0,071



**APPENDIX C:**

*Deflection and ETR values at Y direction for 8 $\mu$ m-long, 0.75 $\mu$ m-wide, and 0.75 $\mu$ m-thick beams at in-plane alignment under 1nN (nanonewton) dynamic force.*

**Table C.1 :** Deflection and ETR values at 0.2 $\mu$ m separation distance.

<b>Frequency (kHz)</b>	<b>Amplitude of First Beam (nm)</b>	<b>Amplitude of Second Beam (nm)</b>	<b>Transfer Rate of Deflection</b>	<b>Percent Transfer Rate of Deflection</b>	<b>Percent Transfer Rate of Energy</b>
96480	0,1571	0,0229	0,15	14,59	2,13
96490	0,1734	0,0280	0,16	16,16	2,61
96500	0,1933	0,0350	0,18	18,10	3,28
96510	0,2182	0,0448	0,21	20,52	4,21
96520	0,2504	0,0592	0,24	23,62	5,58
96530	0,2936	0,0814	0,28	27,73	7,69
96540	0,3549	0,1186	0,33	33,42	11,17
96550	0,4509	0,1876	0,42	41,61	17,32
96560	0,6334	0,3397	0,54	53,63	28,76
96570	1,1138	0,7752	0,70	69,60	48,44
96580	1,1285	0,9101	0,81	80,65	65,04
96590	0,6072	0,4421	0,73	72,80	53,00
96600	0,4531	0,2558	0,56	56,45	31,87
96610	0,3744	0,1628	0,43	43,49	18,92
96620	0,3178	0,1103	0,35	34,69	12,04
96630	0,2738	0,0784	0,29	28,62	8,19
96640	0,2390	0,0580	0,24	24,26	5,89
96650	0,2112	0,0444	0,21	21,02	4,42
96660	0,1887	0,0349	0,19	18,52	3,43
96670	0,1702	0,0281	0,17	16,54	2,74

**Table C.2 : Deflection and ETR values at 0.5 $\mu$ m separation distance.**

<b>Frequency (kHz)</b>	<b>Amplitude of First Beam (nm)</b>	<b>Amplitude of Second Beam (nm)</b>	<b>Transfer Rate of Deflection</b>	<b>Percent Transfer Rate of Deflection</b>	<b>Percent Transfer Rate of Energy</b>
96480	0,1607	0,0149	0,09	9,30	0,86
96490	0,1781	0,0183	0,10	10,30	1,06
96500	0,1998	0,0230	0,12	11,53	1,33
96510	0,2275	0,0298	0,13	13,09	1,71
96520	0,2638	0,0399	0,15	15,12	2,29
96530	0,3137	0,0559	0,18	17,83	3,18
96540	0,3863	0,0835	0,22	21,62	4,68
96550	0,5005	0,1358	0,27	27,13	7,36
96560	0,6961	0,2456	0,35	35,28	12,44
96570	0,9637	0,4437	0,46	46,04	21,20
96580	0,8689	0,4568	0,53	52,57	27,63
96590	0,6570	0,3031	0,46	46,14	21,29
96600	0,5248	0,1849	0,35	35,24	12,42
96610	0,4252	0,1153	0,27	27,12	7,36
96620	0,3497	0,0758	0,22	21,67	4,70
96630	0,2936	0,0526	0,18	17,92	3,21
96640	0,2515	0,0383	0,15	15,23	2,32
96650	0,2193	0,0290	0,13	13,23	1,75
96660	0,1941	0,0227	0,12	11,68	1,36
96670	0,1739	0,0182	0,10	10,46	1,09

**Table C.3 :** Deflection and ETR values at 1 $\mu$ m separation distance.

<i>Frequency (kHz)</i>	<i>Amplitude of First Beam (nm)</i>	<i>Amplitude of Second Beam (nm)</i>	<i>Transfer Rate of Deflection</i>	<i>Percent Transfer Rate of Deflection</i>	<i>Percent Transfer Rate of Energy</i>
96480	0,1605	0,0092	0,06	5,74	0,33
96490	0,1777	0,0113	0,06	6,35	0,40
96500	0,1990	0,0141	0,07	7,10	0,50
96510	0,2258	0,0182	0,08	8,05	0,65
96520	0,2605	0,0242	0,09	9,30	0,86
96530	0,3068	0,0337	0,11	10,97	1,20
96540	0,3705	0,0493	0,13	13,32	1,77
96550	0,4602	0,0769	0,17	16,71	2,79
96560	0,5844	0,1262	0,22	21,59	4,66
96570	0,7373	0,2012	0,27	27,29	7,45
96580	0,8621	0,2539	0,29	29,45	8,68
96590	0,7845	0,1933	0,25	24,64	6,07
96600	0,6007	0,1124	0,19	18,71	3,50
96610	0,4595	0,0668	0,15	14,54	2,11
96620	0,3657	0,0429	0,12	11,72	1,37
96630	0,3018	0,0294	0,10	9,74	0,95
96640	0,2561	0,0213	0,08	8,30	0,69
96650	0,2221	0,0160	0,07	7,21	0,52
96660	0,1959	0,0125	0,06	6,37	0,41
96670	0,1751	0,0100	0,06	5,69	0,32

**Table C.4 :** Deflection and ETR values at 2 $\mu$ m separation distance.

<b>Frequency (kHz)</b>	<b>Amplitude of First Beam (nm)</b>	<b>Amplitude of Second Beam (nm)</b>	<b>Transfer Rate of Deflection</b>	<b>Percent Transfer Rate of Deflection</b>	<b>Percent Transfer Rate of Energy</b>
96480	0,1617	0,0003	0,002	0,210	0,000
96490	0,1793	0,0004	0,002	0,219	0,000
96500	0,2011	0,0005	0,002	0,232	0,001
96510	0,2286	0,0006	0,003	0,253	0,001
96520	0,2644	0,0008	0,003	0,285	0,001
96530	0,3126	0,0010	0,003	0,334	0,001
96540	0,3799	0,0015	0,004	0,408	0,002
96550	0,4773	0,0025	0,005	0,514	0,003
96560	0,6184	0,0042	0,007	0,681	0,005
96570	0,7894	0,0078	0,010	0,993	0,010
96580	0,8584	0,0104	0,012	1,212	0,015
96590	0,7315	0,0083	0,011	1,134	0,013
96600	0,5634	0,0054	0,010	0,956	0,009
96610	0,4383	0,0035	0,008	0,800	0,006
96620	0,3530	0,0024	0,007	0,689	0,005
96630	0,2935	0,0018	0,006	0,611	0,004
96640	0,2503	0,0014	0,006	0,556	0,003
96650	0,2178	0,0011	0,005	0,516	0,003
96660	0,1926	0,0009	0,005	0,485	0,002
96670	0,1725	0,0008	0,005	0,461	0,002

*Deflection and ETR values at Z direction for 8 $\mu$ m-long, 0.75 $\mu$ m-wide, and 0.75 $\mu$ m-thick beams at in-plane alignment under 1nN (nanonewton) dynamic force.*

**Table C.5 :** Deflection and ETR values at 0.2 $\mu$ m separation distance.

<b>Frequency (kHz)</b>	<b>Amplitude of First Beam (nm)</b>	<b>Amplitude of Second Beam (nm)</b>	<b>Transfer Rate of Deflection</b>	<b>Percent Transfer Rate of Deflection</b>	<b>Percent Transfer Rate of Energy</b>
96480	0,0055	0,0043	0,77	77,23	59,65
96490	0,0072	0,0057	0,80	79,55	63,28
96500	0,0094	0,0076	0,81	81,40	66,26
96510	0,0116	0,0097	0,84	83,82	70,25
96520	0,0133	0,0116	0,87	86,92	75,56
96530	0,0143	0,0130	0,91	90,77	82,40
96540	0,0152	0,0145	0,95	95,22	90,68
96550	0,0169	0,0168	0,99	99,41	98,83
96560	0,0212	0,0214	1,01	100,94	101,88
96570	0,0326	0,0320	0,98	98,00	96,05
96580	0,0193	0,0300	1,55	155,04	240,36
96590	0,0188	0,0314	1,67	166,92	278,61
96600	0,0235	0,0209	0,89	89,16	79,49
96610	0,0161	0,0087	0,54	53,98	29,14
96620	0,0113	0,0040	0,36	35,64	12,70
96630	0,0084	0,0021	0,25	25,10	6,30
96640	0,0066	0,0012	0,18	17,81	3,17
96650	0,0053	0,0007	0,13	12,67	1,61
96660	0,0044	0,0004	0,09	9,14	0,83
96670	0,0037	0,0003	0,09	8,62	0,74

**Table C.6 :** Deflection and ETR values at 0.5 $\mu$ m separation distance.

<b>Frequency (kHz)</b>	<b>Amplitude of First Beam (nm)</b>	<b>Amplitude of Second Beam (nm)</b>	<b>Transfer Rate of Deflection</b>	<b>Percent Transfer Rate of Deflection</b>	<b>Percent Transfer Rate of Energy</b>
96480	0,0024	0,0020	0,86	85,76	73,55
96490	0,0027	0,0025	0,92	92,02	84,67
96500	0,0032	0,0031	0,99	99,48	98,96
96510	0,0037	0,0040	1,09	108,52	117,77
96520	0,0045	0,0053	1,20	119,59	143,02
96530	0,0055	0,0074	1,33	133,11	177,19
96540	0,0072	0,0108	1,49	149,03	222,10
96550	0,0103	0,0170	1,65	165,41	273,59
96560	0,0170	0,0299	1,76	175,93	309,51
96570	0,0318	0,0540	1,70	169,71	288,00
96580	0,0462	0,0649	1,40	140,49	197,38
96590	0,0597	0,0638	1,07	106,93	114,35
96600	0,0321	0,0299	0,93	93,34	87,13
96610	0,0177	0,0145	0,82	81,81	66,94
96620	0,0115	0,0082	0,72	71,58	51,23
96630	0,0082	0,0052	0,63	63,23	39,97
96640	0,0061	0,0035	0,57	56,63	32,07
96650	0,0048	0,0025	0,51	51,42	26,44
96660	0,0039	0,0019	0,47	47,26	22,33
96670	0,0033	0,0014	0,44	43,85	19,23

**Table C.7 :** Deflection and ETR values at 1 $\mu$ m separation distance.

<b>Frequency (kHz)</b>	<b>Amplitude of First Beam (nm)</b>	<b>Amplitude of Second Beam (nm)</b>	<b>Transfer Rate of Deflection</b>	<b>Percent Transfer Rate of Deflection</b>	<b>Percent Transfer Rate of Energy</b>
96480	0,0043	0,0010	0,24	23,71	5,62
96490	0,0052	0,0013	0,25	24,57	6,04
96500	0,0062	0,0016	0,25	25,50	6,50
96510	0,0077	0,0020	0,26	26,49	7,02
96520	0,0098	0,0027	0,28	27,57	7,60
96530	0,0130	0,0037	0,29	28,75	8,26
96540	0,0179	0,0054	0,30	30,04	9,03
96550	0,0261	0,0082	0,31	31,50	9,92
96560	0,0405	0,0135	0,33	33,36	11,13
96570	0,0666	0,0249	0,37	37,30	13,91
96580	0,1265	0,0583	0,46	46,08	21,24
96590	0,0800	0,0336	0,42	41,99	17,63
96600	0,0424	0,0148	0,35	34,93	12,20
96610	0,0264	0,0085	0,32	32,41	10,50
96620	0,0179	0,0056	0,31	31,47	9,90
96630	0,0132	0,0040	0,30	30,37	9,22
96640	0,0101	0,0030	0,30	29,53	8,72
96650	0,0080	0,0023	0,29	28,80	8,29
96660	0,0065	0,0018	0,28	28,13	7,91
96670	0,0054	0,0015	0,28	27,50	7,56

**Table C.8** : Deflection and ETR values at 2 $\mu$ m separation distance.

<i>Frequency (kHz)</i>	<i>Amplitude of First Beam (nm)</i>	<i>Amplitude of Second Beam (nm)</i>	<i>Transfer Rate of Deflection</i>	<i>Percent Transfer Rate of Deflection</i>	<i>Percent Transfer Rate of Energy</i>
96480	0,0023	0,0009	0,39	39,14	15,32
96490	0,0027	0,0011	0,41	40,76	16,61
96500	0,0032	0,0013	0,42	42,42	18,00
96510	0,0038	0,0017	0,44	44,07	19,42
96520	0,0047	0,0021	0,46	45,54	20,74
96530	0,0060	0,0028	0,46	46,49	21,62
96540	0,0081	0,0038	0,46	46,34	21,47
96550	0,0116	0,0054	0,46	46,38	21,51
96560	0,0159	0,0105	0,66	65,99	43,55
96570	0,0235	0,0203	0,87	86,50	74,83
96580	0,0350	0,0299	0,85	85,39	72,92
96590	0,0383	0,0304	0,79	79,38	63,02
96600	0,0271	0,0197	0,73	72,83	53,04
96610	0,0165	0,0110	0,67	66,62	44,39
96620	0,0106	0,0065	0,61	61,02	37,24
96630	0,0074	0,0041	0,56	56,04	31,41
96640	0,0055	0,0028	0,52	51,64	26,67
96650	0,0043	0,0021	0,48	47,74	22,79
96660	0,0035	0,0015	0,44	44,28	19,61
96670	0,0029	0,0012	0,41	41,20	16,98



**APPENDIX D:**

*Deflection and ETR values for 8 $\mu$ m-long, 0.75 $\mu$ m-wide, and 0.34 $\mu$ m-thick beams at in-plane alignment under 1nN (nanonewton) dynamic force.*

**Table D.1 :** Deflection and ETR values at 0.1 $\mu$ m separation distance.

<b>Frequency (kHz)</b>	<b>Amplitude of First Beam (nm)</b>	<b>Amplitude of Second Beam (nm)</b>	<b>Transfer Rate of Deflection</b>	<b>Percent Transfer Rate of Deflection</b>	<b>Percent Transfer Rate of Energy</b>
45701	2,8081	5,0089	1,78	178,37	318,17
45702	2,5381	5,0443	1,99	198,74	394,99
45703	2,303	5,0918	2,21	221,09	488,83
45704	2,1176	5,1594	2,44	243,64	593,62
45705	2,0001	5,2548	2,63	262,73	690,25
45706	1,9702	5,3866	2,73	273,40	747,50
45707	2,0461	5,5647	2,72	271,97	739,66
45708	2,2406	5,8021	2,59	258,95	670,57
45709	2,5628	6,1168	2,39	238,68	569,66
45710	3,0263	6,5351	2,16	215,94	466,32
45711	3,6597	7,0978	1,94	193,94	376,15
45712	4,5203	7,872	1,74	174,15	303,27
45713	5,7201	8,9761	1,57	156,92	246,25
45714	7,4867	10,642	1,42	142,15	202,05
45715	10,338	13,389	1,30	129,51	167,73
45716	15,738	18,676	1,19	118,67	140,82
45717	29,961	32,761	1,09	109,35	119,56
45718	166,63	168,74	1,01	101,27	102,55
45719	49,188	46,348	0,94	94,23	88,79
45720	22,549	19,854	0,88	88,05	77,52

**Table D.2 :** Deflection and ETR values at 0.2 $\mu$ m separation distance.

<b>Frequency (kHz)</b>	<b>Amplitude of First Beam (nm)</b>	<b>Amplitude of Second Beam (nm)</b>	<b>Transfer Rate of Deflection</b>	<b>Percent Transfer Rate of Deflection</b>	<b>Percent Transfer Rate of Energy</b>
45701	5,0726	5,893	1,16	116,17	134,96
45702	4,6791	6,0864	1,30	130,08	169,20
45703	4,2456	6,2351	1,47	146,86	215,68
45704	3,8101	6,3611	1,67	166,95	278,74
45705	3,4113	6,4889	1,90	190,22	361,83
45706	3,091	6,6433	2,15	214,92	461,92
45707	2,8986	6,8493	2,36	236,30	558,36
45708	2,891	7,1348	2,47	246,79	609,07
45709	3,1228	7,5353	2,41	241,30	582,25
45710	3,6396	8,102	2,23	222,61	495,54
45711	4,4974	8,9182	1,98	198,30	393,22
45712	5,815	10,134	1,74	174,27	303,71
45713	7,873	12,052	1,53	153,08	234,34
45714	11,389	15,404	1,35	135,25	182,93
45715	18,671	22,495	1,20	120,48	145,16
45716	42,794	46,315	1,08	108,23	117,13
45717	199,99	196,02	0,98	98,01	96,07
45718	34,602	30,942	0,89	89,42	79,96
45719	19,357	15,897	0,82	82,13	67,45
45720	13,707	10,4	0,76	75,87	57,57

**Table D.3** : Deflection and ETR values at 0.3 $\mu$ m separation distance.

<i>Frequency (kHz)</i>	<i>Amplitude of First Beam (nm)</i>	<i>Amplitude of Second Beam (nm)</i>	<i>Transfer Rate of Deflection</i>	<i>Percent Transfer Rate of Deflection</i>	<i>Percent Transfer Rate of Energy</i>
45701	6,6467	5,7524	0,87	86,55	74,90
45702	6,4842	6,2719	0,97	96,73	93,56
45703	6,1527	6,7206	1,09	109,23	119,31
45704	5,6847	7,0892	1,25	124,71	155,52
45705	5,1419	7,3947	1,44	143,81	206,82
45706	4,6021	7,6749	1,67	166,77	278,12
45707	4,155	7,979	1,92	192,03	368,77
45708	3,9083	8,3641	2,14	214,01	458,00
45709	3,9904	8,8992	2,23	223,02	497,36
45710	4,534	9,6816	2,14	213,53	455,96
45711	5,6828	10,874	1,91	191,35	366,15
45712	7,7068	12,802	1,66	166,11	275,94
45713	11,341	16,248	1,43	143,27	205,26
45714	19,1	23,736	1,24	124,27	154,44
45715	46,248	50,362	1,09	108,90	118,58
45716	143,71	138,63	0,96	96,47	93,06
45717	33,051	28,538	0,86	86,35	74,56
45718	19,164	14,949	0,78	78,01	60,85
45719	13,788	9,7961	0,71	71,05	50,48
45720	10,914	7,1129	0,65	65,17	42,47

**Table D.4 :** Deflection and ETR values at 0.4 $\mu$ m separation distance.

<b>Frequency (kHz)</b>	<b>Amplitude of First Beam (nm)</b>	<b>Amplitude of Second Beam (nm)</b>	<b>Transfer Rate of Deflection</b>	<b>Percent Transfer Rate of Deflection</b>	<b>Percent Transfer Rate of Energy</b>
45701	7,2701	4,9667	0,68	68,32	46,67
45702	7,4486	5,6739	0,76	76,17	58,02
45703	7,4509	6,3966	0,86	85,85	73,70
45704	7,2374	7,0868	0,98	97,92	95,88
45705	6,8167	7,7097	1,13	113,10	127,92
45706	6,2586	8,2662	1,32	132,08	174,44
45707	5,6856	8,8006	1,55	154,79	239,59
45708	5,2657	9,3947	1,78	178,41	318,31
45709	5,2189	10,166	1,95	194,79	379,44
45710	5,8178	11,289	1,94	194,04	376,52
45711	7,4018	13,08	1,77	176,71	312,28
45712	10,627	16,255	1,53	152,96	233,97
45713	17,627	23,002	1,30	130,49	170,28
45714	40,285	45,051	1,12	111,83	125,06
45715	174,9	169,52	0,97	96,92	93,94
45716	35,986	30,612	0,85	85,07	72,36
45717	20,304	15,34	0,76	75,55	57,08
45718	14,493	9,8287	0,68	67,82	45,99
45719	11,438	7,0271	0,61	61,44	37,74
45720	9,5358	5,3502	0,56	56,11	31,48

**Table D.5** : Deflection and ETR values at 0.5 $\mu$ m separation distance.

<i>Frequency (kHz)</i>	<i>Amplitude of First Beam (nm)</i>	<i>Amplitude of Second Beam (nm)</i>	<i>Transfer Rate of Deflection</i>	<i>Percent Transfer Rate of Deflection</i>	<i>Percent Transfer Rate of Energy</i>
45701	7,4955	4,2797	0,57	57,10	32,60
45702	7,8895	5,0195	0,64	63,62	40,48
45703	8,169	5,8551	0,72	71,67	51,37
45704	8,2548	6,75	0,82	81,77	66,86
45705	8,0872	7,65	0,95	94,59	89,48
45706	7,6722	8,5115	1,11	110,94	123,08
45707	7,1157	9,3405	1,31	131,27	172,31
45708	6,6297	10,217	1,54	154,11	237,50
45709	6,5385	11,302	1,73	172,85	298,78
45710	7,2992	12,879	1,76	176,44	311,32
45711	9,5743	15,522	1,62	162,12	262,83
45712	14,865	20,762	1,40	139,67	195,08
45713	29,75	35,122	1,18	118,06	139,37
45714	141,78	142,12	1,00	100,24	100,48
45715	46,82	40,362	0,86	86,21	74,32
45716	23,393	17,589	0,75	75,19	56,53
45717	16,056	10,669	0,66	66,45	44,15
45718	12,442	7,392	0,59	59,41	35,30
45719	10,266	5,5078	0,54	53,65	28,78
45720	8,7983	4,2991	0,49	48,86	23,88

**Table D.6** : Deflection and ETR values at 1µm separation distance.

<b>Frequency (kHz)</b>	<b>Amplitude of First Beam (nm)</b>	<b>Amplitude of Second Beam (nm)</b>	<b>Transfer Rate of Deflection</b>	<b>Percent Transfer Rate of Deflection</b>	<b>Percent Transfer Rate of Energy</b>
45701	7,5962	2,2412	0,30	29,50	8,70
45702	8,3019	2,7247	0,33	32,82	10,77
45703	9,1034	3,3611	0,37	36,92	13,63
45704	9,9948	4,2074	0,42	42,10	17,72
45705	10,946	5,3368	0,49	48,76	23,77
45706	11,891	6,8364	0,57	57,49	33,05
45707	12,759	8,8045	0,69	69,01	47,62
45708	13,624	11,393	0,84	83,62	69,93
45709	15,152	15,036	0,99	99,23	98,47
45710	19,721	21,313	1,08	108,07	116,80
45711	36,485	37,387	1,02	102,47	105,01
45712	87,316	76,471	0,88	87,58	76,70
45713	38,261	27,683	0,72	72,35	52,35
45714	22,69	13,628	0,60	60,06	36,07
45715	16,545	8,3901	0,51	50,71	25,72
45716	13,22	5,7643	0,44	43,60	19,01
45717	11,098	4,2291	0,38	38,11	14,52
45718	9,6051	3,2437	0,34	33,77	11,40
45719	8,4868	2,5701	0,30	30,28	9,17
45720	7,6125	2,0878	0,27	27,43	7,52

**Table D.7 :** Deflection and ETR values at 2 $\mu$ m separation distance.

<b>Frequency (kHz)</b>	<b>Amplitude of First Beam (nm)</b>	<b>Amplitude of Second Beam (nm)</b>	<b>Transfer Rate of Deflection</b>	<b>Percent Transfer Rate of Deflection</b>	<b>Percent Transfer Rate of Energy</b>
45701	7,9368	1,079	0,14	13,59	1,85
45702	8,8113	1,3347	0,15	15,15	2,29
45703	9,8887	1,689	0,17	17,08	2,92
45704	11,244	2,1966	0,20	19,54	3,82
45705	12,993	2,9539	0,23	22,73	5,17
45706	15,325	4,1381	0,27	27,00	7,29
45707	18,6	6,0969	0,33	32,78	10,74
45708	23,644	9,5568	0,40	40,42	16,34
45709	32,593	15,986	0,49	49,05	24,06
45710	44,716	24,201	0,54	54,12	29,29
45711	37,388	18,951	0,51	50,69	25,69
45712	26,218	11,088	0,42	42,29	17,89
45713	19,996	6,8548	0,34	34,28	11,75
45714	16,184	4,5507	0,28	28,12	7,91
45715	13,572	3,1985	0,24	23,57	5,55
45716	11,66	2,3519	0,20	20,17	4,07
45717	10,202	1,793	0,18	17,57	3,09
45718	9,0549	1,4075	0,16	15,54	2,42
45719	8,1316	1,1319	0,14	13,92	1,94
45720	7,3737	0,92857	0,13	12,59	1,59

**APPENDIX E:**

*Deflection and ETR values for 20 $\mu$ m-long, 1 $\mu$ m-wide, and 0.34 $\mu$ m-thick beams at in-plane alignment under 0.1nN (nanonewton) dynamic force.*

**Table E.1 :** Deflection and ETR values at 0.1 $\mu$ m separation distance.

<b>Frequency (kHz)</b>	<b>Amplitude of First Beam (nm)</b>	<b>Amplitude of Second Beam (nm)</b>	<b>Transfer Rate of Deflection</b>	<b>Percent Transfer Rate of Deflection</b>	<b>Percent Transfer Rate of Energy</b>
7356	1,9989	0,51737	0,26	25,88	6,70
7357	2,3549	0,70155	0,30	29,79	8,88
7358	2,8812	1,0109	0,35	35,09	12,31
7359	3,755	1,6021	0,43	42,67	18,20
7360	5,5632	3,0272	0,54	54,41	29,61
7361	12,373	9,2904	0,75	75,09	56,38
7362	18,638	22,561	1,21	121,05	146,53
7363	2,5696	8,0135	3,12	311,86	972,55
7364	1,3762	7,4433	5,41	540,86	2925,28
7365	9,4597	13,713	1,45	144,96	210,14
7366	20,091	16,817	0,84	83,70	70,06
7367	6,4666	3,8054	0,59	58,85	34,63
7368	4,1038	1,8622	0,45	45,38	20,59
7369	3,0699	1,1337	0,37	36,93	13,64
7370	2,4745	0,77039	0,31	31,13	9,69
7371	2,0819	0,56029	0,27	26,91	7,24
7372	1,8014	0,42693	0,24	23,70	5,62
7373	1,5898	0,33663	0,21	21,17	4,48
7374	1,4241	0,27251	0,19	19,14	3,66
7375	1,2905	0,22526	0,17	17,46	3,05



**Table E.2 :** Deflection and ETR values at 0.5 $\mu$ m separation distance.

<i>Frequency (kHz)</i>	<i>Amplitude of First Beam (nm)</i>	<i>Amplitude of Second Beam (nm)</i>	<i>Transfer Rate of Deflection</i>	<i>Percent Transfer Rate of Deflection</i>	<i>Percent Transfer Rate of Energy</i>
7356	1,7604	0,1756	0,10	9,98	1,00
7357	2,0119	0,2288	0,11	11,37	1,29
7358	2,3486	0,3104	0,13	13,21	1,75
7359	2,824	0,4454	0,16	15,77	2,49
7360	3,5497	0,6942	0,20	19,56	3,82
7361	4,8089	1,237	0,26	25,72	6,62
7362	7,6385	2,8695	0,38	37,57	14,11
7363	23,615	16,435	0,70	69,60	48,44
7364	3,876	18,222	4,70	470,12	2210,16
7365	628,2	620,88	0,99	98,83	97,68
7366	9,7165	4,3469	0,45	44,74	20,01
7367	5,486	1,5864	0,29	28,92	8,36
7368	3,8924	0,8316	0,21	21,36	4,56
7369	3,0326	0,5138	0,17	16,94	2,87
7370	2,4892	0,3494	0,14	14,04	1,97
7371	2,1131	0,2532	0,12	11,98	1,44
7372	1,8368	0,192	0,10	10,45	1,09
7373	1,6248	0,1507	0,09	9,27	0,86
7374	1,457	0,1214	0,08	8,33	0,69
7375	1,3208	0,0999	0,08	7,56	0,57

**Table E.3** : Deflection and ETR values at 0.8 $\mu$ m separation distance.

<i>Frequency (kHz)</i>	<i>Amplitude of First Beam (nm)</i>	<i>Amplitude of Second Beam (nm)</i>	<i>Transfer Rate of Deflection</i>	<i>Percent Transfer Rate of Deflection</i>	<i>Percent Transfer Rate of Energy</i>
7356	1,7368	0,11178	0,06	6,44	0,41
7357	1,9793	0,14502	0,07	7,33	0,54
7358	2,301	0,19568	0,09	8,50	0,72
7359	2,749	0,2785	0,10	10,13	1,03
7360	3,4169	0,42803	0,13	12,53	1,57
7361	4,5252	0,74229	0,16	16,40	2,69
7362	6,7562	1,6047	0,24	23,75	5,64
7363	14,164	6,0916	0,43	43,01	18,50
7364	14,637	33,176	2,27	226,66	513,74
7365	35,631	24,696	0,69	69,31	48,04
7366	8,8515	2,6618	0,30	30,07	9,04
7367	5,3387	1,0252	0,19	19,20	3,69
7368	3,8535	0,54364	0,14	14,11	1,99
7369	3,022	0,33695	0,11	11,15	1,24
7370	2,4879	0,22935	0,09	9,22	0,85
7371	2,1152	0,1662	0,08	7,86	0,62
7372	1,84	0,12599	0,07	6,85	0,47
7373	1,6284	0,0988	0,06	6,07	0,37
7374	1,4605	0,07956	0,05	5,45	0,30
7375	1,3241	0,06544	0,05	4,94	0,24

**Table E.4 :** Deflection and ETR values at 1 $\mu$ m separation distance.

<i>Frequency (kHz)</i>	<i>Amplitude of First Beam (nm)</i>	<i>Amplitude of Second Beam (nm)</i>	<i>Transfer Rate of Deflection</i>	<i>Percent Transfer Rate of Deflection</i>	<i>Percent Transfer Rate of Energy</i>
7356	1,7312	0,08777	0,05	5,07	0,26
7357	1,9715	0,11376	0,06	5,77	0,33
7358	2,2896	0,1533	0,07	6,70	0,45
7359	2,731	0,21775	0,08	7,97	0,64
7360	3,3853	0,33354	0,10	9,85	0,97
7361	4,4589	0,57472	0,13	12,89	1,66
7362	6,5639	1,2228	0,19	18,63	3,47
7363	12,867	4,3198	0,34	33,57	11,27
7364	30,602	51,797	1,69	169,26	286,49
7365	27,337	15,213	0,56	55,65	30,97
7366	8,6063	2,0574	0,24	23,91	5,71
7367	5,2901	0,80541	0,15	15,22	2,32
7368	3,8385	0,42878	0,11	11,17	1,25
7369	3,0165	0,26612	0,09	8,82	0,78
7370	2,4859	0,18122	0,07	7,29	0,53
7371	2,1146	0,13135	0,06	6,21	0,39
7372	1,84	0,09958	0,05	5,41	0,29
7373	1,6287	0,07809	0,05	4,79	0,23
7374	1,461	0,06288	0,04	4,30	0,19
7375	1,3246	0,05172	0,04	3,90	0,15

**Table E.5** : Deflection and ETR values at 2 $\mu$ m separation distance.

<i>Frequency (kHz)</i>	<i>Amplitude of First Beam (nm)</i>	<i>Amplitude of Second Beam (nm)</i>	<i>Transfer Rate of Deflection</i>	<i>Percent Transfer Rate of Deflection</i>	<i>Percent Transfer Rate of Energy</i>
7356	1,7223	0,03628	0,021	2,107	0,044
7357	1,9593	0,04696	0,024	2,397	0,057
7358	2,272	0,06316	0,028	2,780	0,077
7359	2,7037	0,08945	0,033	3,308	0,109
7360	3,3383	0,13634	0,041	4,084	0,167
7361	4,3635	0,23278	0,053	5,335	0,285
7362	6,3032	0,48454	0,077	7,687	0,591
7363	11,407	1,568	0,137	13,746	1,890
7364	88,278	57,18	0,648	64,773	41,955
7365	20,719	4,9494	0,239	23,888	5,706
7366	8,3176	0,83914	0,101	10,089	1,018
7367	5,2367	0,33492	0,064	6,396	0,409
7368	3,8247	0,17909	0,047	4,682	0,219
7369	3,0131	0,11129	0,037	3,694	0,136
7370	2,4859	0,07581	0,030	3,050	0,093
7371	2,1157	0,05495	0,026	2,597	0,067
7372	1,8416	0,04165	0,023	2,262	0,051
7373	1,6303	0,03266	0,020	2,003	0,040
7374	1,4625	0,02629	0,018	1,798	0,032
7375	1,326	0,021622	0,016	1,631	0,027

**Table E.6 :** Deflection and ETR values at 4 $\mu$ m separation distance.

<b>Frequency (kHz)</b>	<b>Amplitude of First Beam (nm)</b>	<b>Amplitude of Second Beam (nm)</b>	<b>Transfer Rate of Deflection</b>	<b>Percent Transfer Rate of Deflection</b>	<b>Percent Transfer Rate of Energy</b>
7356	1,7209	0,0125	0,007	0,728	0,005
7357	1,9573	0,0162	0,008	0,828	0,007
7358	2,2692	0,02179	0,010	0,960	0,009
7359	2,6992	0,03084	0,011	1,142	0,013
7360	3,3306	0,04697	0,014	1,410	0,020
7361	4,3479	0,08008	0,018	1,842	0,034
7362	6,2607	0,16609	0,027	2,653	0,070
7363	11,186	0,53013	0,047	4,739	0,225
7364	54,181	11,996	0,221	22,141	4,902
7365	19,764	1,6383	0,083	8,289	0,687
7366	8,26	0,28849	0,035	3,493	0,122
7367	5,2246	0,11561	0,022	2,213	0,049
7368	3,8209	0,06188	0,016	1,620	0,026
7369	3,0118	0,03847	0,013	1,277	0,016
7370	2,4854	0,02621	0,011	1,055	0,011
7371	2,1156	0,019	0,009	0,898	0,008
7372	1,8416	0,0144	0,008	0,782	0,006
7373	1,6304	0,01129	0,007	0,693	0,005
7374	1,4626	0,00909	0,006	0,622	0,004
7375	1,3262	0,00748	0,006	0,564	0,003

*Deflection and ETR values for 20 $\mu$ m-long, 1 $\mu$ m-wide, and 0.34 $\mu$ m-thick beams at in-plane alignment under 0.01nN (nanonewton) dynamic force.*

**Table E.7 :** Deflection and ETR values at 8 $\mu$ m separation distance.

<b>Frequency (kHz)</b>	<b>Amplitude of First Beam (nm)</b>	<b>Amplitude of Second Beam (nm)</b>	<b>Transfer Rate of Deflection</b>	<b>Percent Transfer Rate of Deflection</b>	<b>Percent Transfer Rate of Energy</b>
7364,12	9,3943	1,1045	0,12	11,76	1,38
7364,14	10,833	1,4614	0,13	13,49	1,82
7364,16	12,795	2,0242	0,16	15,82	2,50
7364,18	15,627	2,9882	0,19	19,12	3,66
7364,2	20,071	4,8476	0,24	24,15	5,83
7364,22	27,949	9,149	0,33	32,73	10,72
7364,24	43,913	22,184	0,51	50,52	25,52
7364,26	50,548	53,219	1,05	105,28	110,85
7364,28	46,14	86,929	1,88	188,40	354,96
7364,3	86,951	60,614	0,70	69,71	48,60
7364,32	34,113	13,667	0,40	40,06	16,05
7364,34	22,344	6,2457	0,28	27,95	7,81
7364,36	16,806	3,6026	0,21	21,44	4,60
7364,38	13,519	2,349	0,17	17,38	3,02
7364,4	11,326	1,6542	0,15	14,61	2,13
7364,42	9,7529	1,2284	0,13	12,60	1,59
7364,44	8,567	0,9485	0,11	11,07	1,23
7364,46	7,6401	0,7546	0,10	9,88	0,98
7364,48	6,8952	0,6146	0,09	8,91	0,79
7364,5	6,2833	0,51032	0,08	8,12	0,66

**Table E.8** : Deflection and ETR values at 10 $\mu$ m separation distance.

<i>Frequency (kHz)</i>	<i>Amplitude of First Beam (nm)</i>	<i>Amplitude of Second Beam (nm)</i>	<i>Transfer Rate of Deflection</i>	<i>Percent Transfer Rate of Deflection</i>	<i>Percent Transfer Rate of Energy</i>
7364,12	9,1544	0,7256	0,08	7,93	0,63
7364,14	10,505	0,9567	0,09	9,11	0,83
7364,16	12,323	1,3184	0,11	10,70	1,14
7364,18	14,897	1,931	0,13	12,96	1,68
7364,2	18,817	3,0923	0,16	16,43	2,70
7364,22	25,453	5,7049	0,22	22,41	5,02
7364,24	38,473	13,479	0,35	35,03	12,27
7364,26	58,786	44,362	0,75	75,46	56,95
7364,28	129,53	151,81	1,17	117,20	137,36
7364,3	66,878	29,718	0,44	44,44	19,75
7364,32	33,061	8,6041	0,26	26,02	6,77
7364,34	22,369	4,0956	0,18	18,31	3,35
7364,36	16,966	2,3932	0,14	14,11	1,99
7364,38	13,68	1,5687	0,11	11,47	1,31
7364,4	11,466	1,1074	0,10	9,66	0,93
7364,42	9,8708	0,8234	0,08	8,34	0,70
7364,44	8,6662	0,6361	0,07	7,34	0,54
7364,46	7,724	0,5062	0,07	6,55	0,43
7364,48	6,9668	0,4124	0,06	5,92	0,35
7364,5	6,345	0,3424	0,05	5,40	0,29

**Table E.9 :** Deflection and ETR values at 12 $\mu$ m separation distance.

<b>Frequency (kHz)</b>	<b>Amplitude of First Beam (nm)</b>	<b>Amplitude of Second Beam (nm)</b>	<b>Transfer Rate of Deflection</b>	<b>Percent Transfer Rate of Deflection</b>	<b>Percent Transfer Rate of Energy</b>
7364,12	9,052	0,505	0,06	5,57	0,31
7364,14	10,368	0,663	0,06	6,39	0,41
7364,16	12,130	0,909	0,07	7,50	0,56
7364,18	14,607	1,323	0,09	9,06	0,82
7364,2	18,340	2,097	0,11	11,43	1,31
7364,22	24,568	3,803	0,15	15,48	2,40
7364,24	36,700	8,750	0,24	23,84	5,68
7364,26	63,294	31,291	0,49	49,44	24,44
7364,28	221,700	200,460	0,90	90,42	81,76
7364,3	62,702	20,915	0,33	33,36	11,13
7364,32	32,956	6,298	0,19	19,11	3,65
7364,34	22,502	2,996	0,13	13,31	1,77
7364,36	17,097	1,744	0,10	10,20	1,04
7364,38	13,787	1,140	0,08	8,27	0,68
7364,4	11,551	0,802	0,07	6,95	0,48
7364,42	9,939	0,595	0,06	5,99	0,36
7364,44	8,722	0,459	0,05	5,26	0,28
7364,46	7,770	0,365	0,05	4,69	0,22
7364,48	7,005	0,297	0,04	4,24	0,18
7364,5	6,378	0,246	0,04	3,86	0,15



**Table E.10** : Deflection and ETR values at 15 $\mu$ m separation distance.

<i>Frequency (kHz)</i>	<i>Amplitude of First Beam (nm)</i>	<i>Amplitude of Second Beam (nm)</i>	<i>Transfer Rate of Deflection</i>	<i>Percent Transfer Rate of Deflection</i>	<i>Percent Transfer Rate of Energy</i>
7364,12	9,271	0,344	0,037	3,71	0,14
7364,14	10,656	0,454	0,043	4,26	0,18
7364,16	12,523	0,625	0,050	4,99	0,25
7364,18	15,179	0,915	0,060	6,03	0,36
7364,2	19,248	1,464	0,076	7,61	0,58
7364,22	26,226	2,700	0,103	10,30	1,06
7364,24	40,665	6,440	0,158	15,84	2,51
7364,26	81,294	26,591	0,327	32,71	10,70
7364,28	190,550	114,830	0,603	60,26	36,32
7364,3	50,648	11,297	0,223	22,30	4,98
7364,32	29,793	3,803	0,128	12,76	1,63
7364,34	21,068	1,872	0,089	8,89	0,79
7364,36	16,282	1,108	0,068	6,81	0,46
7364,38	13,261	0,731	0,055	5,51	0,30
7364,4	11,184	0,518	0,046	4,63	0,21
7364,42	9,668	0,386	0,040	3,99	0,16
7364,44	8,514	0,299	0,035	3,51	0,12
7364,46	7,605	0,238	0,031	3,13	0,10
7364,48	6,872	0,194	0,028	2,82	0,08
7364,5	6,267	0,161	0,026	2,57	0,07

**Table E.11** : Deflection and ETR values at 18 $\mu$ m separation distance.

<i>Frequency (kHz)</i>	<i>Amplitude of First Beam (nm)</i>	<i>Amplitude of Second Beam (nm)</i>	<i>Transfer Rate of Deflection</i>	<i>Percent Transfer Rate of Deflection</i>	<i>Percent Transfer Rate of Energy</i>
7364,12	9,238	0,244	0,026	2,64	0,07
7364,14	10,612	0,323	0,030	3,04	0,09
7364,16	12,465	0,446	0,036	3,58	0,13
7364,18	15,095	0,656	0,043	4,34	0,19
7364,2	19,121	1,057	0,055	5,53	0,31
7364,22	26,023	1,972	0,076	7,58	0,57
7364,24	40,381	4,834	0,120	11,97	1,43
7364,26	84,172	22,315	0,265	26,51	7,03
7364,28	146,560	53,420	0,364	36,45	13,29
7364,3	51,028	7,239	0,142	14,19	2,01
7364,32	30,106	2,538	0,084	8,43	0,71
7364,34	21,245	1,268	0,060	5,97	0,36
7364,36	16,391	0,757	0,046	4,62	0,21
7364,38	13,335	0,502	0,038	3,76	0,14
7364,4	11,237	0,357	0,032	3,17	0,10
7364,42	9,708	0,266	0,027	2,74	0,08
7364,44	8,545	0,207	0,024	2,42	0,06
7364,46	7,630	0,165	0,022	2,16	0,05
7364,48	6,892	0,134	0,020	1,95	0,04
7364,5	6,284	0,112	0,018	1,78	0,03

**Table E.12** : Deflection and ETR values at 20 $\mu$ m separation distance.

<i>Frequency (kHz)</i>	<i>Amplitude of First Beam (nm)</i>	<i>Amplitude of Second Beam (nm)</i>	<i>Transfer Rate of Deflection</i>	<i>Percent Transfer Rate of Deflection</i>	<i>Percent Transfer Rate of Energy</i>
7364,12	9,113	0,197	0,022	2,16	0,05
7364,14	10,448	0,259	0,025	2,48	0,06
7364,16	12,239	0,355	0,029	2,90	0,08
7364,18	14,769	0,518	0,035	3,51	0,12
7364,2	18,606	0,825	0,044	4,43	0,20
7364,22	25,101	1,509	0,060	6,01	0,36
7364,24	38,340	3,557	0,093	9,28	0,86
7364,26	77,850	15,050	0,193	19,33	3,74
7364,28	160,660	55,001	0,342	34,23	11,72
7364,3	54,959	7,007	0,127	12,75	1,63
7364,32	31,526	2,313	0,073	7,34	0,54
7364,34	21,953	1,125	0,051	5,12	0,26
7364,36	16,810	0,661	0,039	3,93	0,15
7364,38	13,612	0,434	0,032	3,19	0,10
7364,4	11,433	0,306	0,027	2,68	0,07
7364,42	9,854	0,228	0,023	2,31	0,05
7364,44	8,657	0,176	0,020	2,03	0,04
7364,46	7,720	0,140	0,018	1,81	0,03
7364,48	6,965	0,114	0,016	1,63	0,03
7364,5	6,345	0,095	0,015	1,49	0,02

**APPENDIX F:**

*Deflection and ETR values under viscous damping for 20 $\mu$ m-long, 1 $\mu$ m-wide, and 0.34 $\mu$ m-thick beams at in-plane alignment under 1nN (nanonewton) dynamic force.*

**Table F.1 :** Deflection and ETR values at 0.1 $\mu$ m separation distance.

<b>Frequency (kHz)</b>	<b>Amplitude of First Beam (nm)</b>	<b>Amplitude of Second Beam (nm)</b>	<b>Transfer Rate of Deflection</b>	<b>Percent Transfer Rate of Deflection</b>	<b>Percent Transfer Rate of Energy</b>
7356	18,407	4,491	0,24	24,40	5,95
7357	20,966	5,784	0,28	27,59	7,61
7358	24,188	7,652	0,32	31,63	10,01
7359	28,157	10,378	0,37	36,86	13,58
7360	32,561	14,220	0,44	43,67	19,07
7361	36,009	18,879	0,52	52,43	27,49
7362	36,461	22,853	0,63	62,68	39,29
7363	34,774	24,808	0,71	71,34	50,89
7364	34,506	25,067	0,73	72,65	52,77
7365	36,290	23,746	0,65	65,43	42,82
7366	36,760	20,278	0,55	55,16	30,43
7367	33,900	15,561	0,46	45,90	21,07
7368	29,469	11,373	0,39	38,59	14,89
7369	25,260	8,333	0,33	32,99	10,88
7370	21,802	6,249	0,29	28,66	8,21
7371	19,059	4,816	0,25	25,27	6,38
7372	16,879	3,807	0,23	22,55	5,09
7373	15,125	3,077	0,20	20,34	4,14
7374	13,690	2,535	0,19	18,52	3,43
7375	12,498	2,122	0,17	16,98	2,88

**Table F.2** : Deflection and ETR values at 0.2 $\mu$ m separation distance.

<i>Frequency (kHz)</i>	<i>Amplitude of First Beam (nm)</i>	<i>Amplitude of Second Beam (nm)</i>	<i>Transfer Rate of Deflection</i>	<i>Percent Transfer Rate of Deflection</i>	<i>Percent Transfer Rate of Energy</i>
7356	18,02	3,2794	0,18	18,20	3,31
7357	20,604	4,2574	0,21	20,66	4,27
7358	24,013	5,7299	0,24	23,86	5,69
7359	28,655	8,066	0,28	28,15	7,92
7360	35,09	11,97	0,34	34,11	11,64
7361	43,503	18,584	0,43	42,72	18,25
7362	50,726	28,016	0,55	55,23	30,50
7363	49,556	35,146	0,71	70,92	50,30
7364	46,714	36,836	0,79	78,85	62,18
7365	50,727	34,699	0,68	68,40	46,79
7366	50,469	26,695	0,53	52,89	27,98
7367	42,311	17,393	0,41	41,11	16,90
7368	34,01	11,233	0,33	33,03	10,91
7369	27,84	7,6279	0,27	27,40	7,51
7370	23,405	5,4596	0,23	23,33	5,44
7371	20,139	4,0823	0,20	20,27	4,11
7372	17,655	3,161	0,18	17,90	3,21
7373	15,71	2,517	0,16	16,02	2,57
7374	14,148	2,0503	0,14	14,49	2,10
7375	12,867	1,7017	0,13	13,23	1,75

**Table F.3 :** Deflection and ETR values at 0.3 $\mu$ m separation distance.

<i>Frequency (kHz)</i>	<i>Amplitude of First Beam (nm)</i>	<i>Amplitude of Second Beam (nm)</i>	<i>Transfer Rate of Deflection</i>	<i>Percent Transfer Rate of Deflection</i>	<i>Percent Transfer Rate of Energy</i>
7356	17,751	2,5606	0,14	14,43	2,08
7357	20,277	3,325	0,16	16,40	2,69
7358	23,633	4,4848	0,19	18,98	3,60
7359	28,285	6,3579	0,22	22,48	5,05
7360	35,071	9,6326	0,27	27,47	7,54
7361	45,385	15,889	0,35	35,01	12,26
7362	59,572	28,079	0,47	47,13	22,22
7363	65,59	43,448	0,66	66,24	43,88
7364	59,055	48,361	0,82	81,89	67,06
7365	65,76	44,996	0,68	68,42	46,82
7366	61,606	30,021	0,49	48,73	23,75
7367	46,932	16,896	0,36	36,00	12,96
7368	36,019	10,128	0,28	28,12	7,91
7369	28,892	6,6278	0,23	22,94	5,26
7370	24,047	4,6466	0,19	19,32	3,73
7371	20,574	3,4298	0,17	16,67	2,78
7372	17,972	2,6326	0,15	14,65	2,15
7373	15,953	2,0831	0,13	13,06	1,71
7374	14,341	1,6889	0,12	11,78	1,39
7375	13,024	1,3966	0,11	10,72	1,15

**Table F.4** : Deflection and ETR values at 0.4 $\mu$ m separation distance.

<i>Frequency (kHz)</i>	<i>Amplitude of First Beam (nm)</i>	<i>Amplitude of Second Beam (nm)</i>	<i>Transfer Rate of Deflection</i>	<i>Percent Transfer Rate of Deflection</i>	<i>Percent Transfer Rate of Energy</i>
7356	18,407	4,491	0,24	24,40	5,95
7357	20,966	5,784	0,28	27,59	7,61
7358	24,188	7,652	0,32	31,63	10,01
7359	28,157	10,378	0,37	36,86	13,58
7360	32,561	14,220	0,44	43,67	19,07
7361	36,009	18,879	0,52	52,43	27,49
7362	36,461	22,853	0,63	62,68	39,29
7363	34,774	24,808	0,71	71,34	50,89
7364	34,506	25,067	0,73	72,65	52,77
7365	36,290	23,746	0,65	65,43	42,82
7366	36,760	20,278	0,55	55,16	30,43
7367	33,900	15,561	0,46	45,90	21,07
7368	29,469	11,373	0,39	38,59	14,89
7369	25,260	8,333	0,33	32,99	10,88
7370	21,802	6,249	0,29	28,66	8,21
7371	19,059	4,816	0,25	25,27	6,38
7372	16,879	3,807	0,23	22,55	5,09
7373	15,125	3,077	0,20	20,34	4,14
7374	13,690	2,535	0,19	18,52	3,43
7375	12,498	2,122	0,17	16,98	2,88

**Table F.5** : Deflection and ETR values at 0.5 $\mu$ m separation distance.

<i>Frequency (kHz)</i>	<i>Amplitude of First Beam (nm)</i>	<i>Amplitude of Second Beam (nm)</i>	<i>Transfer Rate of Deflection</i>	<i>Percent Transfer Rate of Deflection</i>	<i>Percent Transfer Rate of Energy</i>
7356	17,467	1,730	0,10	9,91	0,98
7357	19,912	2,244	0,11	11,27	1,27
7358	23,154	3,022	0,13	13,05	1,70
7359	27,654	4,286	0,16	15,50	2,40
7360	34,307	6,533	0,19	19,04	3,63
7361	45,037	11,072	0,25	24,58	6,04
7362	64,222	21,995	0,34	34,25	11,73
7363	93,049	49,657	0,53	53,37	28,48
7364	86,405	70,551	0,82	81,65	66,67
7365	97,728	61,965	0,63	63,41	40,20
7366	74,419	29,257	0,39	39,31	15,46
7367	50,448	13,759	0,27	27,27	7,44
7368	37,400	7,731	0,21	20,67	4,27
7369	29,625	4,914	0,17	16,59	2,75
7370	24,512	3,390	0,14	13,83	1,91
7371	20,902	2,478	0,12	11,85	1,40
7372	18,218	1,889	0,10	10,37	1,07
7373	16,146	1,487	0,09	9,21	0,85
7374	14,496	1,201	0,08	8,29	0,69
7375	13,153	0,990	0,08	7,53	0,57



**Table F.6 :** Deflection and ETR values at 1 $\mu$ m separation distance.

<b>Frequency (kHz)</b>	<b>Amplitude of First Beam (nm)</b>	<b>Amplitude of Second Beam (nm)</b>	<b>Transfer Rate of Deflection</b>	<b>Percent Transfer Rate of Deflection</b>	<b>Percent Transfer Rate of Energy</b>
7356	17,271	0,874	0,051	5,06	0,26
7357	19,654	1,131	0,058	5,75	0,33
7358	22,801	1,521	0,067	6,67	0,44
7359	27,149	2,153	0,079	7,93	0,63
7360	33,544	3,278	0,098	9,77	0,95
7361	43,874	5,576	0,127	12,71	1,62
7362	63,294	11,452	0,181	18,09	3,27
7363	110,700	33,990	0,307	30,70	9,43
7364	170,680	118,180	0,692	69,24	47,94
7365	160,470	72,014	0,449	44,88	20,14
7366	80,959	18,461	0,228	22,80	5,20
7367	51,764	7,728	0,149	14,93	2,23
7368	37,961	4,196	0,111	11,05	1,22
7369	29,962	2,626	0,088	8,76	0,77
7370	24,746	1,796	0,073	7,26	0,53
7371	21,077	1,305	0,062	6,19	0,38
7372	18,355	0,991	0,054	5,40	0,29
7373	16,256	0,778	0,048	4,79	0,23
7374	14,587	0,627	0,043	4,30	0,18
7375	13,229	0,516	0,039	3,90	0,15

**Table F.7** : Deflection and ETR values at 2 $\mu$ m separation distance.

<i>Frequency (kHz)</i>	<i>Amplitude of First Beam (nm)</i>	<i>Amplitude of Second Beam (nm)</i>	<i>Transfer Rate of Deflection</i>	<i>Percent Transfer Rate of Deflection</i>	<i>Percent Transfer Rate of Energy</i>
7356	17,216	0,362	0,02	2,10	0,04
7357	19,581	0,469	0,02	2,39	0,06
7358	22,701	0,630	0,03	2,77	0,08
7359	27,003	0,891	0,03	3,30	0,11
7360	33,316	1,356	0,04	4,07	0,17
7361	43,477	2,308	0,05	5,31	0,28
7362	62,526	4,761	0,08	7,61	0,58
7363	110,840	14,817	0,13	13,37	1,79
7364	337,380	146,660	0,43	43,47	18,90
7365	187,670	41,573	0,22	22,15	4,91
7366	81,848	8,139	0,10	9,94	0,99
7367	52,022	3,307	0,06	6,36	0,40
7368	38,107	1,778	0,05	4,67	0,22
7369	30,060	1,108	0,04	3,68	0,14
7370	24,817	0,756	0,03	3,04	0,09
7371	21,131	0,548	0,03	2,59	0,07
7372	18,398	0,416	0,02	2,26	0,05
7373	16,290	0,326	0,02	2,00	0,04
7374	14,615	0,263	0,02	1,80	0,03
7375	13,253	0,216	0,02	1,63	0,03

## CURRICULUM VITAE



**Name Surname:** Ünal DEĞİRMENÇİ

**Place and Date of Birth:** Malatya/ Turkey and 05/09/1988

**Address:** Inonu Mah. Istasyon Cad. 7. Sok. Sabir Apt. B 8/16 Malatya // Turkey

**E-Mail:** [unaldegirmenci44@gmail.com](mailto:unaldegirmenci44@gmail.com), [udegirmenci@itu.edu.tr](mailto:udegirmenci@itu.edu.tr)

**B.Sc.:** Industrial Engineering, Selçuk University, Konya, 2006-2010.

Mechanical Engineering, Selçuk University, Konya, 2008-2010.

### Professional Experience and Rewards:

March 2012– Continued                      Research Asst.                      Istanbul Technical University

August 2010–March 2012                      Research Asst.                      Bingol University

### List of Publications and Patents:

- **Degirmenci U.**, Guzel E. and Bulgan E., “Energy transfer through coupled micro/nano-scale structures,” *2013 9th National Conference on Nanoscience and Nanotechnology NanoTR-9*.
- Akgobek O., Kaya S., **Degirmenci U.**, Engin O., “Parallel Greedy Metaheuristic Algorithm for Solving Open Shop Scheduling Problem”, *e -Journal of New World Sciences Academy Engineering Sciences*, ISSN: 1308 -7231, 6 (1),p:421-427, 2011.